

Alma Mater Studiorum – Università di Bologna

**DOTTORATO DI RICERCA IN
GEOFISICA**

Ciclo 33

Settore Concorsuale: 04/A4

Settore Scientifico Disciplinare: GEO/10

**DISCRIMINATION BETWEEN NATURAL AND INDUCED SEISMICITY
IN THE HENGILL GEOTHERMAL AREA, SW ICELAND**

Presentata da: Camilla Rossi

Coordinatore Dottorato

Nadia Pinaridi

Supervisore

Prof. Paolo Gasperini

Co-Supervisore

Dr. Francesco Grigoli

Esame finale anno 2021

CONTENTS

Acknowledgments.....1

ABSTRACT.....2

List of Figures.....3

List of Tables.....5

1. INTRODUCTION6

 1.1 *NATURAL AND INDUCED SEISMICITY*6

 1.2 *THESIS OUTLINE*.....9

2. CASE STUDY: HENGILL GEOTHERMAL AREA10

 2.1 *TECTONIC SETTING AND GEOPHYSICAL CONSTRAINS*10

 2.2 *GEOTHERMAL FIELD AT HENGILL VOLCANO COMPLEX*12

 2.3 *SEISMICITY*.....13

3. DATASET AND SEISMIC NETWORK15

4. SEISMIC EVENT LOCATION.....19

 4.1 *METHOD*.....19

 4.2 *APPLICATION TO THE HENGILL DATASET*24

 4.3 *RESULTS*.....26

5. CLUSTERING ANALYSIS.....30

 5.1 *METHOD*.....30

 5.2 *SPATIAL AND WAVEFORM CLUSTERING AT HENGILL AREA*32

 5.3 *RESULTS*.....33

6. MASTER EVENTS IDENTIFICATION AND RELATIVE MAGNITUDE ESTIMATION.....37

7. EARTHQUAKE SOURCE INVERSION39

 7.1 *METHOD*.....39

 7.2 *APPLICATION TO THE HENGILL DATASET*42

 7.3 *RESULTS*.....45

8. DISCUSSION49

9. DISCRIMINATING BETWEEN NATURAL AND INDUCED SEISMICITY AT HENGILL AREA53

 9.1 *SUMMARY*.....60

10. CONCLUSIONS62

REFERENCES65

Appendix A. Catalogue	78
Appendix B. Relative magnitude	92
Appendix C. Data fitting and optimization of moment tensor inversion.....	101
Appendix D. Test Davis and Frohlich (1993).....	104

Acknowledgments

I would like to express my sincere gratitude to Dr. Francesco Grigoli for his guidance, support and encouragements throughout my Ph.D. The starting point of my work was possible thanks to him.

I would like to thank Prof. Paolo Gasperini for his advice and support during the development of this project.

I would also like to thank Dr. Simone Cesca for his guidance, suggestions and instructions which greatly improved the quality of this project.

Thanks to Dr. Sebastian Heimann for his technical support and patience.

I am also grateful to Luca Scarabello for his assistance and practical suggestions.

Special thanks are given to Matteo, who followed me during this path and help me in different ways, from technical to moral supports.

Thanks to my colleagues and friends who I met and who supported me during these last three years.

My deep gratitude goes to my Family: thanks for understanding the choice I made and for supporting me during this important chapter of my life.

ABSTRACT

The Hengill area is a complex tectonic and geothermal site, located at the triple junction between the Reykjanes Peninsula (RP), the Western Volcanic Zone (WVZ), and the South Iceland Seismic Zone (SISZ). Geothermal systems in the vicinity of the Hengill volcano are exploited for electrical power and heat production, and today the two largest operating geothermal power plants are located at the Nesjavellir and the Hellisheiði. The region is seismically highly active with several thousand earthquakes located yearly, and whose origin may be either natural or anthropogenic. The thesis focuses on the analysis and investigation of the M_L 4.7 mainshock and the seismicity starting few days before the mainshock and in the following 30 days of the sequence, to understand the source mechanisms and to discriminate the origin of these seismic events. I use a very dense seismic monitoring network deployed since November 2018 and apply robust and full-waveform based methods for earthquake location, clustering analysis and source mechanism determination. To discriminate between natural and induced earthquakes, I also consider the spatial and temporal correlation between injections and seismic events. Results show that seismicity is clustered, highlighting how shallower events are located in the center of the geothermal area, near the geothermal plants, while deeper ones occurred at the edge of the geothermal site and in the southern part of the study area. Moreover, shallower seismicity near Hellisheiði boreholes show a relationship with injection activities and presents a large non-double-couple and isotropic components of moment tensor solutions, suggesting the influence of geothermal activity and geothermal energy exploitation on their origin. Deeper seismicity, far from injection sites and close to deviatoric solutions of the moment tensor, might have a more a natural origin due to tectonic and geothermal activity.

List of Figures

Figure 2.1 - Map of Iceland with the main tectonic zone.....	10
Figure 2.2 - Map of Hengill geothermal area with the main tectonic zone.....	11
Figure 3.1 - Map of study area with the three sub-seismic networks used.	16
Figure 3.2 - Magnitude plot.	16
Figure 3.3 - Recorded seismograms and power spectra	17
Figure 3.4 - Local and regional seismic networks.....	18
Figure 4.1 - LOKI location process.....	21
Figure 4.2 - Examples of unfiltered and filtered waveforms and amplitude spectra.....	24
Figure 4.3 - Three different 1-D velocity models for P and S waves.....	25
Figure 4.4 - Coherence values of three velocity models.....	26
Figure 4.5 - Example of coherence matrix	27
Figure 4.6 - Histogram plots of results	27
Figure 4.7 - Map and two orthogonal NS and EW vertical sections of 636 earthquakes.....	28
Figure 4.8 - Cumulative plot.....	29
Figure 5.1 - DBSCAN method	31
Figure 5.2 - Map and two orthogonal NS and EW vertical sections of computed spatial clustering.	34
Figure 5.3 - Example of waveform clustering results for P and S waves of cluster 1	35
Figure 5.4 - Example of waveform clustering results for P and S waves of cluster 3	36
Figure 6.1 - Map of computed relative magnitude of eight clusters and time-magnitude plot.....	38
Figure 7.1 - GROND optimization process.....	42
Figure 7.2 - Full waveform and body waves windows for master events inversion.	43
Figure 7.3 - Full waveform windows for the mainshock inversion.....	44
Figure 7.4 - Results of earthquake source inversion.....	45
Figure 7.5 - DC focal mechanism solution and triangular diagram for faults classification.....	46
Figure 7.6 - Orientation of pressure (P), tension (T) and null (B) axes	47
Figure 7.7 - Misfit values of earthquake source inversion.....	48
Figure 8.1 - Waveform clustering results and DC focal mechanism of cluster 3.....	50
Figure 8.2 - Decomposition of full moment tensor solutions	51
Figure 8.3 - Percentage of moment tensor components.....	52

Figure 9.1 - Map and two orthogonal NS and EW vertical sections of clusters with the full moment tensor solutions.....	56
Figure 9.2 - Map and two orthogonal NS and EW vertical sections view of injection wells at Húsmúli and Gráuhnúkar site	57
Figure 9.3 - Pressure (bar) (a) and flow rate Q (l/s) (b) at Gráuhnúkar wells.....	58
Figure 9.4 - Pressure (bar) (a) and flow rate Q (l/s) (b) at Húsmúli wells.....	59
Figure C.1 - Observed and synthetic full waveform and body waves best fitting model of master events	102
Figure C.2 - Observed and synthetic full waveform best fitting model of the mainshock.....	103
Figure C.3 - Sequence plots for strike and rake parameters	104
Figure C.4 - Sorted misfit of single bootstrap chains	104

List of Tables

Table 5.1 - Results of spatial and waveform clustering	34
Table 6.1 - List of selected master events plus the mainshock	37
Table 7.1 - Mean BIC and AIC values.	48
Table 9.1 - Pressure (bar) at well head (bar) at Húsmúli and Gráuhnúkar site	54
Table 9.2 - Flow rate (l/s) at well head at Húsmúli and Gráuhnúkar site	54
Table 9.3 - Mean epicentral distances (km) between clusters and the wells bottom	55
Table A.1 - Catalogue	79
Table B.1 - Relative magnitude of Cluster 1	93
Table B.2 - Relative magnitude of Cluster 2	95
Table B.3 - Relative magnitude of Cluster 3	97
Table B.4 - Relative magnitude of Cluster 4	99
Table B.5 - Relative magnitude of Cluster 5	99
Table B.6 - Relative magnitude of Cluster 6	100
Table B.7 - Relative magnitude of Cluster 7	101
Table B.8 - Relative magnitude of Cluster 8	101
Table D.1 - Results of Davis and Frohlich (1993) test for each spatial cluster	101

1. INTRODUCTION

1.1 NATURAL AND INDUCED SEISMICITY

In recent years, the discrimination between natural and induced seismicity has attracted considerable interest in the scientific community (Ellsworth et al 2013).

Natural seismicity is mostly caused by tectonic process occurring as shear faulting. However, deviations from pure shear faulting have been observed in volcanic and geothermal environments (Miller et al., 1998; Klein et al., 1977; Arnott and Foulger, 1994a, b; Vavryìcuk 2002; Martens & White, 2013, Fischer et al., 2014; Sgattoni et., 2016), where the circulation of high-pressure and temperature fluids and magma intrusion occur and can facilitate combinations of shear and tensile faulting as well as the opening of tensile cracks. Examples of seismicity in volcanic and geothermal areas are the microseismicity at Long Valley Caldera, California (Foulger et al., 2004) caused by hydraulic fracturing, seismic activity of Krafla volcano, Iceland (Eirnasson 1991) and swarm seismicity associated with deep fluid reservoirs, Czech Republic (Cox 2016).

Seismicity can be even induced by industrial activities, such as hydrocarbon extraction and natural gas storage operations, shale gas exploitation, geothermal energy exploitation, mining operations, and water impoundment (see Grigoli et al., 2017, for a review). Such activities may alter the stress field of the shallow Earth's crust inducing seismicity. Although, the term "induced seismicity" generally refers to man-made earthquakes, several studies (McGarr and Simpson 1997; Shapiro et al. 2013; Dahm et al., 2012: 2015), distinguished between "triggered" and "induced" earthquakes. In the first case, the occurrence of a seismic event is 'anticipated' because of a stress perturbation on favourable oriented faults that are prone to natural failure in the future. In the second case, the seismicity is fully controlled in nucleation and size by stress change produced by human operations.

Several cases from low to moderate seismicity related to industrial operation have been reported in recent years. Among the key examples I may cite St. Gallen, Switzerland (Deichmann and Giardini, 2009; Kraft and Deichmann, 2014; Edwards et al., 2015) and the Geyser geothermal field, California (Eberhart-Phillips and Oppenheimer, 1984; Ross

et al., 1996, 1999; Martinez-Garzòn et al. 2017), where the stimulation of unconventional hydrocarbon reservoirs, geothermal systems, and wastewater injection can trigger or induce seismic events as a consequence of tensile fractures opening. Other cases of induced events are reported in Europe, for instance, in Basel, Switzerland (Häring et al. 2008), at the Groningen gas field, Netherlands (Bourne et al., 2014), and at the Castor Project gas storage, Spain (Cesca et al., 2014). Cases of induced events with larger magnitude ($M > 5$) have been also reported, for instance the 2011 Mw 5.6, 2016 Mw 5.1 and Mw 5.8 events occurred in Oklahoma, United States, associated with wastewater injection operations (Ellsworth 2013, Langenbruch and Zoback, 2016) and the Mw 5.5 Pohang induced earthquake, South Korea, due to enhanced geothermal stimulation (Grigoli et al., 2018; Ellsworth et al., 2019).

With the growing number of industrial-related seismicity, the monitoring and analysis of such events have become increasingly important. A dense seismic monitoring infrastructure allows to detect even low magnitude events with low signal-to-noise ratio, and plays a fundamental role to test the efficiency of the industrial activity and to assess the seismic hazard. The lack of an adequate monitoring network, on the contrary, does not allow to quickly detect seismicity, to accurately analyse it and, finally, to properly estimate the hazard related to industrial operations. Few important examples are Blackpool (UK, Clarke et al., 2014), Castor (Spain, Cesca et al., 2015; Gaité et al., 2016), Basel (Switzerland, Häring et al. 2008) and Pohang (South Korea, Grigoli et al. 2018, Ellsworth et al. 2019) cases where industrial activities were definitively interrupted after the occurrence of felt seismic events.

These cases highlight the potential socio-economic impact of induced seismicity and the risk associated with, demonstrating the importance to investigate, and monitoring such seismic events.

In particular, this concept becomes relevant for industrial applications in seismically active areas, where both natural and induced seismicity may occur and where their discrimination and the assessment of origin processes are needed.

For instance, in some geothermal project sites, seismic events due to the geothermal power production occur together with natural seismicity, arising from tectonic, magmatic and geothermal sources. Examples are the Geysers geothermal field (California, Eberhart-Phillips and Oppenheimer, 1984; Ross et al., 1996, 1999; Guilhem et al., 2014; Martinez-Garzòn et al. 2017), the Coso geothermal field (California, Manley and Bacon, 2000;

Hauksson and Unruh, 2007; Kaven et al., 2014; Schoenball et al., 2015), the Salton Sea geothermal field (California, Brodsky and Lajoie, 2013; Cheng and Chen, 2018) and at Soultz-sous-Forêts (France, Cornet et al 1997; Dorbath et al. 2009, Cuenot et al. 2008, 2015). Other examples are at Lacq gas field area (Southwestern France, Maury et al., 1990; Grasso and Wittlinger 1990; Segall 1994, Bardainne et al., 2008), where seismicity is linked to the gas production and to Pyrenean tectonic stress, and in some mining activity sites (Bischoff et al., 2010; Cesca et al., 2013; Wilson et a., 2015; Koper et al., 2016).

The problem of the discrimination between natural and induced seismicity is complex, still unsolved and an active topic of research. Among the different approaches to tackle this problem the spatio-temporal correlation between human activity and earthquakes occurrence proximal to industrial sites is probably the most direct one (Goebel et al., 2015). A qualitative approach allowing to discriminate between natural and induced seismicity and that uses the spatio-temporal correlation between seismicity and industrial activities is based on a set of YES-NO criteria (Davis and Frohlich, 1993; Davis et al., 1995); if more than half of the questions are answered by YES, the event is considered to be likely induced. An improved version of this last approach is proposed by Verdon et al., (2019), in which the final outcome is composed by two scores: the first one reflects whether events are induced or natural, the second one represents the strength of available evidence.

Dahm et al (2012), suggested three different discrimination approaches: physics-based probabilistic method, statistics-based method, and source parameters-based method. The first approach quantifies the probability that a given earthquake is triggered by a given stress-inducing phenomenon (Passarelli et al., 2013; Dieterich et al., 2015). Statistics methods are based on the detection of changes in statistical parameters of the observed seismicity (Hainzl et al., 2005; Schoenball et al., 2015; Zaliapin et al., 2016), which may be correlated with industrial activities. The third method assess the origin of earthquake based on the difference in earthquake source parameters; for instance, a high isotropic component of moment tensor may indicate an induced origin (Syleny et al., 2009; Cesca et al., 2013; Koper et la., 2016; Vavryčuk 2015). In addition, recent hybrid discrimination methods, joining physical and statistical approaches and accounting for detailed seismic source parameter have been proposed (Dahm et al., 2015). However, it is important to mention that a standardized scheme or recipe to discriminate induced earthquakes from natural one still not exists, and that the choice to follow one approach

with respect to other ones often depends on the availability of data (e.g. hydraulic, geological and geomechanical data).

1.2 THESIS OUTLINE

In this thesis, I focus on the analysis of seismicity in the Hengill geothermal area, located in SW of Iceland. The region is characterized by a complex geological and tectonic setting and it is affected by an intense seismic activity, with several thousand earthquakes located yearly. Furthermore, Hengill is a high-temperature geothermal area hosting two of the largest geothermal power plants of the country.

Due to the presence of industrial operations that may induce or trigger earthquakes in a seismically active area, the problem of discriminating among natural and induced events in the Hengill region is important.

I investigate the M_L 4.7 mainshock occurred on 30 December 2018 and the seismicity recorded at Hengill area from 22 December 2018 to 31 January 2019.

The dataset consists of 636 seismic events, 98% of them with magnitude below 2 and characterized by a strong noise contamination.

I use a very dense broadband monitoring network applying semi-automated full waveforms and noise-robust methods to understand their physical source mechanisms, origin and the role of potential natural and anthropogenic drivers of these seismic events. To discriminate between natural and induced earthquakes, I also analyse the spatial and temporal correlation between injections and seismic events.

Implemented methods tackle the problems of microseismicity location, seismicity clustering and microseismicity source characterization.

2. CASE STUDY: HENGILL GEOTHERMAL AREA

2.1 TECTONIC SETTING AND GEOPHYSICAL CONSTRAINTS

Iceland lies on the divergent boundary between the Eurasian and North American plates, and above a mantle plume, i.e. a hot spot under Iceland (Einarsson 1991; Wolfe et al., 1997).

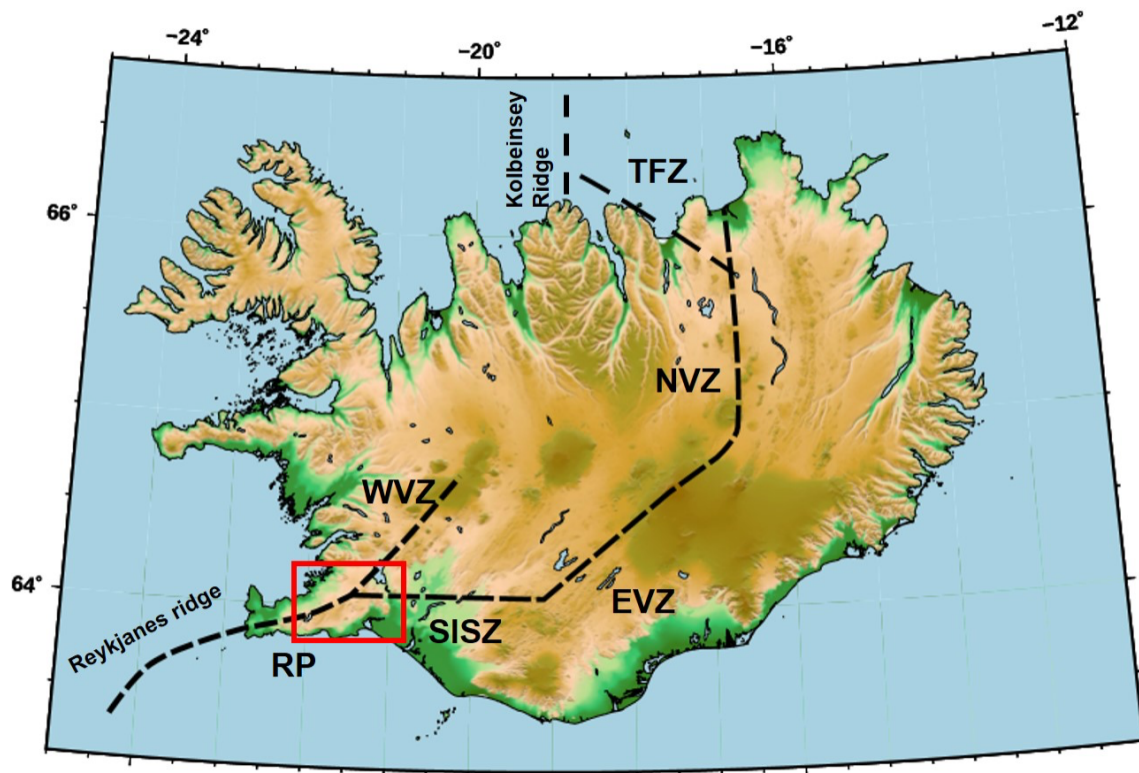


Figure 2.1 - Map of Iceland with the main tectonic zone. Red square indicates the Hengill study area.

The plate boundary in Iceland is composed of overlapping volcanic rift zones and transform zones, with active faulting and volcanism extending from southwest to the north. Plate spreading is mainly accommodated by extension across the volcanic zones and horizontal shear in the transform areas. The mid-ocean ridge bordering Iceland is represented by two submarine segments, the Reykjanes Ridge in the south and

Kolbeinsey Ridge in the north. Two major discontinuities connect these ridges and the Icelandic rift axes: the Tjornes Fracture Zone (TFZ), and the South Iceland Seismic Zone (SISZ). The TFZ is a right lateral transform zone in northern Iceland and connects the North Iceland Volcanic Zone (NVZ) and the southern end of the Kolbeinsey Ridge. The SISZ is a left lateral transform zone in southern Iceland, transferring part of crustal spreading from Western volcanic zone (WVZ) to the eastern volcanic zone (EVZ) (Einarsson, 1991, 2008). (Fig. 2.1)

The Hengill volcanic system is located in SW Iceland, at the triple junction between the Western Volcanic Zone (WVZ), the Reykjanes Peninsula (RP), which is the landward extension of the Reykjanes spreading ridge, and the South Iceland Seismic Zone (SISZ), i.e. the left-lateral transform zone (Saemundsson, 1979) (Fig. 2.2).

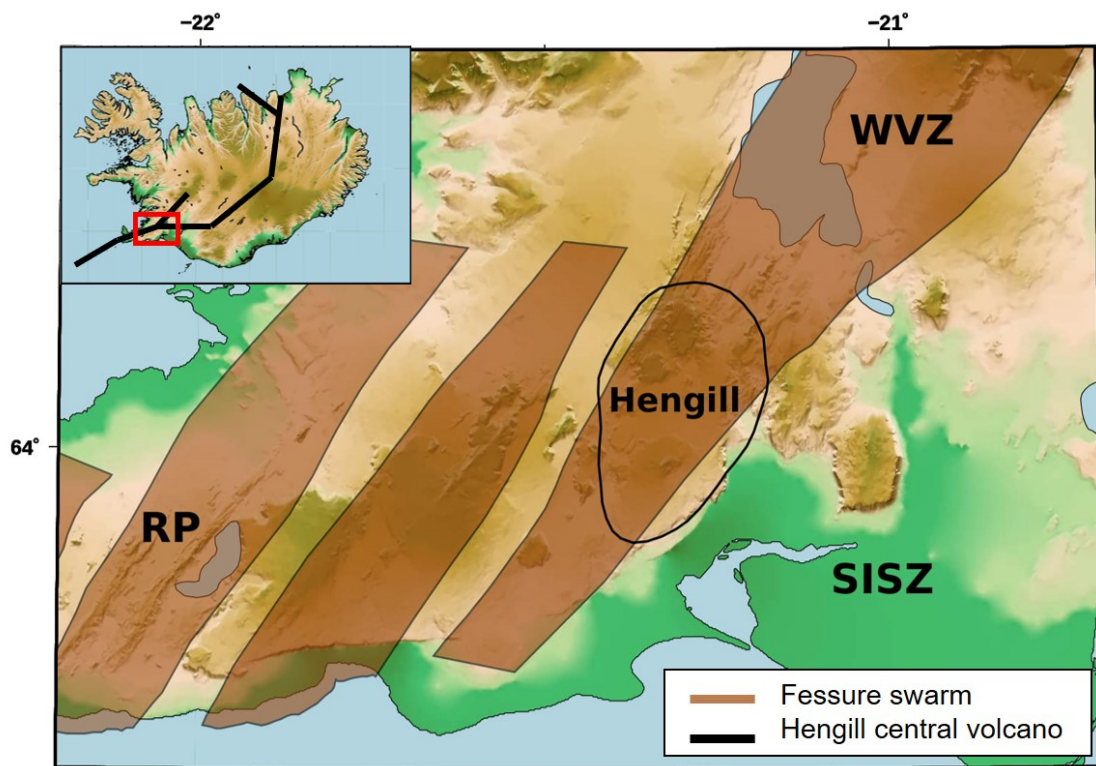


Figure 2.2 - Map of Hengill geothermal area with the main tectonic zone. Black circle indicates the Hengill central volcano and brown zones mark the fissure swarms located in the area.

The dominant tectonic trend of the area is extensional, with the distribution of major faults and eruptive fissures oriented NNE (Fig. 2.2), parallel to the accretionary zones (Toomey and Foulger 1989). South of 64°N, is marked by the SISZ, the transform zone oriented E-W with the high seismic activity; however, the largest and historical earthquakes in this

area are associated with faulting N-S striking planes, perpendicular to the general trend (Bergerat and Angelier, 2000; Eirnasson 2008).

The Hengill complex is primarily composed by three main volcanic systems, which are from SE to NW with decreasing age (0.3–0.5 My), Grændalur, Hrómundartindur (Ölkelduháls) in decline, and Hengill, with the present-day volcanic activity (Arnason et al., 2010).

The geothermal activity of area is fueled by three distinct heat sources associated with the three volcanic systems (Foulger and Toomey 1989). Tomographic studies (Foulger and Toomey 1989; Foulger et al., 1995; Jousset et al 2011) imaged three high velocity bodies which correlate well with the extinct surface eruptive sites. These three high velocity bodies have been interpreted as intrusion, representing solidified shallow crustal magma reservoirs or conduits to the surface. Foulger et al (1995) also found low V_p/V_s ratios in the near surface correlated with surface geothermal activity manifestations. A small low velocity zone underlying the presently active Hengill central volcano has been interpreted as partial melt (Tryggvason et al., 2002). Jousset et al. (2011) discovered a low resistivity/high V_p/V_s ratio area at 2.5–4 km depths interpreting this body as the heat source of geothermal activity, because it may contain supercritical fluids.

Geochemical and hydrological studies detected the maximum temperatures of three separated reservoirs: the hottest reservoir underlies the Hengill volcano ($> 310^\circ\text{C}$), a second one ($300\text{--}310^\circ\text{C}$) was detected beneath the transverse tectonic structure within the Hromundartindur system, a third one, the coolest ($270\text{--}280^\circ\text{C}$), was associated with the Grensdalur volcanic system (Foulger and Toomey 1989). On the contrary, the south Iceland Seismic Zone (SISZ), which represents the transform branch of the triple junction, lies to the south of the volcanic complex and contains low-temperature geothermal resources ($< 150^\circ\text{C}$ in the upper 1000 m) (Rognvaldsson et al 1998).

2.2 GEOTHERMAL FIELD AT HENGILL VOLCANO COMPLEX

The Hengill volcanoes were found in the late 1960s to have high potential for geothermal energy production (Gunnarsson et al., 1992). The natural geothermal activity is expressed by numerous hot springs and fumaroles spread throughout the area around the volcanic complex (Saemundsson, 1995; Arnórsson et al., 2008).

Because of its geothermal activity, the Hengill geothermal system started to be exploited for electrical power and heat production. Today, the two largest operating geothermal power plants, respectively at NE and SW of Hengill area, are the Nesjavellir and the Hellisheiði geothermal fields, where electricity and hot water are extracted (Arnason et al., 2010). Furthermore, exploration drilling has been launched at Bitra and Hverahlíd to the east and south of Hengill central volcano respectively (Hardarson et al., 2010).

Exploration drilling of the Hengill system started at Nesjavellir in 1965 with a series of geologic, geochemical and geophysical surveys of the Hengill area. Hot water production started in 1990 and electricity generation in 1998 (Arnason et al., 2010; Gunnarsson et al., 2013 b). The main drilling in the Hellisheiði field started in 2001, but prior to that some exploration wells had been drilled since 1985 (Franzon et al., 2010) first for electricity and then also for heat generation.

2.3 SEISMICITY

Due to its complex tectonic setting, the Hengill area is highly seismically active, with several thousand earthquakes located yearly.

According to previous studies (Julian et al., 1997; Miller et al., 1998; Foulger 1988 a,b, 1989; Foulger & Toomey 1989), the seismic activity at the Hengill triple junction can be mostly divided in two groups. First, infrequent intense episodes, occurring along the accretionary plate boundary and the transform zone (SISZ), outside the high temperature geothermal area. For instance, the two Mw 6.5 earthquakes occurred in June 2000 (Árnadóttir et al., 2001), and two Mw 6 earthquakes in May 2008 (Hreinsdóttir et al., 2009). These earthquakes occurred predominately on N-S orientation faults and are associated to the SISZ tectonic activity (Stefánsson and Halldórsson, 1988; Einarsson, 1991; Decriem et al., 2010).

The second activity is represented by a background of small-magnitude earthquakes ($M < 2$) occurring on a day to day. An example is the 1994-1995 swarm activity, where several thousand of seismic events with $M_L \geq 0.5$ were recorded and attributed to magma injection (Sigmundsson et al., 1997; Jakobsdóttir 2008). Some focal mechanisms available of this background seismicity show significative non double couple component (non - DC) which is related to fluid circulation in the crust (Miller et al., 1998, Foulger 1988

a, b). The other focal mechanisms are consistent with normal and strike-slip faults related to plate movements in the area. This persistent small-earthquake activity seems due either to a tensile crack formation, resulting from thermal contraction and cracking in the heat source, or to a combination of shear and tensile faulting (Foulger 1988b, 1989; Miller et al 1998; Foulger and Long 1984), or to magma injection under volcanic system (Sigmundsson et al., 1997). Therefore, the continuous micro-earthquake activity may be correlated with the geothermal and volcanic activity of Hengill region.

In recent years, with the increase in power production, seismic activity in association with drilling and fluid injection at Hellisheiði and Nesjavellir has been observed (Vogfjörð and Hjaltadóttir 2007; Ágústsson et al. 2015). The Húsmúli area, an Hellisheiði drilling site, first showed signs of induced seismicity with magnitudes up to M 2 during the drilling of some production wells in 2002 and again in 2009 (Björnsson 2004; Bessason et al., 2012). In the late 2011, after the injection started, an increase of seismic activity was observed in Húsmúli area, and on 15 October 2011 two largest earthquake of magnitude 4.0 occurred in relation to rapid changes in the injection.

3. DATASET AND SEISMIC NETWORK

A proper seismic monitoring infrastructure is a fundamental tool to analyse and understand physical processes governing induced seismicity as well as natural earthquakes. It allows to detect weak events with low signal-to-noise ratio (SNR), to obtain accurate locations, magnitudes estimation and source parameters, providing information about the related seismogenic structures. Microseismic monitoring of industrial activities has also the important role in assessing the hazard and mitigating the risks associated with induced seismicity by using dedicated tools such as the traffic light systems (Bommer et al. 2015, Broccardo et al. 2020).

In this study, I use a very dense seismic network composed by three seismic network located in Hengill area (Fig. 3.1): the regional seismic network (the SIL network), which has been in operation since 1991 (Stefánsson et al., 1993; Böðvarsson et al., 1996, 1999), permanent seismic stations installed in October 2016 by GeoSurvey (ÍSOR), and a local seismic network deployed since September 2018 with the support of GEOTHERMICA project COSEISMIQ (COntrol SEISmicity and Manage Induced earthQuakes). This project aims to monitor and control induced events and to get insight into the physics of induced seismicity. The Hengill region has been chosen as demonstration site because of its ideal conditions: there are many existing and commercially successful geothermal projects and induced seismicity is common, but it is much less of a risk governance challenge due to low population density and limited building fragility.

This local seismic network consists of 40 stations with permanent and temporary short (5 and 1 s) - and broad-band (120 and 60 s) sensors distributed within an area of about 35x35 km². Data sampling rate is 100 Hz.

The dataset used here consists of 636 events with $0.8 < M_L < 4.7$ recorded at Hengill area between 22 December 2018 and 31 January 2019 (Fig. 3.2). These data include a seismic sequence occurred at the end of December, with the M_L 4.7 mainshock that took place on 30 December 2018. Preliminary location show that the seismic sequence occurred in the southern part of Hengill geothermal site (south of 64°N), close to the transform zone.

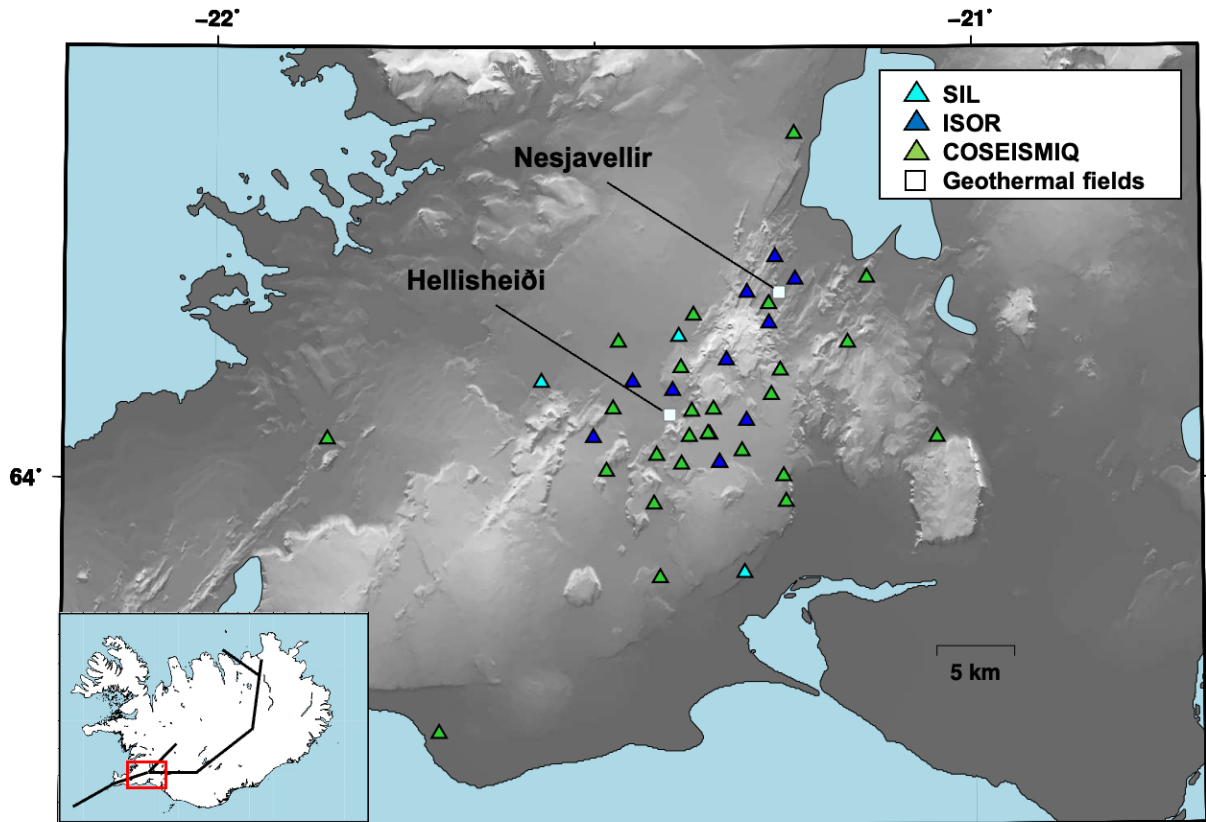


Figure 3.1 - Map of study area with three sub-seismic networks from SIL (light blue), ISOR (blue) and COSEISMIQ (green) and Nesjavellir and Hellisheiði geothermal plants (white square).

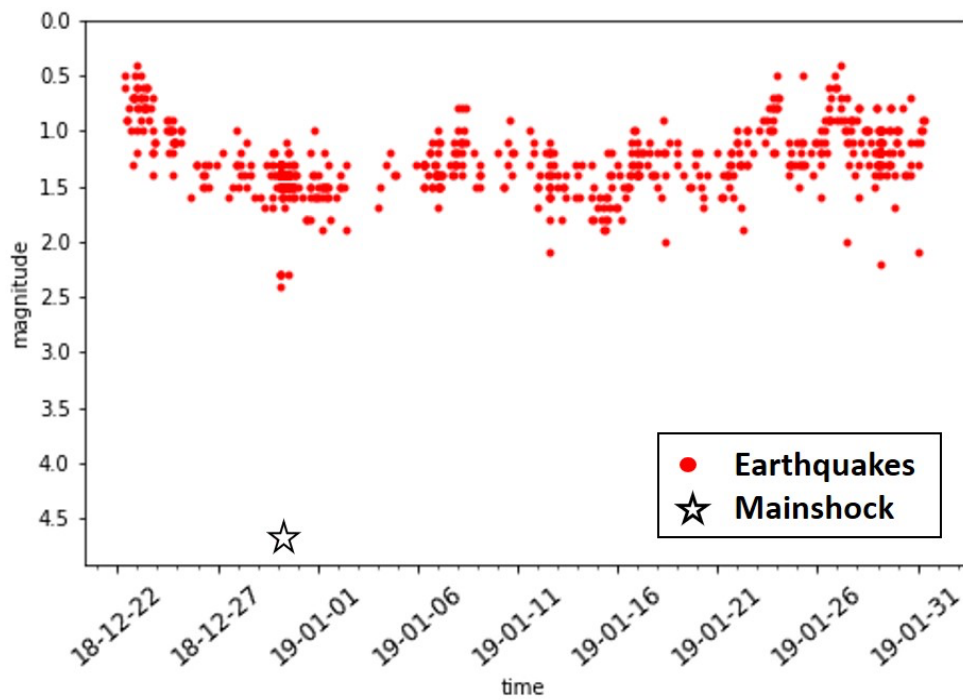


Figure 3.2 - Magnitude plot of the dataset recorded between 2018 December 22 and 2019 January 31.

Except for the M_L 4.7 mainshock, the rest of the dataset is characterized by low-magnitude earthquakes ($M < 2$), with high frequency ($f > 1$ Hz) content and noise contaminated signals. Seismic noise (frequency range of 0.2 - 0.4 Hz) strongly affects events with $M_L \sim 1$ and has more effect on the broad-band seismic stations which are sensitive to a broad range of frequencies (Fig. 3.3).

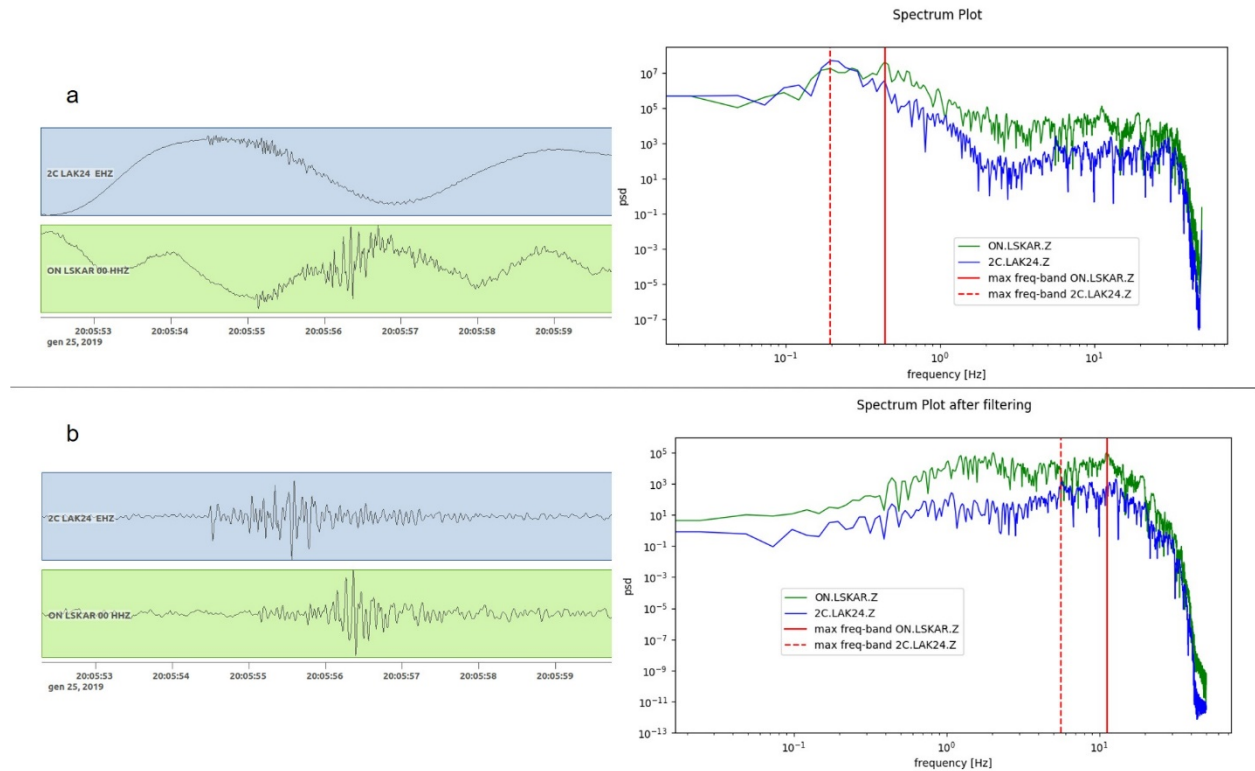


Figure 3.3 - Recorded seismograms and power spectra of the event occurred on 25 January 2019 with magnitude 1.1 in raw (a) and after filtering between 2-15 Hz (b). Green box and lines are related to short period station (LSKAR), while blue ones refer to broad-band stations (LAK24, in green). Red solid and dashed lines indicate the most energetic frequency band recorded respectively by short period and broad-band stations

Because of the high magnitude of the mainshock and its vicinity to the local network, mainshock seismic waveforms are clipped. For this reason, the earthquake source inversion for mainshock has been performed using regional seismic network (Fig. 3.4), with selected stations within a radius of 1000 km from the epicentre.

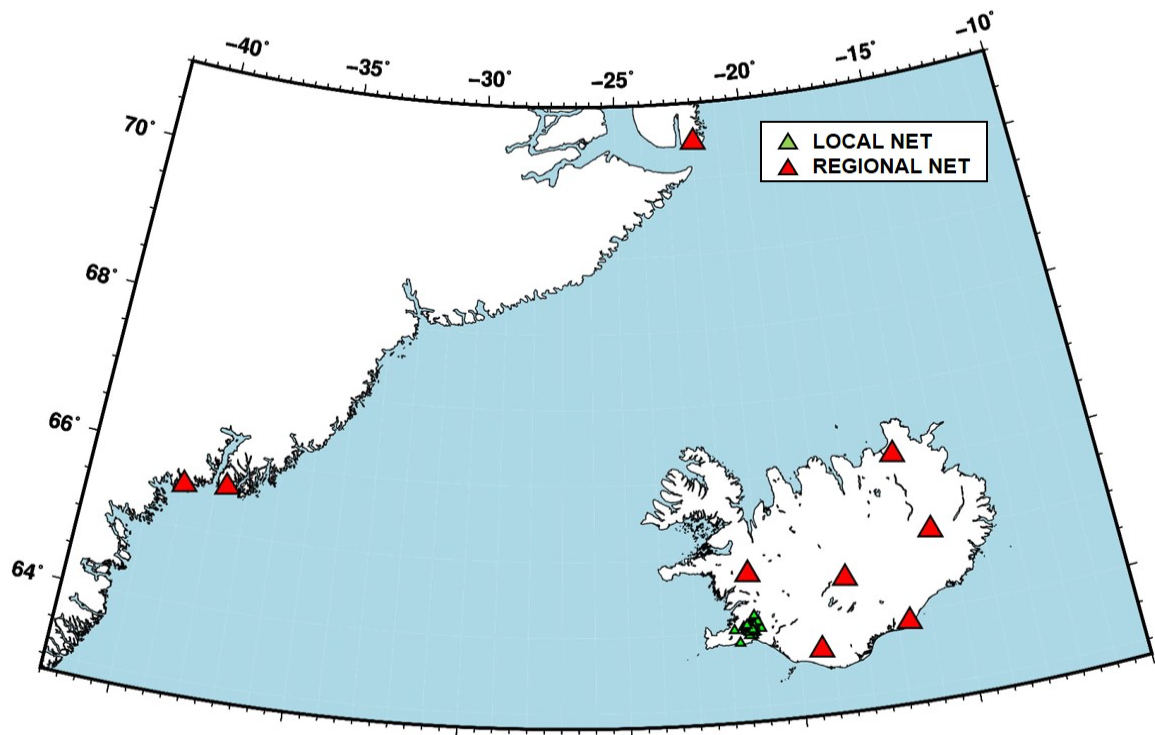


Figure 3.4 - Local (green) and regional (red) seismic networks).

4. SEISMIC EVENT LOCATION

4.1 METHOD

The problem of earthquake location consists in determining the hypocenter (latitude, longitude, depth) and origin time (start time of the rupture) of a seismic source. Essentially, the earthquake location is an inverse problem determined by the misfit between observed and predicted arrival times of seismic phases at stations for different source locations by using a given velocity model, which is usually assumed to be a representation of the true velocity structure. Considering a set of potential source locations within a volume, the hypocentral coordinates of the seismic event to be located corresponds with the one showing the smallest misfit between observed and predicted arrival times.

More formally, let suppose that an earthquake occurred at time t_0 and at position $X(x_0, y_0, z_0)$, and that the velocity model is known, the inverse problem can be written as follows:

$$d = G(m)$$

where d are our observed data (i.e. the arrival times at stations), m is the model parameters vector (i.e. space coordinates and origin time), and G is the operator that gives the predicted arrival time at each station from every value of m . Thus, the inverse problem can be posed as: given the observed arrival times, find a model that minimizes the difference between observed and calculated arrival times.

Different earthquake location techniques have been developed, and among the earliest ones I may cite graphical methods (Milne 1986), simple grid searches (Reid 1910), and the linearized inversion method (Geiger 1912) with the advent of digital computers. Earthquake location methods can be classified in different groups based on 1) spatio-temporal coordinate system, i.e. absolute and relative earthquake locations (e.g. Deichmann and Garcia-Fernandez 1992; Waldhauser and Ellsworth 2000); 2) number of events to be located, i.e. single or multiple event locations (e.g. Douglas 1967; Myers et al. 2007); and 3) the technique employed to solve the inverse problem, that can be a linearized iterative solver (e.g. Geiger 1912; Lee and Lahr 1975; Lahr 1989) or a pure non-linear approach (e.g. Tarantola and Valette 1982; Sambridge and Kennett, 1986;

Lomax et al. 2000, 2001; Sambridge and Mosegaard 2002). The selection of the methodology depends on different factors, such as the scale of application, the quality of data and the availability of detailed velocity models.

Usually, for earthquake location, the velocity structure is taken as known and fixed although it is never exactly known, creating trade-offs between seismic velocity models and earthquake parameters.

Data used to constrain earthquake locations are usually derived from seismograms recorded at seismic stations distributed around the earthquake source area. Most commonly the data set are phase arrival times (mainly the P and S onsets) and associated uncertainties picked manually or automatically from seismograms. In the last two decades a large number of picking algorithms have been developed; while P onsets can be accurately picked, the automatic picking of later seismic phases (including S onsets) is still problematic. For instance, at local and near-regional distance, the identification of S phases might be difficult, where the P coda can overlap the S wave. Furthermore, P and S picking performance is limited in the presence of noisy data, for instance in case of microseismic data characterized by a low SNR.

Alternative techniques for automated seismic event location do not require phase picking nor phase identification and directly exploit the full waveform information contained in recorded seismograms (McMechan, 1982; Gajewski and Tessmer, 2005; Ekstrom, 2006; Kao & Shan, 2004, 2007; Baker et al., 2005; Drew et al., 2005; Gharti et al. 2010; Liao et al., 2012; Grigoli et al., 2013, 2014). Among these methods, the source scanning algorithm (SSA; Kao & Shan, 2004, 2007) is one of the most popular. Basically, the SSA is a systematic grid-search method that performs the source location using a brightness function, which is obtained by stacking the absolute amplitudes of normalized seismograms recorded at different stations along the predicted traveltimes of a given seismic phase from each assumed source location. Several modified versions of SSA algorithm have been proposed with different stacking functions; for instance, at a microseismic scale, Gharti et al. (2010) and Zeng et al. (2014) applied a waveform envelope-stacking approach using both P and S phases.

For this application, the location of seismicity in the Hengill area has been obtained by using the LOKI algorithm (Location of seismic events through traveltimes staking, Grigoli et al. 2013), a modified version of Source Scanning Algorithm (SSA; Kao & Shan, 2004) method and specifically designed for microseismic monitoring.

To explain how LOKI works, let us suppose that a seismic event occurs at the location indicated by the yellow star in figure 4.1 (a1) and recorded by a linear array of n receivers deployed at the surface. To locate an event, LOKI uses non-negative processed waveforms (that I call stacking functions) based on the Short Time Average to Long Time Average ratio (STA/LTA) traces of all available stations.

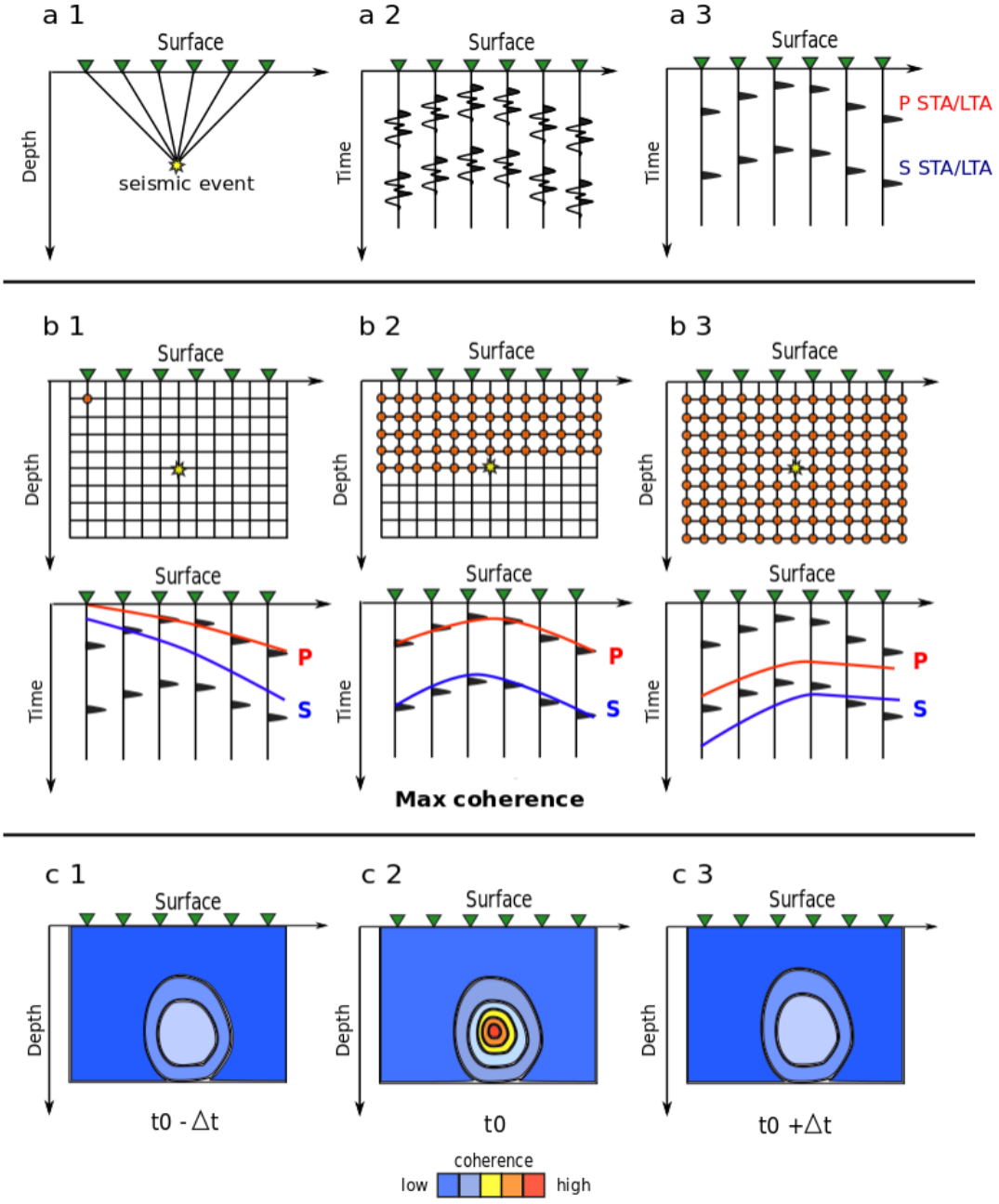


Figure 4.1 - LOKI location process: a) seismic event recorded by n receivers deployed on surface (a1), raw (a2) and processed STA/LTA traces for P and S waves (a3). b) waveform staking process for different source location and time steps (b1, b2, b3). c) Coherence matrix computed for each source location each potential source location (c1, c2, c3) whose maximum corresponds with the hypocenter and origin time (t_0) of the seismic event (c2).

Thus, the algorithm first compute two characteristic functions, a first one sensitive to the P-phase onset and a second one sensitive to S-phase arrival. The P characteristic function is defined as energy of vertical component of seismic trace, whereas the S characteristic function is maximum eigenvalue of the instantaneous covariance matrix of the horizontal components traces (Fig. 4.1 a3). Then, STA/LTA traces, i.e. the ratio of short- to long-term energy, of P and S phases are computed separately.

Once the stacking-function is obtained, to locate an event we need to define a 3D cartesian grid space containing the seismogenic zone, where each grid point represents a potential source location (x, y, z) (Fig. 4.1 b1). For each potential source location (x, y, z) , the theoretical arrival times for the first P $[\tau_i^P(x, y, z)]$ and S $[\tau_i^S(x, y, z)]$ onset at all n stations (i is the station index) are computed. Then τ_{min} and τ_{max} are defined as:

$$\tau_{min}(x, y, z) = \min \{[\tau_i^P(x, y, z)]_{i=1}^n\} \quad (1)$$

$$\tau_{max}(x, y, z) = \max \{[\tau_i^S(x, y, z)]_{i=1}^n\} \quad (2)$$

Which define for each potential source location the minimum P- and maximum S- arrival time in the network. Then, the computed arrival times at station i for P and S first onset $T_i^{P,S}(x, y, z)$ relative to τ_{min} and shifted by a delay t are computed:

$$T_i^{P,S}(x, y, z) = \tau_i^{P,S}(x, y, z) - \tau_{min} + t = \tau_i^{P,S}(x, y, z) + t_0 \quad (3)$$

t_0 is the origin time of the event, which is equal to $t - \tau_{min}(x, y, z)$.

I then evaluate the coherence functions C^P and C^S at each source location (x, y, z) and origin time t (Fig. 4.1 c1, c2, c3), by using the following equation:

$$C^P(x, y, z, t) = \sum_{i=1}^N W_i^P [t + \Delta T_i^P(x, y, z)] \quad (4)$$

$$C^S(x, y, z, t) = \sum_{i=1}^N W_i^S [t + \Delta T_i^S(x, y, z)] \quad (5)$$

where W_i^P and W_i^S are respectively the STA/LTA of P and S characteristic functions related to the i -th station. Waveform normalization is generally required to remove the attenuation effect due to the geometrical spreading: in this way we avoid that stations

close to the source dominate the stacking. The coherence function of the two seismic phases is finally defined as:

$$C(x, y, z, t) = \frac{\sqrt{C^P(x, y, z, t)C^S(x, y, z, t)}}{n} \quad (6)$$

where C^P and C^S are the coherence functions for P and S waves and n is the number of stations. This function is bounded between 0 (no coherence) and 1 (perfect coherence for both P and S phases). Therefore, coherence value provides a direct estimation of earthquake location.

This process is iterated performing a grid-search for different time step and source location (Fig. 4.1 c1, c2, c3). At the correct location and time step (Fig. 4.1 b2), the waveforms stacking process gives an absolute maximum in terms of coherence, $\max\{C(x, y, z, t)\}$, corresponding to the earthquake coordinates (Fig. 4.1 c2).

The uncertainties of solutions are estimated by a) repeating the location procedure after perturbing the STA/LTA parameters (i.e. the length of both long- and short- time windows, b) repeating location process after removing, each time, all traces related to different station (jackknife method). Thus, by repeating this procedure k times, we obtain k estimation for each model parameter (i.e. hypocenter location). Then, from the location distribution, weighted mean and standard deviation are computed. The largest value of the coherence function related to h .th iteration is used as weighting factor:

$$q_h = C_h(x_h, y_h, z_h, t_{0h}) \quad (7)$$

Where C_h , q_h , (x_h, y_h, z_h, t_{0h}) are respectively the coherence function, the weighting factor and the hypocenter estimation related to h -th solution.

After the k -th iteration the normalized weighing factor is composed as:

$$Q_h = \frac{q_h}{\sum_{m=1}^k q_m} \quad (8)$$

The weighted average of all k solution is the best estimation of hypocentral coordinates:

$$\bar{x}_i = \sum_{m=1}^k Q_m \hat{x}_{im} \quad \text{with } i = 1, 2, 3 \quad (9)$$

Where $\hat{x}_{im} = \hat{x}_m, \hat{x}_{2m} = \hat{y}_m, \hat{x}_{3m} = \hat{z}_m$ and $\hat{x}_{4m} = \hat{t}_{0m}$. Uncertainties information can be directly extracted from the covariance matrix R defined as:

$$R_{i,j} = \frac{\sum_{m=1}^k Q_m}{(\sum_{m=1}^k Q_m)^2 - \sum_{m=1}^k Q_m^2} \times \sum_{m=1}^k Q_m (x_{im} - \bar{x}_i)(x_{jm} - \bar{x}_j) \quad (10)$$

with $i = (1, 2, 3, 4)$ and $j = (1, 2, 3, 4)$.

4.2 APPLICATION TO THE HENGILL DATASET

Since the dataset is composed by local low-magnitude event recorded by both broadband and short period station and characterized by high frequency content and noisy signal a high-pass filter is used (see section 3). Thus, to increase the SNR, I applied a bandpass filter from 2 to 15 Hz to the entire dataset (Fig. 4.2).

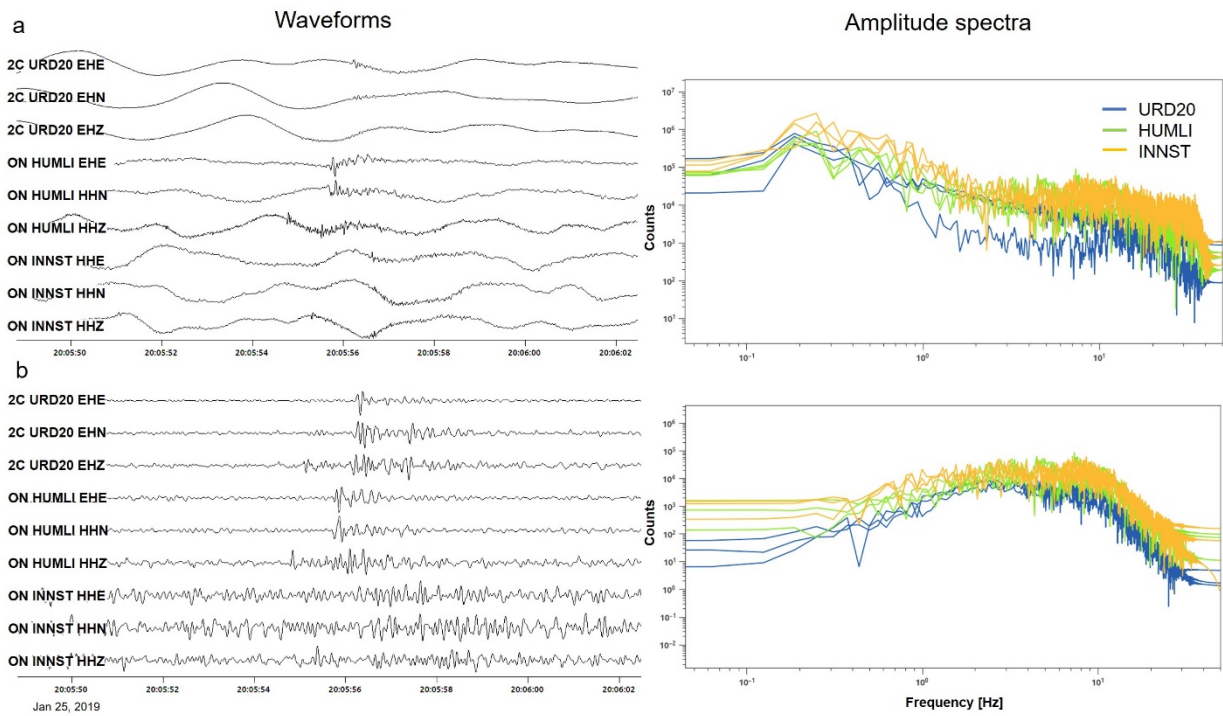


Figure 4.2 - Examples of unfiltered (a) and filtered (b) Waveforms and amplitude spectra of an event occurred on January 25 with $M_L = 1.0$ recorded at three different stations.

Before analysing the whole dataset, I first tested three different velocity models available for the Hengill area (Fig. 4.3): two local velocity models from Icelandic Meteorological Office (IMO) (Kristín Vogfjörð and Sigurlaug Hjaltadóttir, 2007), and a third one extracted from Tryggvason et al. (2002). Thus, I computed earthquake locations comparing the performance of the three velocity models with a small dataset consisting of ~50 seismic events homogeneously distributed within the target area.

In analogy, with the velocity analysis performed in seismic reflection applications, the coherence among waveforms can be used to evaluate the “goodness” of a particular velocity model with respect to other ones. While RMS values strongly depend on the quality of pickings and on the number of phases considered, the use of coherence values and waveform-based techniques (which are free from phase picking) allows to automatize this step and provide robust comparison of the quality of different velocity models.

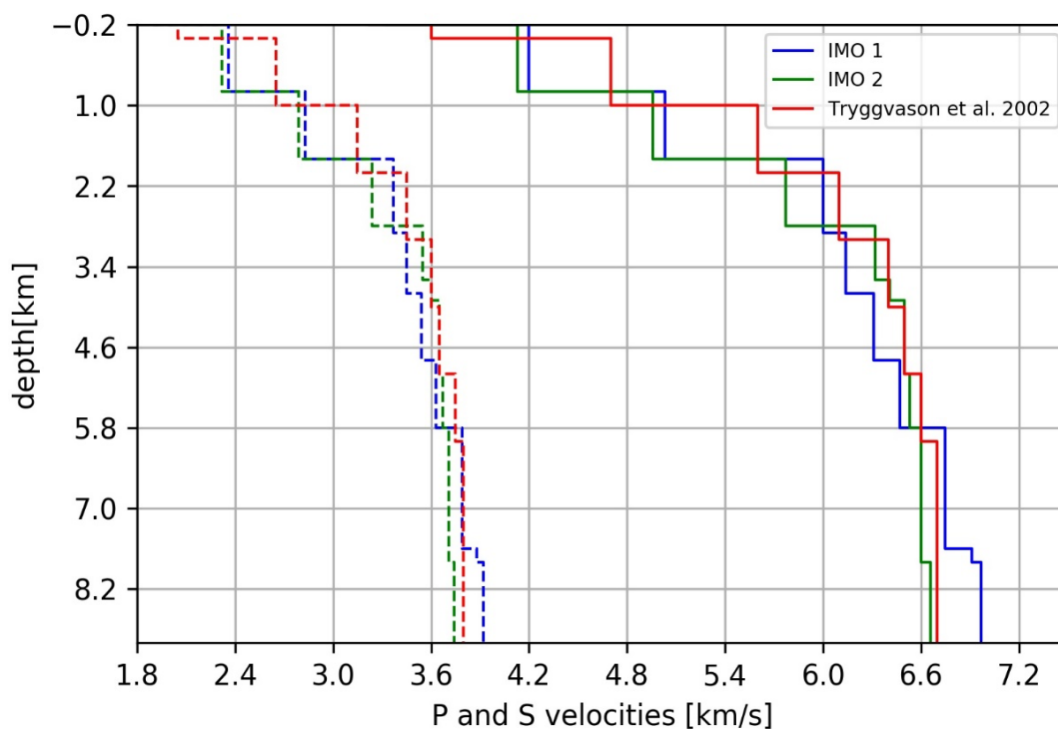


Figure 4.3 - Three different 1-D velocity models for P (solid lines) and S (dashed lines) waves.

To compute P and S travel-times for each velocity model, I used the Eikonal finite difference scheme of Podvin and Lecomte (1991) implemented within NonLinLoc (Lomax et al. 2000).

Taking into account the size of seismogenic zone, I defined a 3D cartesian grid space set to 136x126x50 km³ with 0.4 km grid spacing. For each possible trial source location, the theoretical arrival times for P and S onset at all 40 stations of the recording network are computed. The STA/LTA traces were computed using a short-time window length in the range of 0.1 - 0.15 s, the long-time window is twice as long. Uncertainties have been estimated by random perturbations (5 times) of STA and LTA windows length ranges. Hence, based on maximum estimated coherence values, providing direct information of the best estimation of hypocentral location, I choose the best velocity model and then perform the location of all 636 earthquakes.

4.3 RESULTS

On the basis of the maximum estimated coherence values, I have chosen the best velocity model; the higher values of coherence belong to locations computed using the Tryggvason et al. (2002) velocity model (Fig. 4.4).

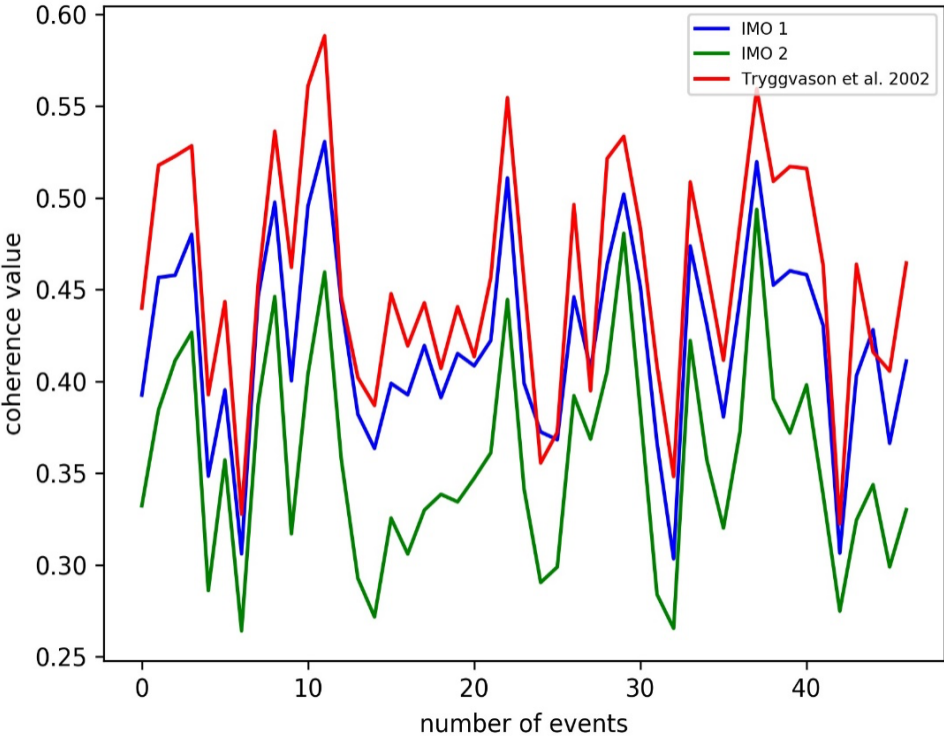


Figure 4.4 - Coherence values of three velocity models. The Tryggvason et al. (2002) model reports the highest values of coherence

The appendix A shows the catalogue of all 636, specifying date, latitude, longitude and depth (in km). The average of maximum coherence value is of about 0.6.

Figure 4.5 shows an example coherence matrices XY, XZ, and YZ related to the earthquake occurred on 2018 December 30 with $M_L = 1.6$; coherence values are represented in color scale, showing a clear absolute maximum.

Uncertainties of solutions, as standard deviation, and the comparison of location results with those obtained with manual procedure are shown in figure 4.6; ~ 80% of automated located events are within 1 km from the reference manual location.

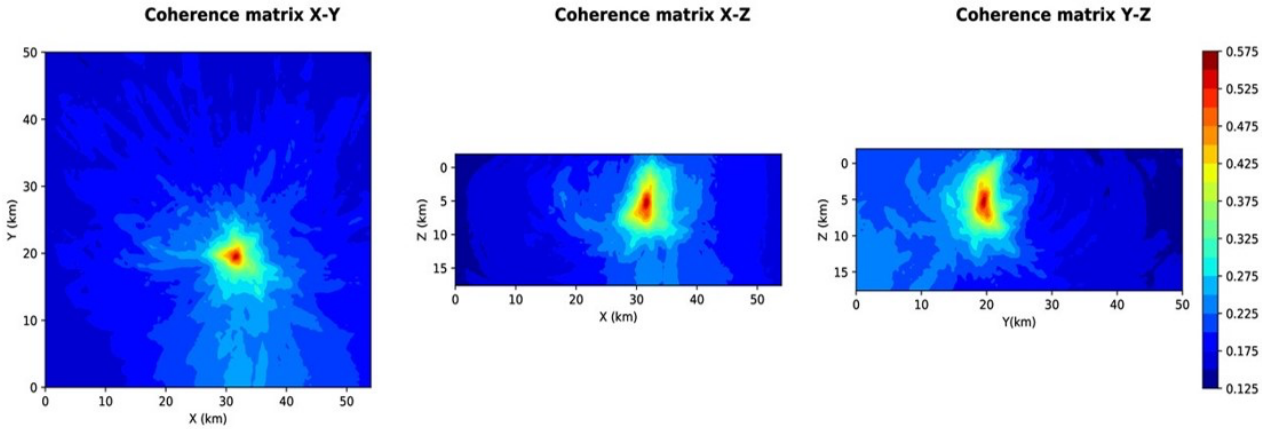


Figure 4.5 - Example of coherence matrix related to M_L 1.6 earthquake occurred on 30 December 2018. The coherence matrix XY is obtained by projecting, for each (X, Y) point, its maximum along Z direction (coherence matrices XZ and YZ are obtained in similar way). Coherence values are represented in colour scale

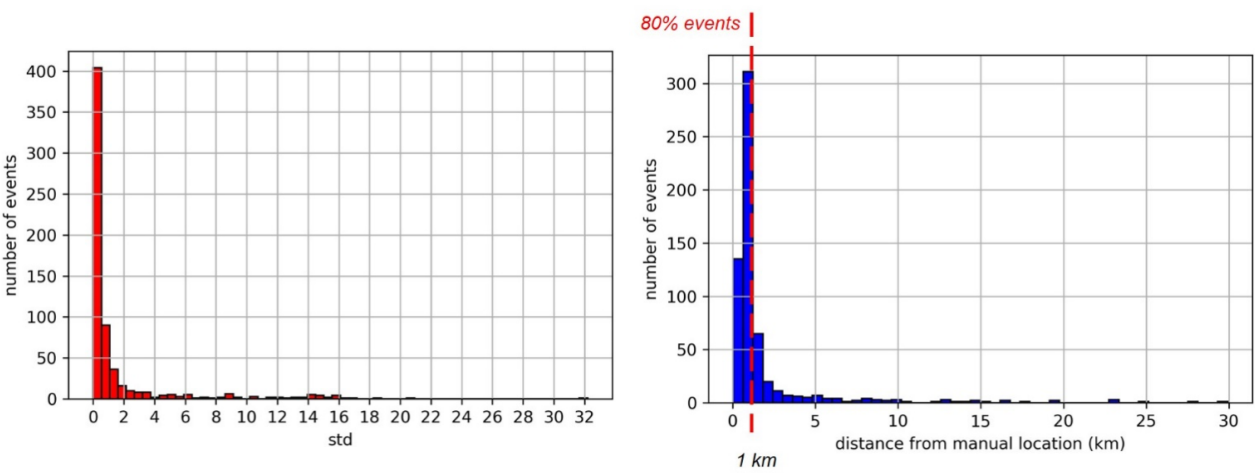


Figure 4.6 - Histogram plots show 1) the number of events automated located (blue bars) within a given distance from the manual locations (on the left) and 2) standard deviation of results (red bars, on the right).

Figure 4.7 shows the map with located events and two orthogonal vertical cross-sections along latitude and longitude. Events are color-coded according to their depth. Seismicity appears clustered with most of hypocentre-depths distributed between 1 and 8 km. In particular, shallower events (with hypocentre < 4 km) are mostly located in the geothermal area, whereas most of deeper events appear as a big separate cluster in the southern part of the area, in the neighbouring SISZ.

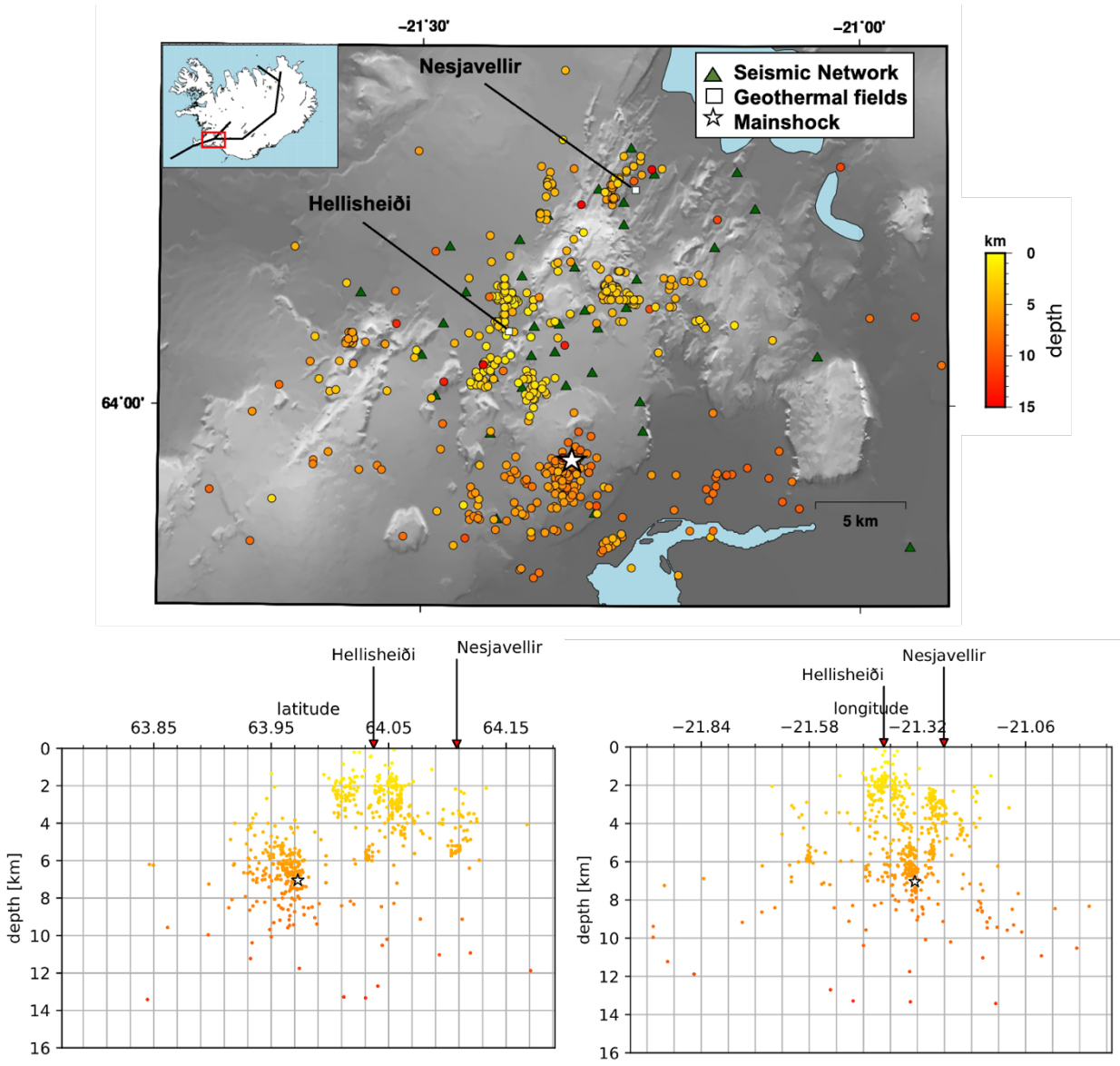


Figure 4.7 - Map and two orthogonal NS and EW vertical sections of 636 earthquakes occurred between 2018 December 22 and 2019 January 31. Located seismic events are color-coded according to depth, the mainshock is marked by the star, arrows in vertical sections indicate the location of Hellisheiði and Nesjavellir geothermal plants, the coloured triangles represent the seismic stations of different networks.

Thus, based on hypocentral distribution, the seismicity can be divided in two main group. The first group is composed by shallower events (depth < 4.0 km) located in the center of geothermal area and in the proximity of geothermal fields. The second group is deeper (depth > 4.0 km), located south of the geothermal site, and close to the transform zone (SISZ), where the M_L 4.7 sequence took place and larger historical earthquakes occurred (Árnadóttir et al., 2001; Hreinsdóttir et al., 2009).

The cumulative plot (Fig. 4.8) shows the standard deviation of locations of the two depth-groups: shallow events (in red), mostly located in center of geothermal site, have lower values of uncertainties than deep events (in green), located at the edge of geothermal site. Shallow events are better constrained by all network, highlighting that the quality of solutions also depends on the number of stations used for the STA/LTA stacking process and on the position of earthquakes with respect to seismic network.

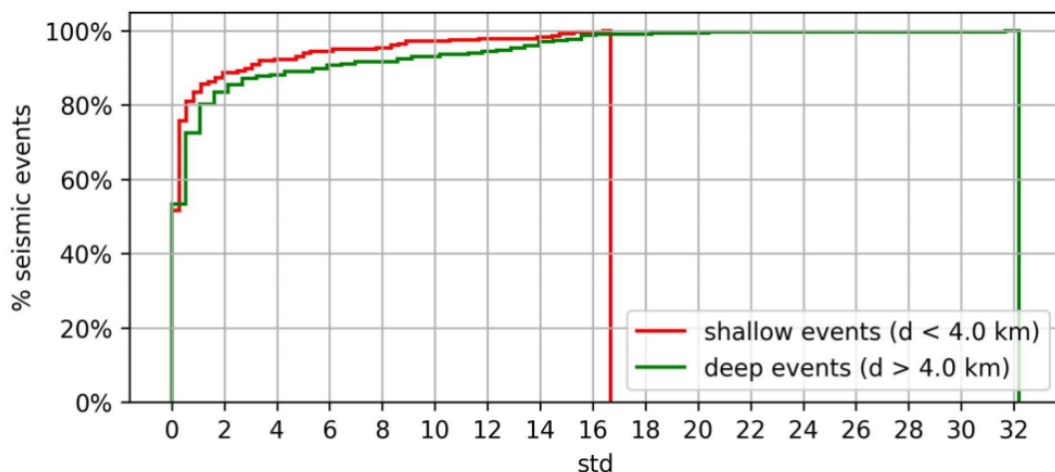


Figure 4.8 - Cumulative plot shows the standard deviation of the location results for shallow in-network (in red) and deep outside-network (green) events

5. CLUSTERING ANALYSIS

5.1 METHOD

Seismic clustering algorithms allow to automatically classify earthquakes, identifying groups of objects (clusters) with similar seismic attributes.

In recent years, the growing interest in microseismicity monitoring led to deploy dense local networks for improving earthquake detection. As a consequence, the seismic catalogues are becoming increasingly large. From this point of view, clustering analysis can be applied to large dataset to automatically detect earthquakes with similar features, such as hypocentral locations, origin times, magnitudes, or focal mechanisms.

Several seismic clustering approaches exist and are used to different purposes in different field, with broad literature of their application. In general, clustering approaches differ in type of algorithm (e.g. hierarchical clustering, k-means clustering, density based clustering) and metrics to be used; for instance spatial location (Ouillon & Sornette 2011; Konstantaraset al.2012; Lippiello et al.2012; Schaefer et al.2017), temporal evolution (Kagan & Knopoff 1976; Kagan & Jackson 1991), waveform similarity (Maurer and Deichmann1995; Cattaneo et al.1999; Wehling-Benatelli et al.2013), focal mechanism similarity (Kagan 1991; Willemann 1993; Moriya et al.2003; Cesca et al., 2014, 2016, 2020a). Alternative approaches combining different earthquake metrics have been also proposed (Hainzlet al. 2000; Sornette & Werner 2005; Lasocki 2014; Lizurekand Lasocki 2014; Zaliapin et al. 2008).

Here, I performed a spatial (hypocentral) and waveform-based clustering using SEISCLOUD, a tool for seismicity clustering (Cesca 2020b) based on the DBSCAN clustering (Density-Based Spatial Clustering of Applications with Noise, Ester et al., 1996).

DBSCAN identifies clusters as high-density regions, where the items to be clustered (i.e. earthquakes) are located close together, and marks as outliers those items which lie in low density regions. The performance of DBSCAN is controlled by two parameters controlling the density threshold: N_{min} parameter identify the minimum number of neighboring items, and ϵ parameter defines the maximum acceptable distance. A cluster is formed if there exist an item i and at least N_{min} other items j with a distance $d_{i,j} < \epsilon$ (Fig. 5.1). Item i is defined as core item, while items j represent density-reachable items

from core item i . If items j have a sufficient number of neighbours (i.e. they lie in a density region), they are also core items, while if they lie in lower density regions, they are so called edge items (Fig. 5.1 c). Both core and edge items will be assigned to a cluster. If an item is neither located in densely populated regions, nor is density-reachable from a core item, it is defined as isolated item. Isolated items are basically located in low density regions and represent outliers.

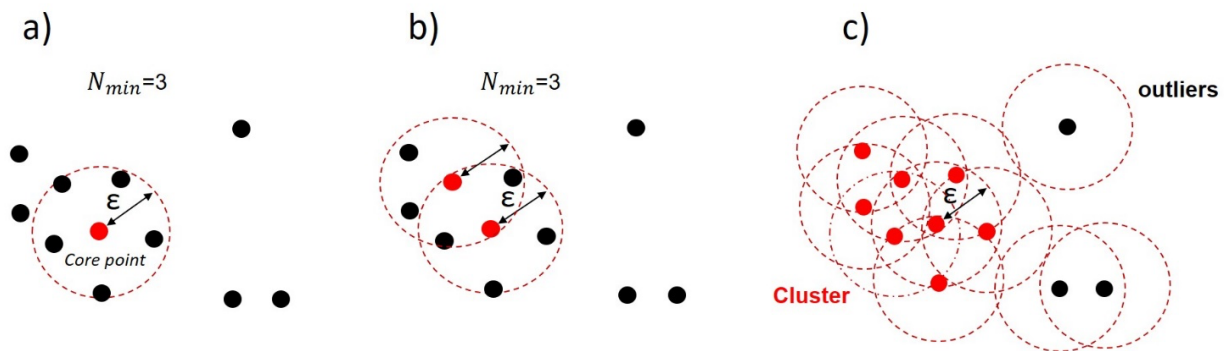


Figure 5.1 - DBSCAN method: a) definition of N_{min} and ϵ parameters and the core point; b) starting to create a cluster; c) identification of cluster and outliers

The number, size, and heterogeneity of the resolved clusters, as well as the fraction of unclustered items are controlled by the choice of N_{min} and ϵ parameters: if the chosen ϵ and N_{min} are too small most data will not be clustered at all (and labelled as -1 for “noise”), if they are chosen too large, close clusters might be merged into one cluster, and eventually the entire data set to be returned as a single cluster. However, the selection of ϵ and N_{min} parameters depends on the purpose of our problem, data, and metric to be used.

SEISCLOUD offers different metrics to estimate the distance among earthquakes (Cesca 2020), based on the similarity of their hypocenters, time, focal mechanisms, or waveforms. The DBSCAN implementation relies on normalized distance values between 0 (equal items) and 1 (very different items). For some metrics, where the distance is defined over a finite interval, the normalization is unique. An example is the use of waveform correlation as a measure of earthquake similarity: a cross-correlation equal to 1.0 (perfectly correlation) and -1.0 (anti-correlation) will map into normalized distances

of 0.0 and 1.0, respectively. In other cases, where a maximal distance cannot be defined (for example, when considering the spatial or time difference among two earthquakes), we will assign the maximum normalized distance 1.0 to all spatial or temporal differences, which are equal or larger than a given threshold (e.g., default thresholds are 1000 km for spatial distances and 365 days for the temporal distance).

5.2 SPATIAL AND WAVEFORM CLUSTERING AT HENGILL AREA

I performed the spatial clustering considering the hypocentral coordinates (latitude, longitude, and depth) as metric. Since I am dealing with local microseismicity in a small study area (latitude range 63.9 - 64.1 and longitude range -21.00 - 21.6, depth range=0 - 11 km), the hypocentral distance among earthquakes is small and some clusters are visible even without clustering analysis. Thus, to define a cluster, I set a minimum of 10 neighbouring earthquakes within 1 km distance ($N_{min} = 10$, $\epsilon = 1$ km).

Once spatial clusters are identified, I performed a waveform-based clustering to assess the waveform similarity among events belonging to the same cluster (i.e. events with similar location). Given that similar waveforms denote earthquakes with similar location and focal mechanism, and that the spatial clustering already identified earthquakes with neighbouring hypocenters, this analysis aims to identify potential families of microearthquakes with different mechanism at a similar location, which may reflect the activation of different faults or fault segments.

I computed the waveform cross correlation, as a measure of earthquakes similarity, using only P and S body waves, because of the seismic noise and the high frequency content of the seismic signal. Therefore, for each cluster I first selected stations with good signal to noise ratio, covering as much homogeneously as possible the cluster area. Note that different stations have been used for different spatial clusters. Then, I picked P and S phases on the vertical and horizontal components of recorded seismograms, respectively. For each station-cluster pair, I computed two cross correlation matrices, for P and S waves separately. The P-cross correlation matrix has been computed by taking the maximum of cross correlation traces of P waves recorded on vertical component. To get the S-cross correlation matrix, first I added up the cross-correlation traces computed for

the East (cc_E) and North (cc_N) components, obtaining the total cross correlation trace of horizontal component (cc_{tot}), and normalized it:

$$Norm = \frac{cc_E + cc_N}{(\sqrt{\sum(tr1_E)^2 \times \sum(tr2_E)^2}) + (\sqrt{\sum(tr1_N)^2 \times \sum(tr2_N)^2})} \quad (11)$$

where $tr1$ and $tr2$ are the waveforms of two different events recorded on E and N components of one selected station.

To normalize distance values between 0 (perfect correlation) and 1 (anti-correlation), I computed the P and S distance matrices (S_m) as following:

$$S_m = 1 - (0.5 \times (cc_m + 1)) \quad (12)$$

The two distance matrices are used as inputs to perform the waveform clustering with SEISCLOUD. I set the ϵ parameter from 0.05 (cross-correlation 0.9) to 0.1 (cross-correlation 0.8) for each cluster, according to the quality of SNR. The minimum number of samples to create a cluster (N_{min}) is based on the number of events recorded by selected stations of the cluster (Table 5.1).

5.3 RESULTS

The spatial clustering identifies eight clusters (see Table 5.1 and Fig. 5.2), highlighting that shallower clusters are located in the central part of the study region, in the vicinity of one geothermal plant. Conversely, deeper clusters are mostly located at the edge of geothermal site. In particular, the largest and deepest cluster (red dots in Fig. 5.2), where the major seismic sequence occurred, is further south respect to other clusters, and its depth-trend shows an E-dipping (see vertical section in Fig. 5.2).

The parameters set for the spatial clustering mark well the outliers (black dots in Fig. 5.2) as those events located in a low-density region (see 5.1 section), quite distant respect to the eight clusters.

Table 5.1 - Results and parameters of spatial and waveform clustering

Spatial clustering				Waveform clustering				
Spatial cluster	Depth mean	Max magnitude	tot n° events	selected stations	n° events of selected station	ϵ	Nmin	n° waveform family
1	6.30	4.58	124	MEI05, NUP27, KAP01	82	0.05	8	1
2	3.03	2.2	80	GAN02, INNST, NUP27	80	0.05	8	1
3	1.93	1.87	69	EDA, GAN02, INNST, GRH43, URD20	61; 62; 69	0.1	6-7	1-2
4	2.35	1.3	28	GRH43, MEI05, NUP27, THU04	22-27	0.1	3	1
5	2.28	1.4	27	BLK22, LSKAR, MEI05, URD20	27	0.1	3	1
6	5.31	0.99	25	EDA, GAN02, GRAFN, OLF42	22;25	0.1	3	1-2
7	5.7	1.62	19	KRIST, SAN	18; 19	0.05	2	1
8	3.68	1.3	14	EDA, GRAFN, INNST, VAL41	14	0.1	2	1-2

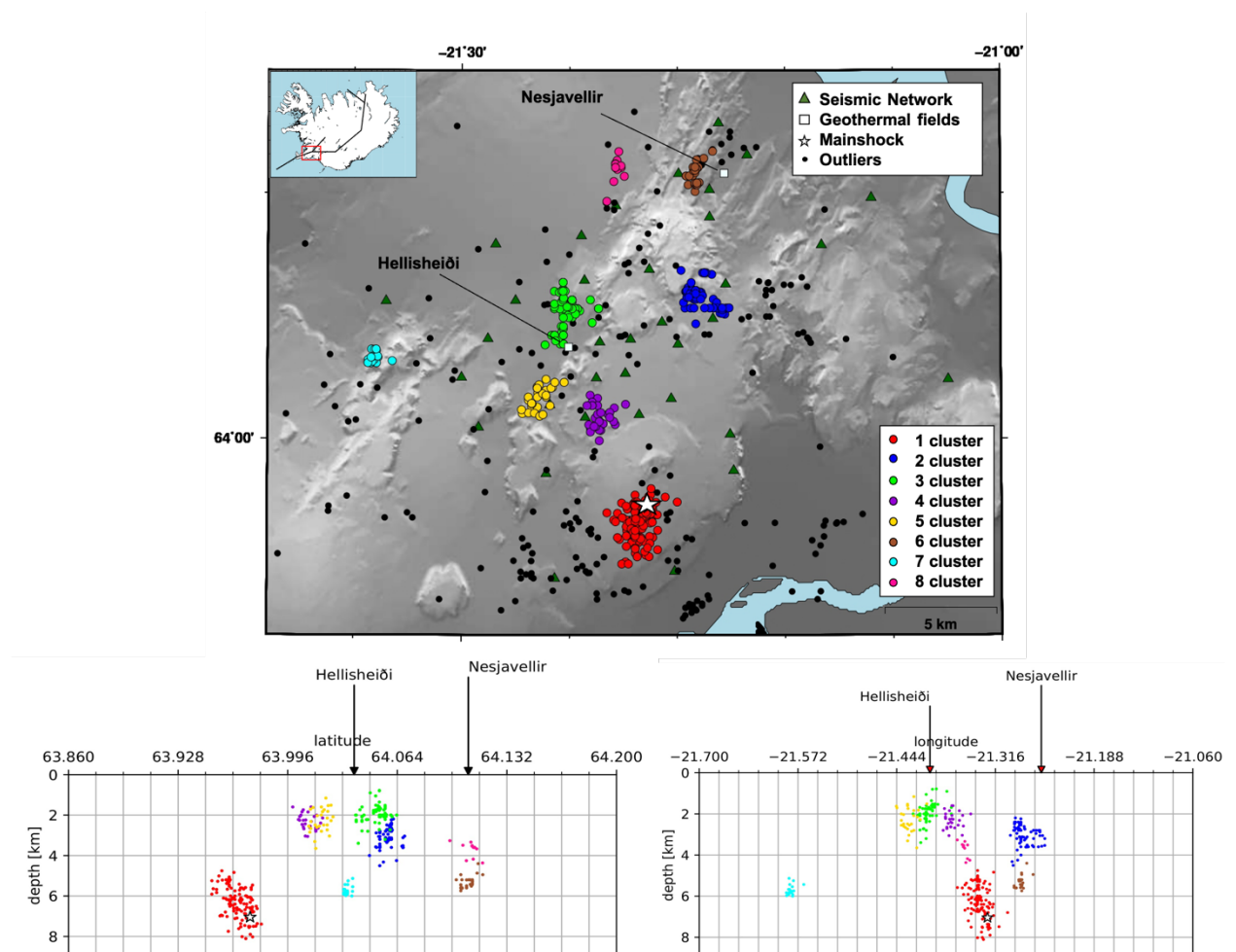


Figure 5.2 - Map and two orthogonal NS and EW vertical sections of computed spatial clustering. Clusters are marked with eight different colours whereas the outliers with black. The mainshock is represented by the white star.

Most of waveform clustering results confirmed the presence of a single family of events, with similar waveforms (see last two columns of Table 5.1). A nice example is the cluster 1 result (Fig. 5.3), where the hypocentral similarity matrices for P and S phases clearly show one waveform family recorded by station MEI05.

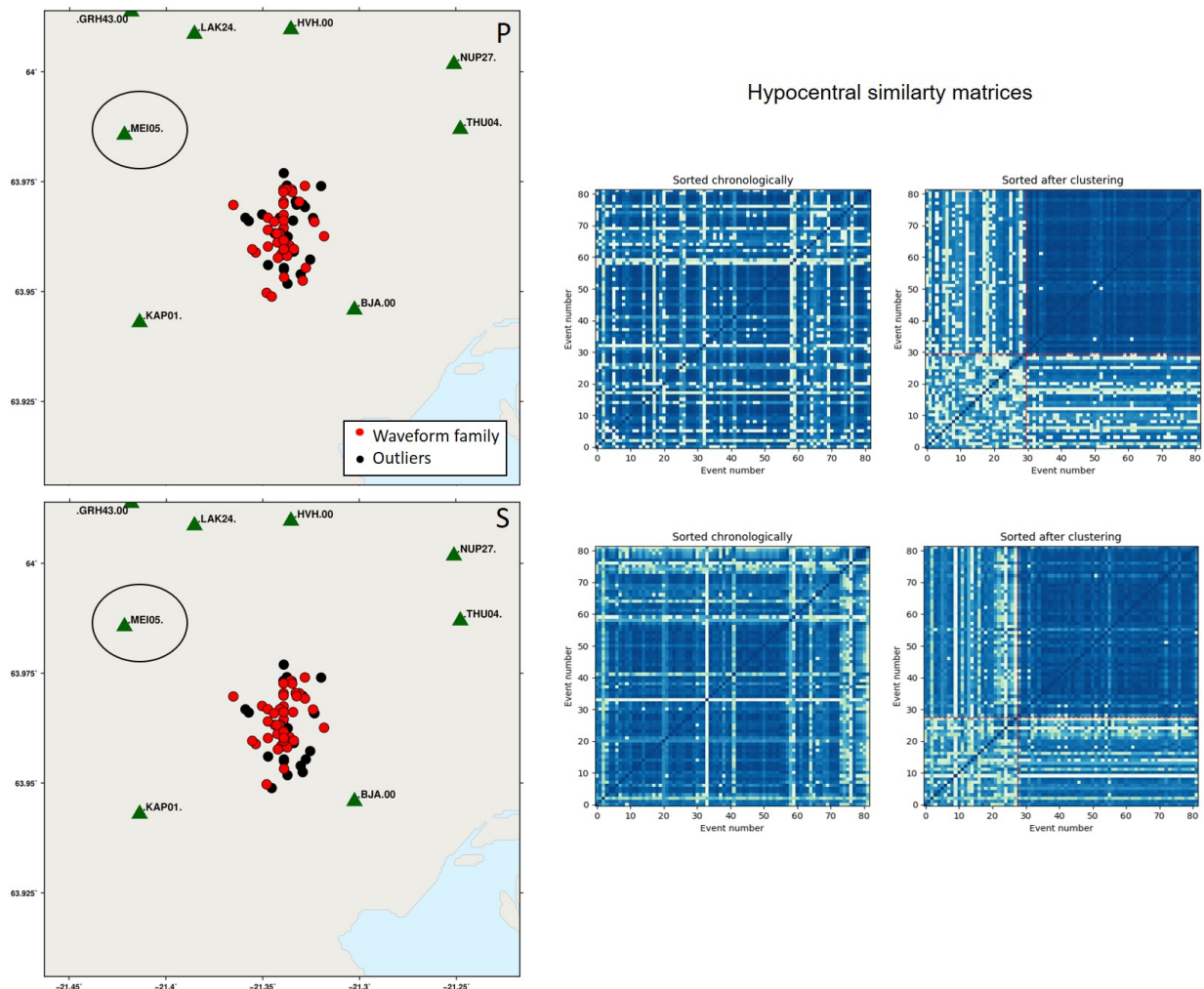


Figure 5.3 - Example of waveform clustering results for P and S waves with maps (left side) and hypocentral similarity matrices (right side) of cluster 1 for MEI05 station.

Even cluster 7 show one clear waveform family, as well as waveforms for clusters 2,4,5, despite their noisier signals.

For the remaining clusters (clusters 3, 6 and 8), results are less clear, as waveforms at some stations, show highly similar waveforms, but waveform at other stations show larger differences and hypothesize the presence of at least two families in each of these

clusters. An example is the cluster 3 (Fig. 5.4), where the hypocentral similarity matrices for P waves shows two waveform families. This result, however, could also be related to a particular cluster-station geometry and the source radiation pattern.

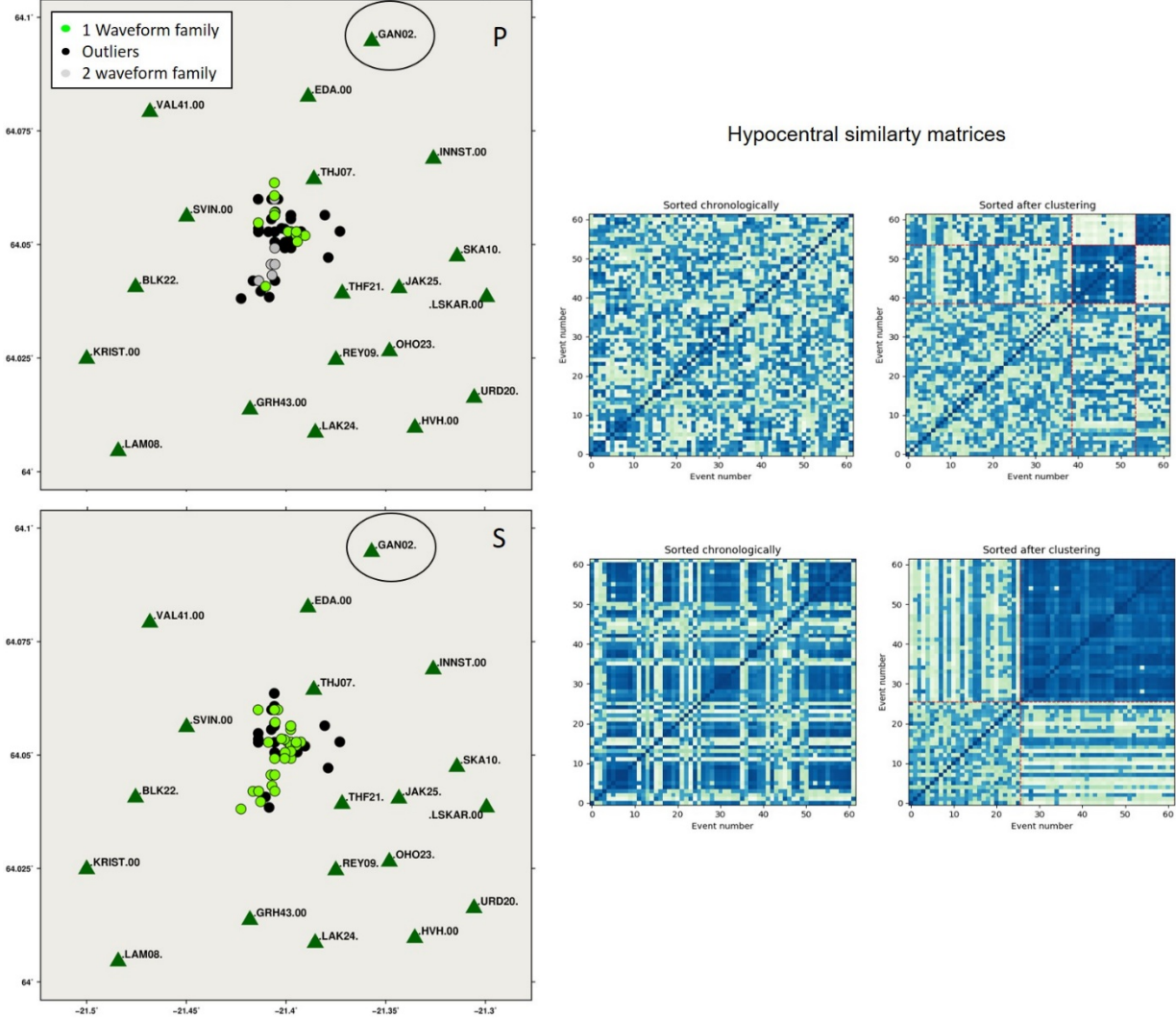


Figure 5.4 - Example of waveform clustering results for P and S waves with maps (left side) and hypocentral similarity matrices (right side) of cluster 3 for GAN02 station

6. MASTER EVENTS IDENTIFICATION AND RELATIVE MAGNITUDE ESTIMATION

Most of the dataset consists of small magnitude events with high frequency content and noisy recorded signal. Thus, to perform the earthquake source inversion, for each spatial cluster I identified several master events, i.e. well-located events with small location uncertainties, high coherence value and good quality of recorded seismic signal.

Table 6.1 show the master events selected. For clusters 6 and 7 I did not select any master events because of the high noise content recorded. For cluster 1, 2, 3 and 4 I identified more than one master events, whereas for cluster 5 and 8 only one.

Table 6.1 - list of selected master events plus the mainshock

Spatial Clusters	Master events	Latitude	Longitude	depth (km)
1	30/12/2018 05:02	63.95969	-21.33911	5.1
	30/12/2018 05:04	63.95969	-21.33911	5.5
	30/12/2018 07:49	63.95970	-21.33637	5.2
	30/12/2018 09:00	63.95834	-21.32817	7.0
	30/12/2018 12:43	63.95892	-21.33635	5.2
	01/01/2019 05:56	63.95969	-21.33911	5.4
	04/01/2019 00:49	63.96733	-21.33848	6.7
	23/01/2019 19:36	63.94889	-21.35145	5.9
2	22/12/2018 17:51	64.06689	-21.26794	3.5
	23/01/2019 18:58	64.05317	-21.26650	3.2
	26/01/2019 04:07	64.05819	-21.27650	3.2
	29/01/2019 02:29	64.06087	-21.28626	2.7
3	23/12/2018 18:52	64.04485	-21.40567	2.2
	14/01/2019 15:27	64.05285	-21.40578	2.4
	29/01/2019 19:16	64.05644	-21.40584	1.9
4	25/01/2019 05:56	64.00687	-21.37240	2.4
	25/01/2019 07:37	64.00267	-21.38052	2.2
5	30/01/2019 14:33	64.02287	-21.41353	2.2
8	29/01/2019 16:26	64.09663	-21.36539	3.2
	mainshock	latitude	longitude	depth (km)
	30/12/2018 02:56	63.97262	-21.32624	7.0

For each spatial cluster I selected the best quality master event, that is used to compute the relative magnitude of each cluster and the earthquake source inversion.

The relative magnitude of each cluster has been computed comparing the maximum horizontal amplitude of each events with the maximum amplitudes of selected master event, taken as reference (Grigoli et al., 2018):

$$M_i = M_{ref} + \log(A_i/A_{ref}) \tag{13}$$

where A_i is the observed maximum horizontal amplitude of an event, M_{ref} and A_{ref} are the magnitude and maximum horizontal amplitudes of reference event. For magnitude computation, I used from three to four stations per cluster such that epicentral distance is larger than the distance among events. I then used the average as the best estimation and the standard deviation for uncertainty.

For clusters 6 and 7 I selected two events with good quality of seismic signal recorded at least by four stations.

Results are summarized in figure 6.1 which shows a map with events of the eight clusters whose size is based on the computed relative magnitude (M_i). The computation shows that 85% of events has $M_i < 1$ and 30% of events has a $M_i < 0$. Computed relative magnitudes of each event in each cluster are provided in appendix B.

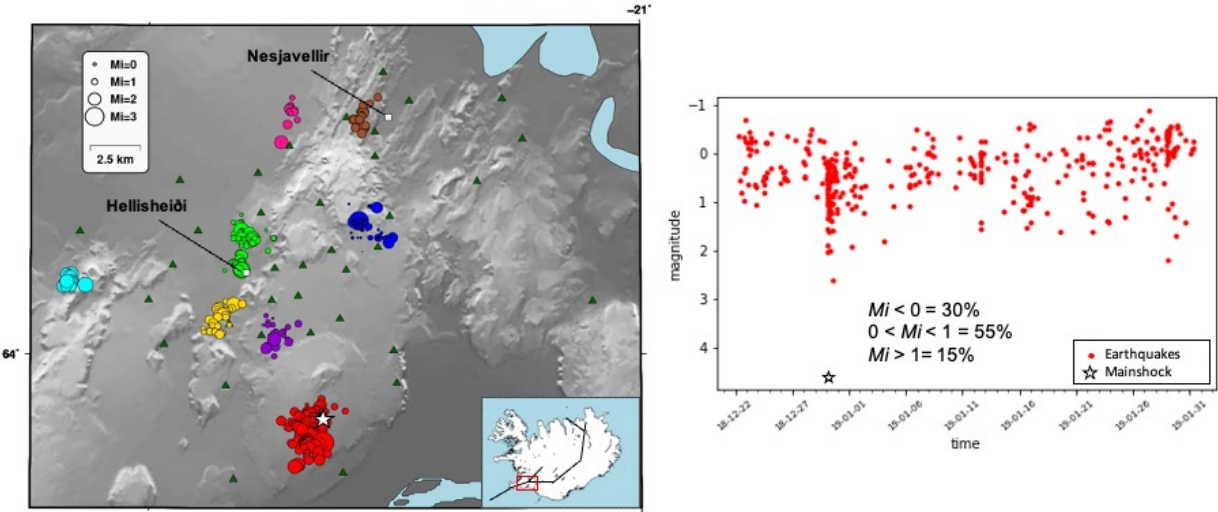


Figure 6.1 - Map of computed relative magnitude of eight clusters and time-magnitude plot. The dimensions of circles are sorted by the computed relative magnitude of each cluster

7. EARTHQUAKE SOURCE INVERSION

7.1 METHOD

Microseismic sources are typically modelled using a point source approximation. The more general and widely used is by means of a moment tensor (Gilbert, 1970), which is a general model which can be used to describe different types of seismic sources, including volumetric changes, shear and tensile failures.

The seismic moment tensor is a second-rank tensor, which describes a superposition of nine elementary force systems, with each component of the tensor giving the strength (moment) of one force system. The diagonal components M_{11} , M_{22} , and M_{33} correspond to linear dipoles that exert no torque, and the off-diagonal elements M_{12} , M_{13} , M_{21} , M_{23} , M_{31} , and M_{32} correspond to force couples. It is usually assumed that the moment tensor is symmetric ($M_{12}=M_{21}$, $M_{13}=M_{31}$, $M_{23}=M_{32}$), so that the force couples exert no net torque, in which case only six moment tensor components are independent.

The moment tensor can be decomposed into an isotropic term (ISO), which is associated with the volumetric change, and a deviatoric one. Jost and Hermann (1989) illustrated further possible decompositions of the deviatoric component; the most used is by means of a double-couple (DC) and a compensated linear vector dipole (CLVD) terms. The CLVD is a dipole that is corrected for the effect of volume change, describing seismic sources which have no volume change, net force, or net moment. The pure DC component is associated with the pure shear motion from two orthogonal vector pairs of equal magnitude but opposite sign. Significant deviations from the DC model have been found for nuclear explosions, mining collapses, and earthquakes in geothermal and volcanic environments (Foulger et al., 2004; Dreger, et al., 2008; Ford et al., 2009). In these cases, the seismic source displays a moment tensor with significant non-double-couple (non-DC) components, i.e. the sum of ISO and CLVD components, indicating different source processes such as tensile faulting, opening/closing-cracks, rupture of non-planar fault surfaces, cavity collapses, or source complexities. However, the non-DC component can also be an artifact of noisy data or due to instrument malfunction, or distortion due to the effect of the propagation path.

Thus, the seismic moment tensor representation is a formula to explain the theoretical relation between ground motions at the stations and seismic source.

Moment tensor inversion is an inverse problem requiring observed data, e.g. full seismograms or at least P and S phases, and the calculation or availability of accurate synthetic seismograms of the Earth (i.e. Green's functions, denoted by G).

Following Jost and Herrmann (1989), the displacement d on the Earth's surface at a station can be expressed, in case of a point source, as a linear combination of time-dependent moment tensor elements $M_{kj}(\xi, t)$ that are assumed to have the same dependence convolved (indicated by the star symbol) with the derivative $G_{sk,j}(x, \xi, t)$ of the Green's functions with regard to the spatial j -coordinate:

$$u_s(x, t) = M_{kj}(\xi, t) * G_{sk,j}(x, \xi, t)$$

where u_s are the ground displacement components (i.e. seismograms at n station) M is the moment tensor of the seismic point source at location ξ and at time t , and $G_{sk,j}$ represents Green's functions which describes all wave propagation effects including the elastostatic response of the Earth due to an impulsive and unidirectional force at source point ξ , and measured at point x .

Several methods have been developed for moment tensor inversion, fitting different observations, including first motion polarities (e.g., Nakamura 2000; Reasenber & Oppenheimer, 1985), waves amplitudes (e.g. Vavrycuk et al., 2008; Kwiatek et al., 2016; Syleny et al., 2009), P and S waves amplitude ratios (e.g. Miller et al., 1998; Hardebeck and Shearer, 2003; Jechumtálová and Šílený, 2005), full waveforms in time (Dreger and Woods, 2002; Sokos and Zahradník, 2008; Zahradník et al., 2008; Adamová et al., 2009) and frequency (Cesca et al., 2006; Zhao et al., 2014) domain or using combined time-frequency approaches (Vavrycuk and Kühn, 2012; Cesca et al., 2010, 2012; Zhao et al., 2014). The resolution of polarity- and amplitude-based methods are strongly affected by the geometry of the monitoring network and typically limited to the inversion of pure DC focal mechanisms. Furthermore, all these methods rely on previous epicentral and depth estimations and seismic rays tracing, which uncertainties can strongly bias the resulting focal mechanism.

Significant improvements have been obtained by moment tensor inversion methods based on full waveforms, which offer a common inversion framework, where both the

source location, centroid depth and moment tensor can be investigated. However, also full waveform-based inversion remains challenging for microseismic applications because they require the modelling of high-frequency waveforms and thus need a more detailed knowledge of the velocity structure.

Here, the inversion has been performed using GROND, a probabilistic earthquake source optimization framework based on bootstrap-based method (Heimann et al., 2018).

The core of optimization is the evaluation of misfit value (or objective function) between observed and synthetic data $|d_{obs} - d_{synth}|$.

GROND supports different input data (waveform and geodetic data) and their combination allows to use simultaneously different target, such as full seismic waveforms, amplitude spectra and body and surface waves.

Observed and synthetic data are processed in the same way before the misfit calculation. The misfit value is computed for each target based on the configurable L_p norm, and then it is normalized. Furthermore, different kind of weights can be applied as factors to the misfit. An example of weighting is the balancing of waveform targets with respect to the expected earthquake signal amplitude; the weight increases with source-receiver distance to balance amplitude inferred by geometrical spreading. This balancing weight tend to enhance small signals and suppress large signals in the misfit function.

The global misfit for a proposed source model results from contributions of multiple weighted target misfit. The source model that results in the smallest values of the objective function is the global minimum of the misfit function optimum model.

The optimization is performed by using the bootstrap method, based on iterative approach and a direct random search, where random model parameters are drawn from a defined model space. Those models are then calculated and compared with the target's observed data finding the absolute minimum of misfit function. The sketch in figure 7.1 show how this iterative and direct random source approach works; let us suppose we want to find the absolute minimum of the misfit function for the strike source parameter (Fig. 7.1 a), at the step 1 (i.e. the number of iteration) the algorithm random select different strike parameters finding several misfit values (fig. 7.1 b). At step 2, the algorithm searches more densely around the local minima and, at the same time, it continues the random search to explore all the model space (Fig. 7.1 c). This procedure continues according to the number of iterations, until the absolute minimum is found (Fig. 7.1 d).

To estimate model parameters uncertainties, a number of parallel bootstrapping chains are realized, where individual bootstrap weights and bootstrap noise are applied to each misfit target. Thus, each bootstrap chain has a different misfit and may converge to different areas within the model space. These differences represent the uncertainty of model with respect to data errors.

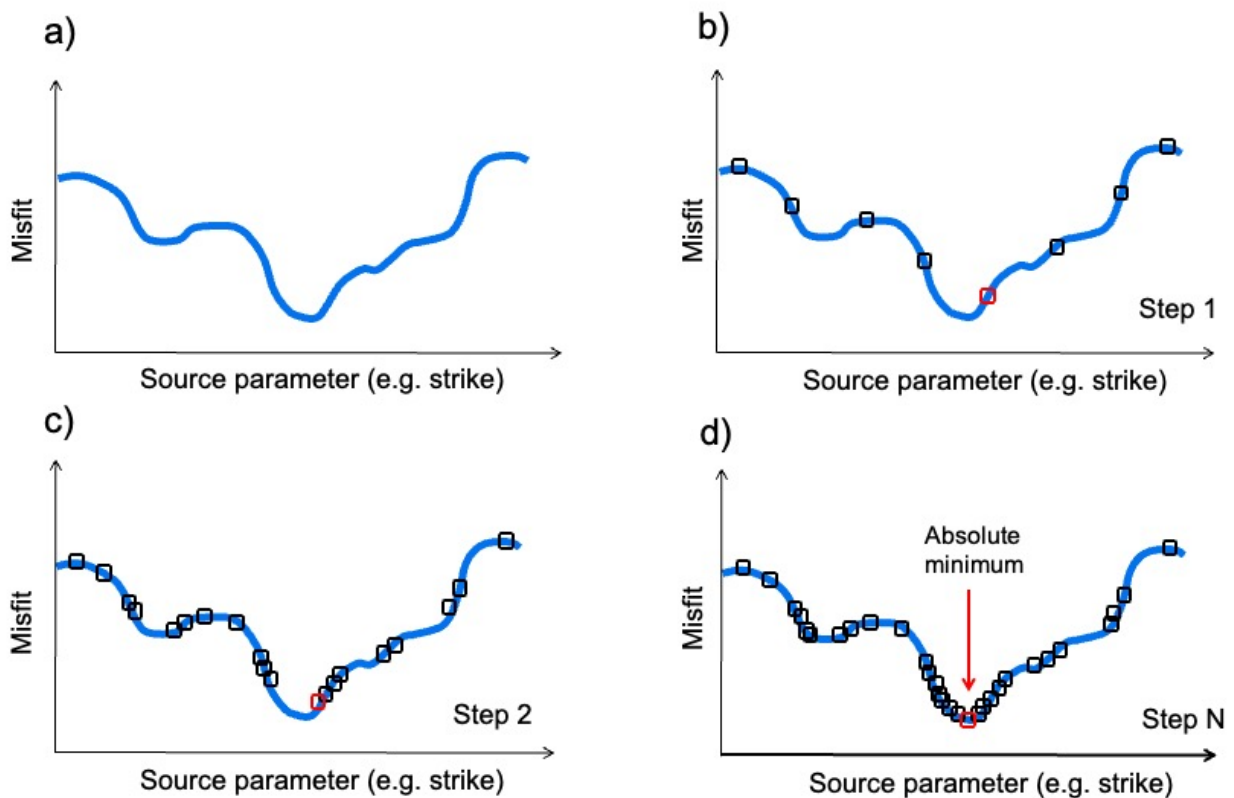


Figure 7.1 –Iterative and direct random search approach used in GROND optimization. a) misfit function of strike source parameter; b) random search around the model space; c) denser search around the local minima and random search simultaneously; d) the absolute minimum is found after N number of iterations

7.2 APPLICATION TO THE HENGILL DATASET

I performed the inversion for DC, deviatoric and full moment tensor source models separately. The L1 norm is used to measure the mismatch between observation and model. Synthetic seismograms are generated based on pre-calculated Green's functions (with QSEIS, Wang 1999) using the Tryggvason et al. (2002) velocity model. For local

distances of selected master events, I used 250 m grid spacing, 0 - 60 km epicentral distance and 0.250 - 15 km source depth, whereas for regional distances of the mainshock 1 km of grid spacing, 1 - 900 km epicentral distance, and 1 - 15 km source depth. Then synthetics data are tapered and filtered in the same way of observed data.

For the master events, I performed the inversion in time domain, using as targets both full waveform and body-waves recorded by local seismic network. To improve the time accuracy, synthetic and observed displacement traces are aligned based on manual P and S picks. To account for potential overlap of P and S time windows during the fitting procedure, I inverted full waveforms (time windows length between -0.2 s from P wave and + 0.9 s from S wave) for stations near to the source (with epicentral distance lower than 4.8 km) (Fig. 7.2 a) and separate P and S body waves (time windows respectively with 1 and 1.5 s length) for stations far away from the source (epicentral distances larger than 4.8 km) (Fig. 7.2 b). For full waveform inversion I used a frequency band between 1 and 3 Hz, whereas for body waves inversion between 1.5 and 2.5 Hz.

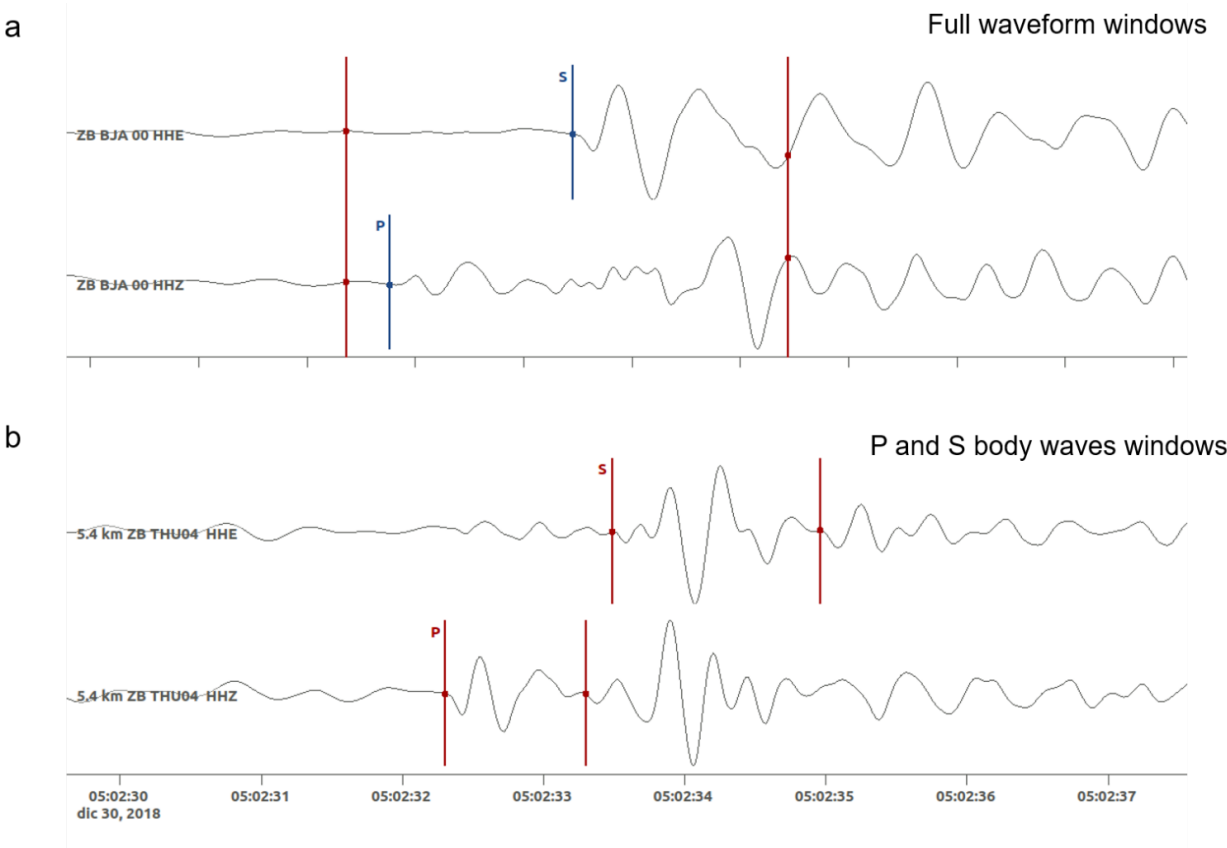


Figure 7.2 – Example of full waveform windows for epicentral distances lower than 4.8 km and b) P and S body waves windows for epicentral distances larger than 4.8 km of master events.

I performed the mainshock inversion both in time and frequency domain, using full waveforms recorded by regional seismic network with an epicentral distance range between 1-900 km. Time window length is between the P-wave arrival and + 2.0 s from S-wave arrival. The applied frequency filter is between 0.04 and 0.08 Hz. (Fig. 7.3).

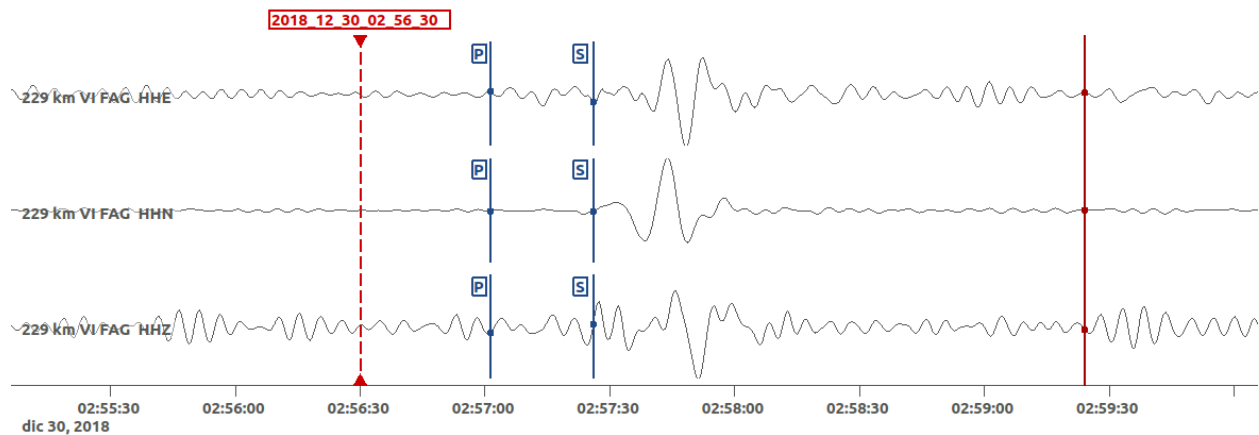


Figure 7.3 Example of full waveform windows for the mainshock

To choose the earthquake source model, I also evaluated the Bayesian (BIC) and Akaike (AIC) Information Criteria (Kass and Raftery 1995; Burnham and Anderson 2002) for the three source models (DC, deviatoric, full) of master events and mainshock. These criteria are defined as follows:

$$BIC = k \ln(n) + n \ln\left(\frac{R}{n}\right) \quad (14)$$

$$AIC = 2k + n \ln\left(\frac{R}{n}\right) \quad (15)$$

where k is the number of free parameters plus 1, n is the number of data points in recorded waveform and R is the misfit of solutions. According to the equations the lowest BIC and AIC values give an indication of the preferred source model. The BIC statistics penalizes a larger number of free parameters more heavily than the AIC, because k is multiplied by the natural log of n . Basically, the BIC selects a simpler model (i.e. with less parameters) than AIC.

7.3 RESULTS

For the misfit calculation, observed and synthetic data are processed in the same way for all target used in master events and mainshock inversions. In Appendix C an example of the best fitting model between observed and synthetic data for a master event (Fig. C.1) and for the mainshock (Fig. C.2) are shown. In addition, examples of the optimization process results of strike and rake parameters and the sorted misfit of single bootstrap chains for a master event and the mainshock are reported in figures C.3 and C.4 (see Appendix C).

Figure 7.4 shows all source model solutions (DC, deviatoric and full) of selected masters of each clusters (divided by colours) and mainshock (in black).

Masters	Latitude	Longitude	depth (km)	DC	dev	full
30/12/2018 05:02	63.95969	-21.33911	5.1			
30/12/2018 05:04	63.95969	-21.33911	5.5			
30/12/2018 07:49	63.95970	-21.33637	5.2			
30/12/2018 09:00	63.95834	-21.32817	7.0			
30/12/2018 12:43	63.95892	-21.33635	5.2			
01/01/2019 05:56	63.95969	-21.33911	5.4			
04/01/2019 00:49	63.96733	-21.33848	6.7			
23/01/2019 19:36	63.94889	-21.35145	5.9			
22/12/2018 17:51	64.06689	-21.26794	3.5			
23/01/2019 18:58	64.05317	-21.26650	3.2			
26/01/2019 04:07	64.05819	-21.27650	3.2			
29/01/2019 02:29	64.06087	-21.28626	2.7			
23/12/2018 18:52	64.04485	-21.40567	2.2			
14/01/2019 15:27	64.05285	-21.40578	2.4			
29/01/2019 19:16	64.05644	-21.40584	1.9			
25/01/2019 05:56	64.00687	-21.37240	2.4			
25/01/2019 07:37	64.00267	-21.38052	2.2			
30/01/2019 14:33	64.02287	-21.41353	2.2			
29/01/2019 16:26	64.09663	-21.36539	3.2			
mainshock	latitude	longitude	depth (km)			
30/12/2018 02:56	63.97262	-21.32624	7.0			

Figure 7.4 - Results of earthquake source inversion. The three source model solutions (DC, deviatoric and full) are reported for each selected master events (divided in colours according to belonging cluster) and for the mainshock (in black).

No focal mechanisms are available for clusters 6 and 7 because of high noise content of recorded seismograms.

Focal mechanism solutions for the mainshock are in agreement with local solutions of cluster 1, which include many aftershocks of the seismic sequence.

DC solutions show from normal to strike-slip fault solutions, with most of nodal planes striking NNE and E-dipping (Fig. 7.5).

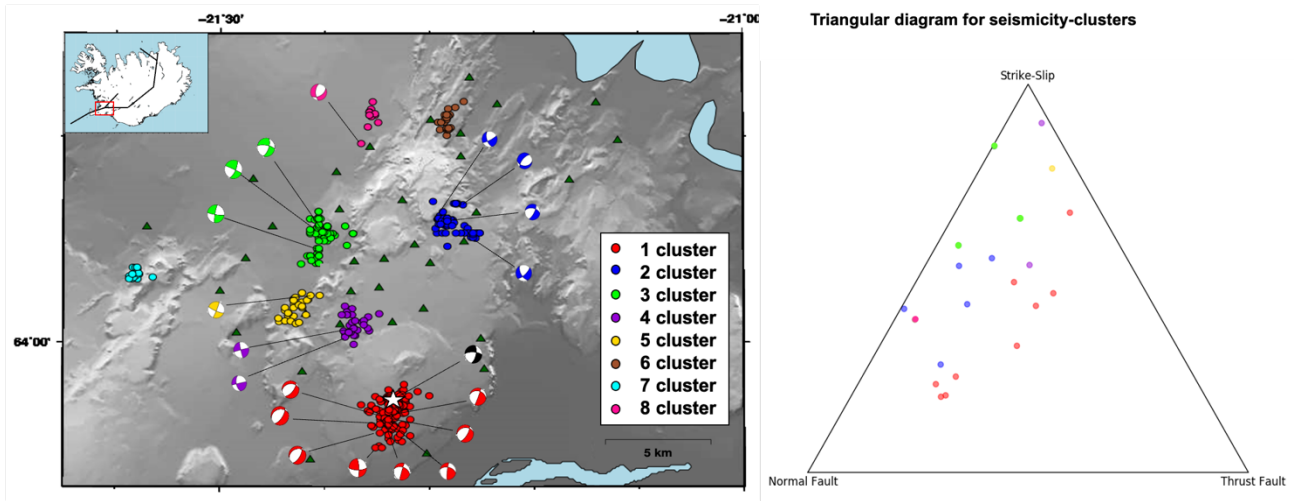


Figure 7.5 - DC focal mechanism solution and triangular diagram for faults classification of master events in each cluster

Most of deviatoric solutions has a positive CLVD component, whereas full solutions are quite different from cluster to cluster. For instance, cluster 4 show a large isotropic component in full solution, whereas cluster 1 has a larger deviatoric component.

Orientation of pressure (P) and tension (T) axes for the three source solutions is consistent in each cluster (Figure 7.6): P axes range from horizontal NE or SW through vertical, and T axes show predominately horizontal NW-SE orientation. Compressional and dilatational zones are in agreement with the tectonic trend of area.

Pressure (P), Tension (T), Null (B) axis of clusters and mainshock

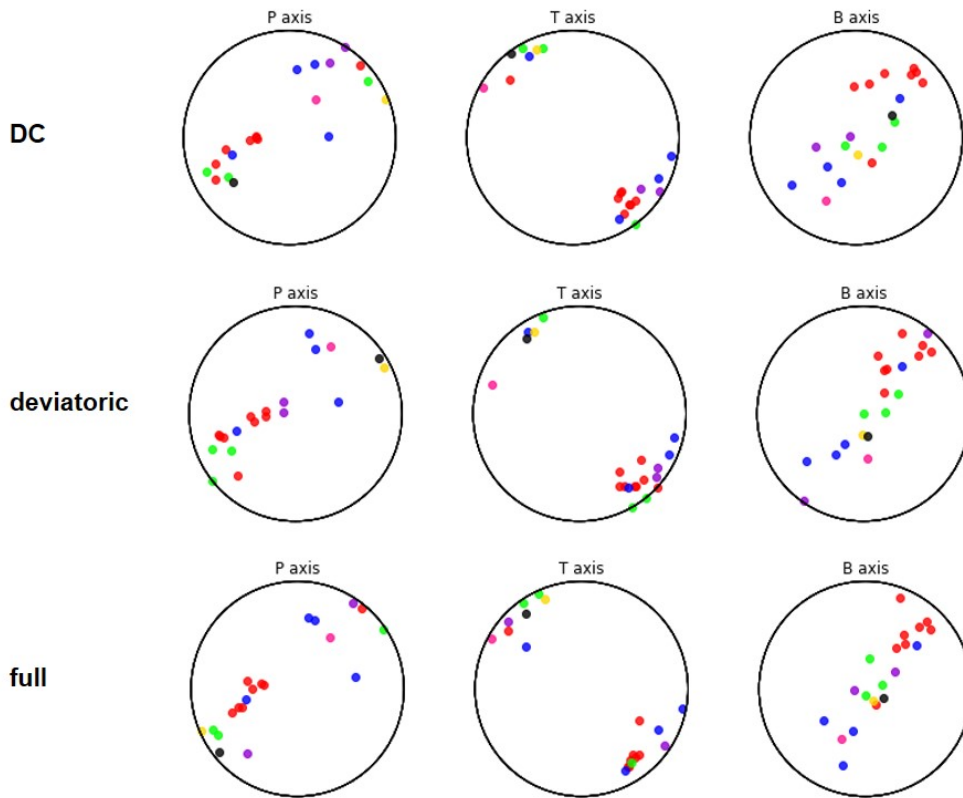


Figure 7.6 - Orientation of pressure (P), tension (T) and null (B) axes of each cluster for DC, deviatoric and full source model solutions

Figure 7.7 indicates misfit values of selected master events and the mainshock for the three source models, showing how they are similar to each other, especially the DC and deviatoric misfit values. The mainshock solutions present the higher misfit values, most probably due to the low number of station and their poor coverage, not homogeneously distributed

Table 7.1 show the mean BIC and AIC values of the three source models for each cluster and for the mainshock, with the lowest BIC values marked in red. AIC and BIC values are similar and the preferred source models for each cluster are the same for both. Most of cluster and the mainshock have DC and full preferred source models, however all values of the three models are very similar without any remarkable difference

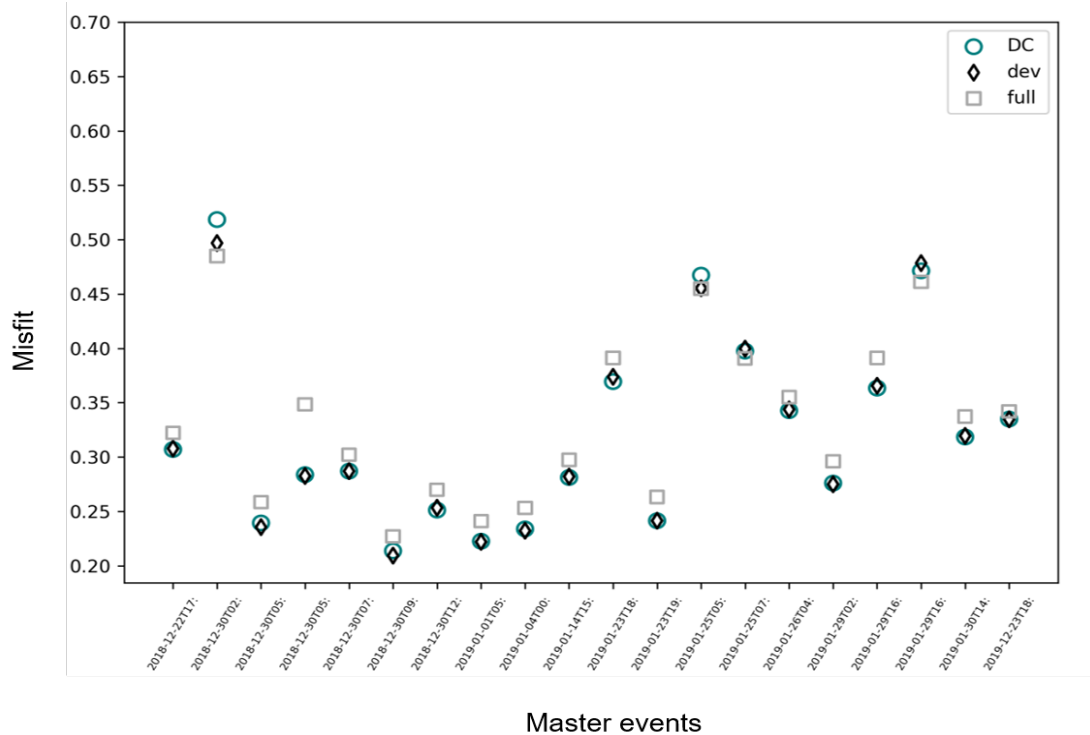


Figure 7.7 - Misfit values of earthquake source inversion for each master events and for the three source models.

Table 7.1 - Mean BIC and AIC values of the three source models for spatial clusters and the mainshock.

SPATIAL CLUSTER	DC-BIC	DEV-BIC	FULL-BIC	DC-AIC	DEV-AIC	FULL-AIC
1	-1.1859E+06	-1.1863E+06	-1.1780E+06	-1.1859E+06	-1.1864E+06	-1.1781E+06
2	-1.2713E+06	-1.2710E+06	-1.2655E+06	-1.2713E+06	-1.2711E+06	-1.2656E+06
3	-1.7236E+06	-1.7232E+06	-1.7163E+06	-1.7236E+06	-1.7232E+06	-1.7164E+06
4	-1.3020E+06	-1.3032E+06	-1.3043E+06	-1.3020E+06	-1.3032E+06	-1.3044E+06
5	-1.9172E+06	-1.9167E+06	-1.9088E+06	-1.9172E+06	-1.9168E+06	-1.9088E+06
8	-1.1075E+06	-1.1061E+06	-1.1094E+06	-1.0755E+05	-1.1062E+06	-1.1095E+06
MAINSHOCK	-2.5386E+07	-2.5458E+07	-2.5499E+07	-2.5386E+07	-2.5458E+07	-2.5499E+07

8. DISCUSSION

I investigated the seismicity at Hengill geothermal area recorded between 22 December 2018 and 31 January 2019, including a seismic sequence at the end of December 2018 with Mw 4.7 mainshock occurred on 30 December 2018.

The dataset is mainly composed by low magnitude events, characterized by high frequency content and low SNR of recorded waveforms. Thus, their analysis and characterization are challenging. I applied automated methods for earthquakes location, clustering analysis and source mechanisms determination that explore the full waveform, and that have proven to be efficient tools for microseismic and noisy events investigations.

Hypocentral distribution of seismic events shows that: 1) shallower events, with depth less than 4 km, occurred in the proximity of the geothermal fields and seem to be clustered in three small clusters; 2) most of deeper events appear as a bigger separate cluster located outside the geothermal area, on the neighbouring SISZ (Fig. 4.7). The obtained results are in agreement with those obtained by manual location and highlight how uncertainties of solutions also depend on the position of events with respect to the seismic network (Fig. 4.8).

Spatial clustering identifies eight clusters and shows that most of shallower events belong to clusters 3, 4 and 5, located in centre of geothermal area, whereas deeper events seem to occur at the edges of geothermal site (Fig. 5.2). In particular, the Mw 4.7 seismic sequence belongs to the biggest and deepest cluster (Fig. 5.2), quite separate from the others and located in south of study area with an E-dipping depth-trend.

Most of waveform clustering results show one waveform family (except for clusters 3, 6 and 8), suggesting the activation of single planar structures, or subparallel faults (see table 5.1). Some selected stations of cluster 3 detect two waveform-families on only one component (GAN02 and GRH43 stations on vertical component, INNST station on horizontal component); considering focal mechanism solutions I attribute the detection of two waveform families to specific event-station geometries, with the stations laying close to nodal planes. For instance, P-first motion polarities recorded at stations GAN02 and GRH43 are both positive or negative, but these stations are located close to one nodal plane, so that different polarities can be explained for the same mechanism just due to minor location changes (Fig. 8.1).

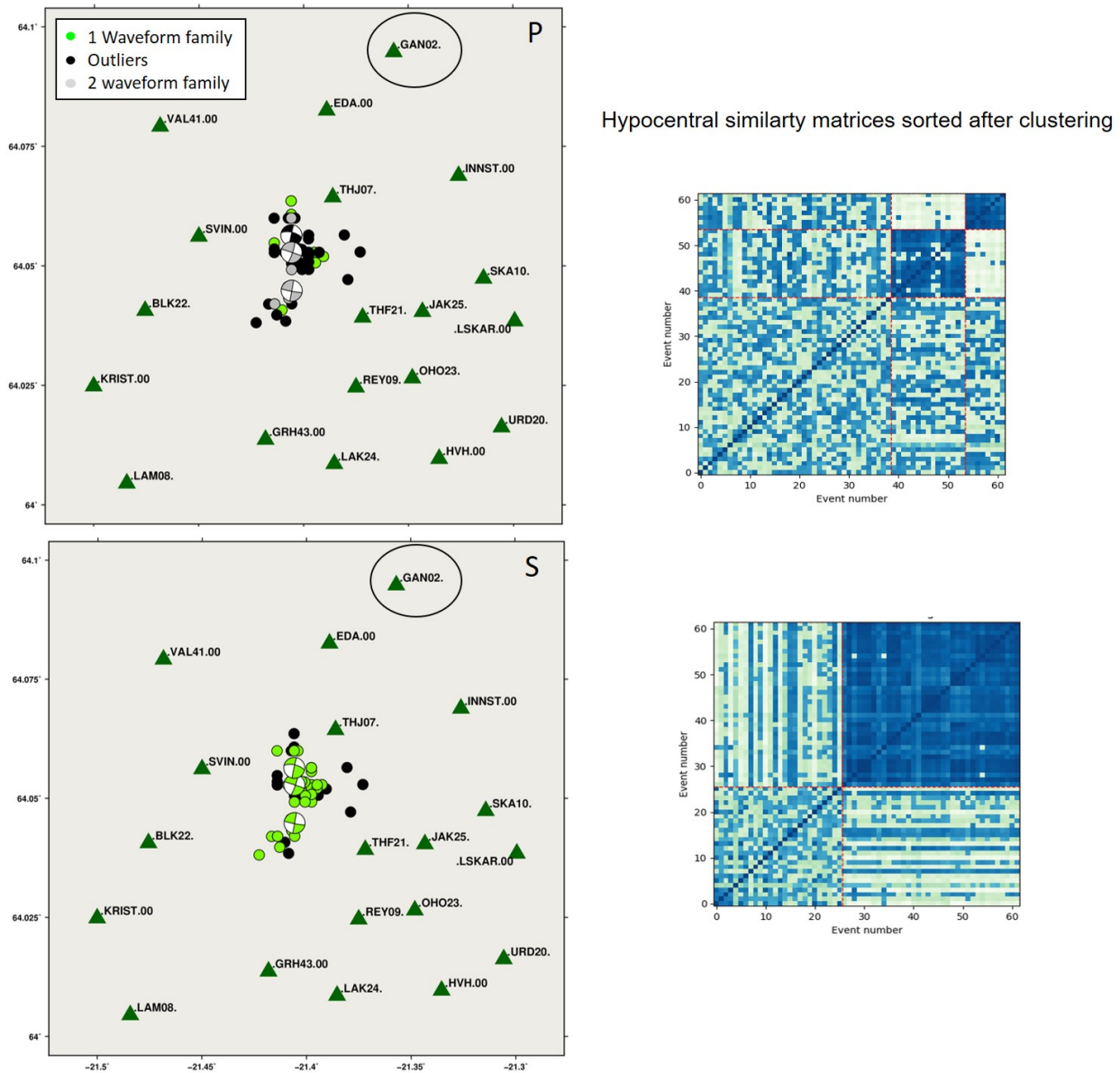


Figure 8.1 - Waveform clustering results and DC focal mechanism of cluster 3. Locations of station close to nodal planes might explain different P first motion polarities and the 2 waveform families observed.

Based on BIC and AIC values (table 7.1), most of cluster and the mainshock have DC and full preferred source model, however all values for the three models are very similar, without any remarkable difference.

Although source inversions of the mainshock and cluster 1 are computed with two different seismic networks, their solutions for the three source models are in agreement with each other.

DC focal mechanisms (Fig. 7.5) and P and T axis orientation (Fig. 7.6) show normal and strike slip fault solutions with a plane striking NNE and ESE-dipping, in agreement with the dominant tectonic trend of area (Foulger and Toomey 1989; Steigerwald et al., 2020; Bergerat and Angelier, 2000). Furthermore, the tectonic orientation is consistent with the depth-trend of cluster 1 (see vertical section in Fig. 5.2), showing an E-dipping oriented plane.

The decomposition of full moment tensor solutions (Fig. 8.2) found that shallower master events show a quite large non-DC components (Fig. 8.3 a), especially the ISO component (Fig. 8.3 d) for cluster 4 (in violet) and 8 (in pink). These solutions are typical of induced earthquakes or of natural ones not caused by pure shear faulting.

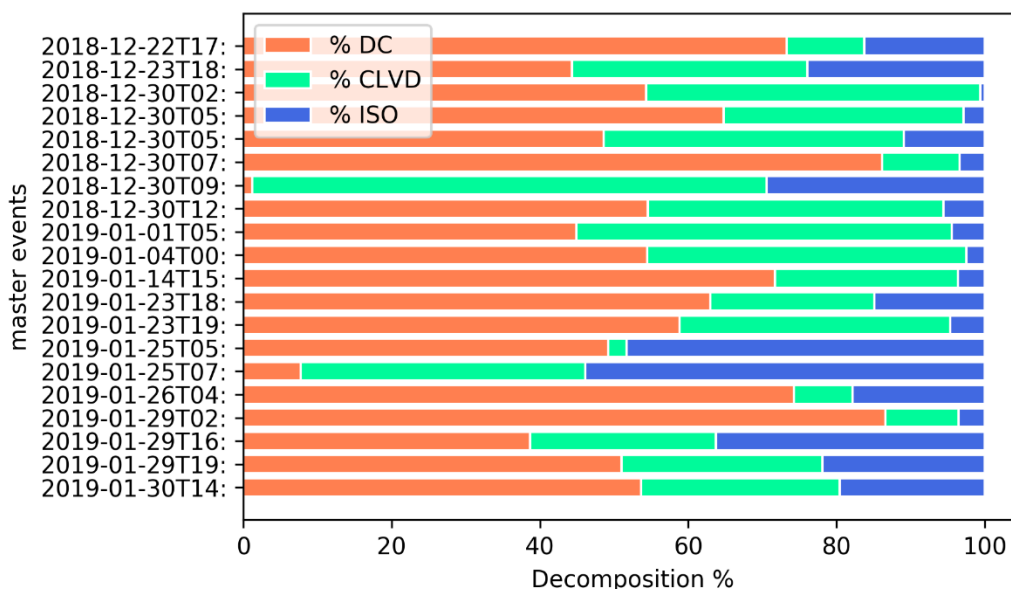


Figure 8.2 - Decomposition of full moment tensor solutions in DC (orange), CLVD (green) and ISO (blue) components of selected master events

On the contrary, deeper master events are close to deviatoric solutions, i.e. the CLVD + DC components (Fig. 8.3 b). In particular, focal mechanisms of cluster 1 differ from the others due to the high percentage of positive CLVD in full solutions (Fig. 8.3 e); this source model is agreement with a combination of shear and tensile faulting.

Even some focal mechanism from previous studies (Miller et al., 1998, foulger 1988 a,b; Sigmundsson et al., 1997) related to small earthquakes activity show some solutions with normal and strike-slip faults related to plate movements in the area, and other ones with a significative non double couple component. The authors suggested that such

earthquakes are either due to tensile cracks formation, resulting either from thermal contraction and cracking in the heat source, or to magma injection under the volcanic system, or even due to a combination of shear and tensile faulting.

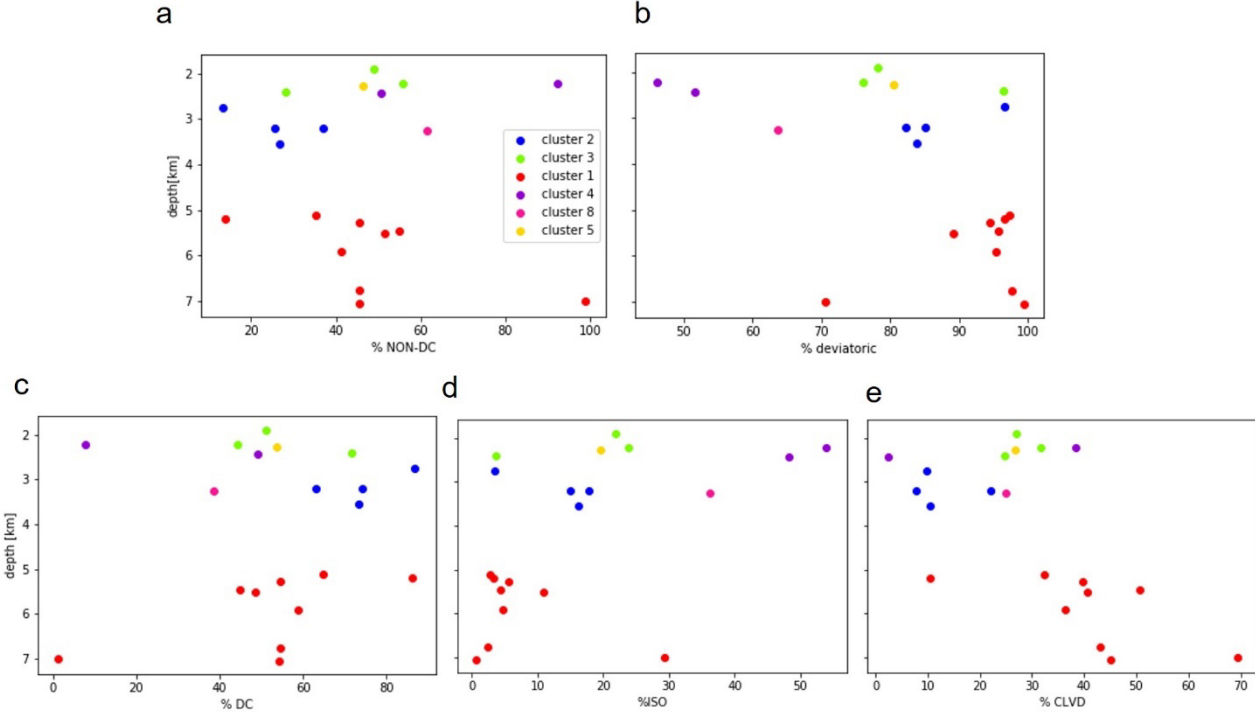


Figure 8.3 - Percentage of moment tensor components of each master events full solution: a) non-DC, b) deviatoric, c) DC, d) ISO, e) CLVD components.

9. DISCRIMINATING BETWEEN NATURAL AND INDUCED SEISMICITY AT HENGILL AREA

As mentioned in the Introduction section, to discriminate between natural and induced seismicity several approaches have been proposed but there is not yet a unique and standardized approach. Current discrimination methods can be divided into two main categories: qualitative and quantitative approaches. The first ones are based on series of binary questions related to observed seismicity and industrial activities, using direct seismological information, such as the spatio-temporal correlation between anthropogenic activities and seismic events. The other group of approaches requires specific physics and probabilistic analyses, thus requiring different type of data such as hydraulic, geologic and geomechanical data.

Quantitative approaches can provide more robust answers with respect to qualitative approaches, whose results can lead to ambiguous interpretation. On the other hand, significant results in quantitative methodologies require high-quality data of different type (such as hydraulic data, geological information and geomechanical models). However, these datasets are often missing and, as a consequence, quantitative discrimination methods can be used only rarely. In addition, using these approaches with unreliable data may introduce biases and mislead the results.

In this work, to discriminate between natural and induced events at Hengill geothermal area, in addition to parameters-based methods for seismic source characterization (see section 7) I also performed the test YES or NO proposed by Davis and Frohlich (1993) based on available data. This qualitative method allows to assess whether events can be due to the fluid injection or not through 7 criteria (questions). These questions address 4 factors: 1) the historical seismicity of the study region, 2) the geographical and geological relationship between injection sites and seismic activity 3) the presence or absence of temporal correlation between injection and seismic activity, 4) the expected effect of fluid injection on the stress regime at the injection sites.

A “YES” answer supports induced origin caused by injection, a “NO” answer suggests that injection is not the cause. In many cases, where answers are uncertain because of incomplete or conflicting information, they denote these less certain answers with question marks “YES ?” or “NO ?”.

If “YES” answers are five or more, then they conclude that there is a strong evidence of relation between injection and seismic, if the “YES” answers are three or fewer, they suggest a cause different from the injection.

I performed the Davis and Frohlich test (1993) for each spatial cluster and considering separately Hellisheiði and Nesjavellir geothermal wells. Injection data refer to 11 wells located at Húsmúli and Gráuhnúkar zones, which are two reinjection sites of Hellisheiði field. These data include information about pressure at well head (bar) (table 9.1) and flow rate Q (l/s) (table 9.2) from December 2018 to January 2019 at Gráuhnúkar site and for January 2019 at Húsmúli site.

Table 9.1 - Pressure (bar) at well head (bar) at Húsmúli and Gráuhnúkar site

Húsmúli wells	min P (bar)	date	max P (bar)	date	mean P (bar)
HN-16	4.7282817	14/01/2019	6.5028986	29/01/2019	5.568168
HN-09	-0.6933691	15/01/2019	8.0589678	24/01/2019	7.296298
HN-14	-0.4155142	14/01/2019	8.4596066	24/01/2019	7.751557
HN-12	-0.6877895	29/01/2019	7.1815803	29/01/2019	6.513040
HN-17	-0.6409265	15/01/2019	7.5616875	24/01/2019	6.824961
Gráuhnúkar wells					
HN-05	7.1957826	14/01/2019	8.5767058	24/01/2019	7.952339
HN-08	7.0557981	14/01/2019	8.434551	24/01/2019	7.809758
HN-10	6.8764916	14/01/2019	8.2203495	24/01/2019	7.606917
HN-06	7.0308564	14/01/2019	8.3948531	24/01/2019	7.774539
HN-07	7.1892146	14/01/2019	8.5680543	24/01/2019	7.944880
HN-03	7.0373378	14/01/2019	8.4110851	24/01/2019	7.788840

Table 9.2 - Flow rate (l/s) at well head at Húsmúli and Gráuhnúkar site

Húsmúli wells	min Q (l/s)	date	max Q (l/s)	date	mean Q (l/s)
HN-14	0.5184221	14/01/2019	35.3178038	15/01/2019	18.351085
HN-17	0.9799383	15/01/2019	58.0256548	15/01/2019	28.705836
HN-12	-9.7550153	29/01/2019	74.7791271	30/01/2019	-4.881755
HN-09	0.05787	15/01/2019	79.1608781	15/01/2019	53.922276
HN-16	48.0497679	29/01/2019	80.2430549	14/01/2019	69.091119
Gráuhnúkar wells					
HN-10	40.3919406	29/01/2019	70.739787	14/01/2019	64.658708
HN-07	47.3318568	29/01/2019	81.5545012	01/01/2019	74.275994
HN-05	24.6709165	29/01/2019	36.0310446	01/01/2019	33.545333
HN-08	52.1209822	29/01/2019	75.3504835	01/01/2019	70.892306
HN-03	0.289344	29/01/2019	1.8228672	15/01/2019	0.799363
HN-06	31.0461295	29/01/2019	52.5685012	01/01/2019	47.571758

Table D.1 in Appendix D shows the results of the Davis and Frohlich test (1993) for each spatial cluster, specifying the related geothermal field. The answers are explained below.

Question 1 - Are these events the first known earthquakes of this character in the region?

Previous studies (Bjornsson, 2004; Gunnarson et al., 2013 a,b; Ágústsson et al., 2015; Stefánsson and Halldórsson, 1988; Einarsson, 1991; Árnadóttir et al., 2001; Hreinsdóttir et al., 2009) already highlighted the occurrence of small ($M < 2$) and moderate ($M \geq 4$) earthquakes in the same area of the eight clusters, that seem related to both natural and injection/reinjection operations for the geothermal exploitation.

Question2 – Spatial correlation

In table 9.3 the mean epicentral distance (in km) between the bottom of wells and the mean clusters epicentral location, for both geothermal sites, are indicated. Figure 9.1 shows the location and depth traces of Hellisheiði and Nesjavellir injection wells (delivered by Reykjavik Energy) together with earthquakes and full focal mechanism solutions of master events.

Table 9.3 - Mean epicentral distances (km) between clusters and the wells bottom at Hellishedi and Nesjvellir geothermal sites.

spatial clusters	mean distance (km) between cluster and bottom-wells at Hellsiheidi	mean distance (km) between cluster and bottom-wells at Nesjavellir
1	8,455	15,305
2	5,648	4,654
3	2,939	8,308
4	3,750	11,199
5	3,751	11,918
6	9,226	1,661
7	10,091	16,721
8	8,317	4,401

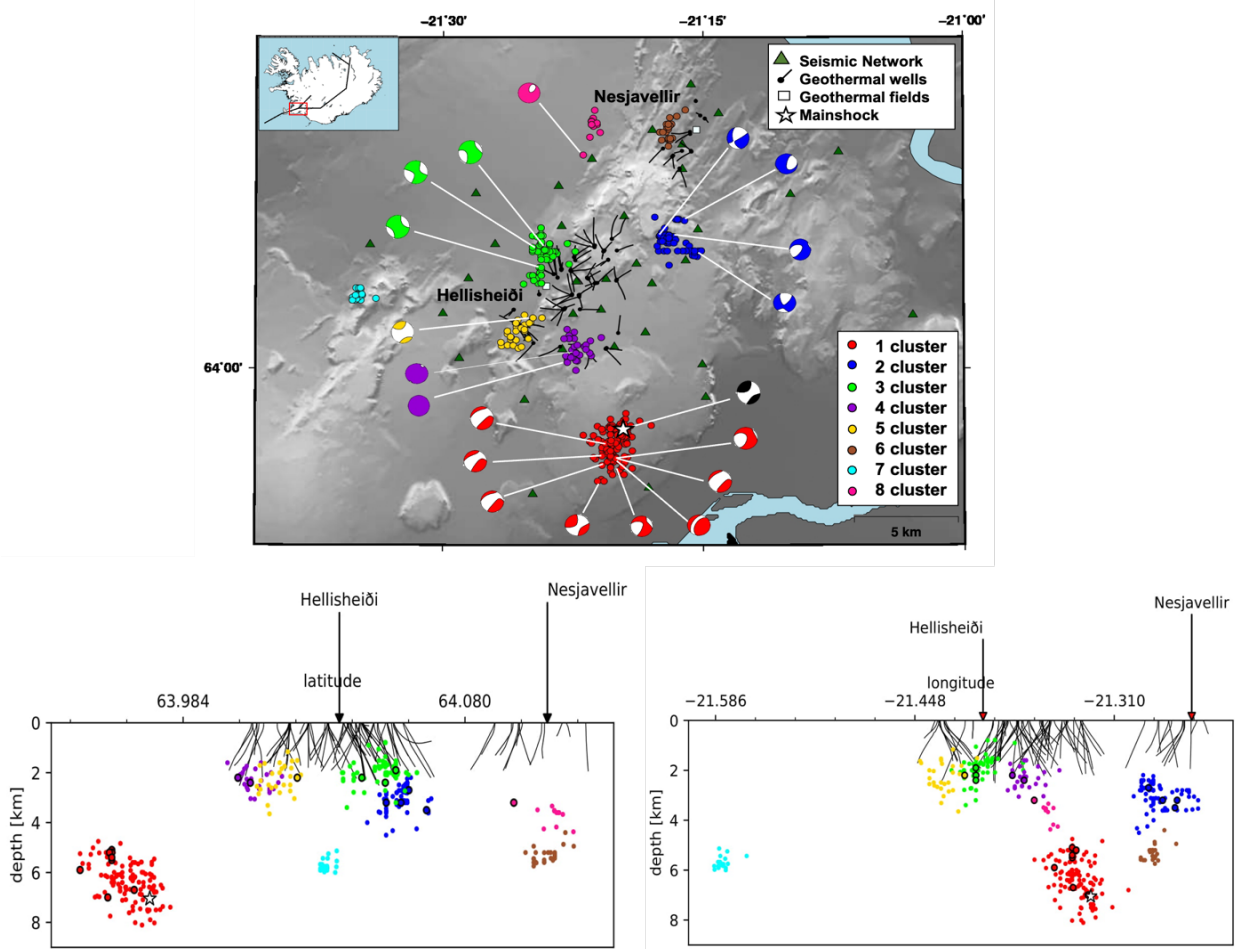


Figure 9.1 - Map and two orthogonal NS and EW vertical sections of clusters with the full moment tensor solutions of master events (circled in black in vertical sections) and the location of Hellisheiði and Nesjavellir injection wells (black lines).

Cluster 1, 2, 6, 7 and 8 have a mean distance larger than 5.0 km with respect of Hellisheiði wells, whereas cluster 3, 4 and 5 are within 5 km from Hellisheiði wells, in the vicinity of some injection wells at depth < 3.0 km (see vertical section in Fig. 9.1). In particular, cluster 3 occurred at Húsmúli site, close to wells listed in table 9.1, whereas some events of cluster 4 and 5, are located near Gráuhnúkar wells (Fig. 9.2).

Considering Nesjavellir field, epicentral location of cluster 6 is within 2 km from wells bottom, however its depth is larger than 4.5 km, deeper compared to the wells bottom. Even cluster 2 and 8 are located within 5 km from wells bottom, with depth > 2 km (Fig. 9.1). However, at Nesjavellir field, until December 2018, the injection was shallow with injection wells less than 500 m deep for the ground water system.

Some studies mapped tectonic structures and fissure swarms in the area (Saemundsson, 1979; Eirnasson 2008; Khodayar and Björnsson 2014; Steigerwald et al., 2020). The

dominant tectonic trend of the area is extensional, with the distribution of major faults and eruptive fissures oriented NNE, parallel to the accretionary zones, whereas South of 64°N, in the SISZ, the area is characterized by transform faulting with the main tectonic structures striking N-S. There is no direct evidence of a possible channel flow rate, however the distribution of some faults is close to injection wells.

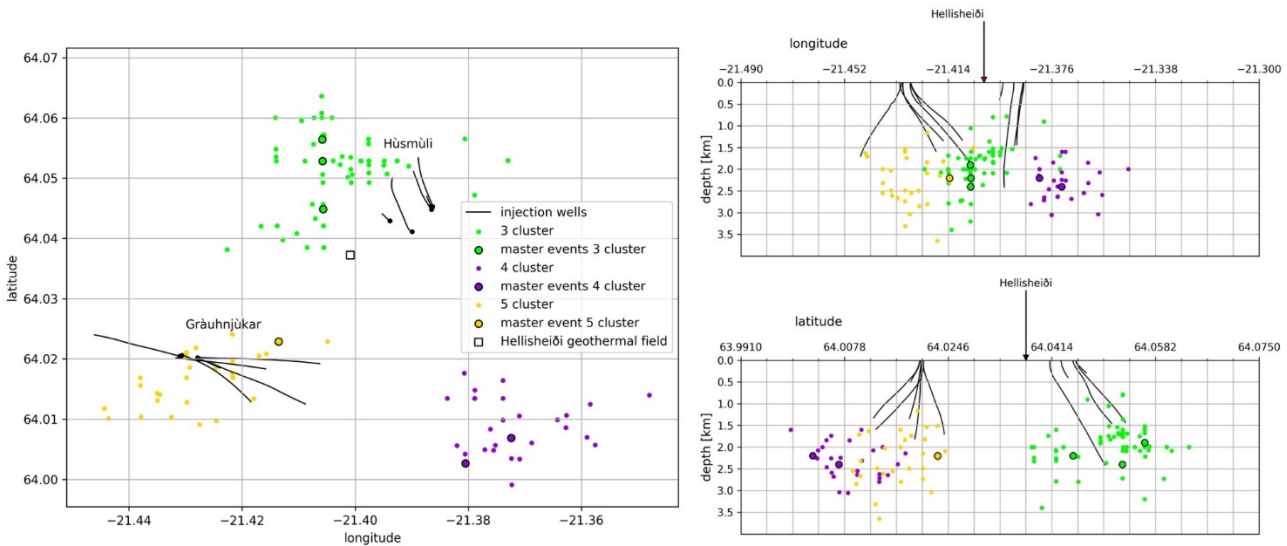


Figure 9.2 - Map and two orthogonal NS and EW vertical sections view of injection wells listed in table 9.1 and 9.2 at Hús múli and Gráuhnúkar site and clusters 3, 4 and 5. Master events are marked with black edge circle.

Question 3 – Temporal correlation

For Gráuhnúkar site, injection data are provided for all the period considered in this work, from 22 December 2018 to 31 January 2019, with the exception of a small gap window at the beginning of January. During the stimulation period, some events of cluster 4 and 5 occurred (Fig. 9.3). The number of events belonging to cluster 4 tends to increase after 21 and 24 January (Fig. 9.3 a, c), at the highest values of pressure (see table 9.1). The two focal mechanism available for this cluster occurred on 25 January and have a high percentage of ISO component. The lower pressure values are recorded on 14 January, but no events occurred at the site. However, few earthquakes occurred before 14 January, that seems not connected to the stimulation.

Most of events of cluster 5 occurred at the end of December and on 6 January (Fig 9.3 d), a few days after the maximum values of flow rate (see table 9.2).

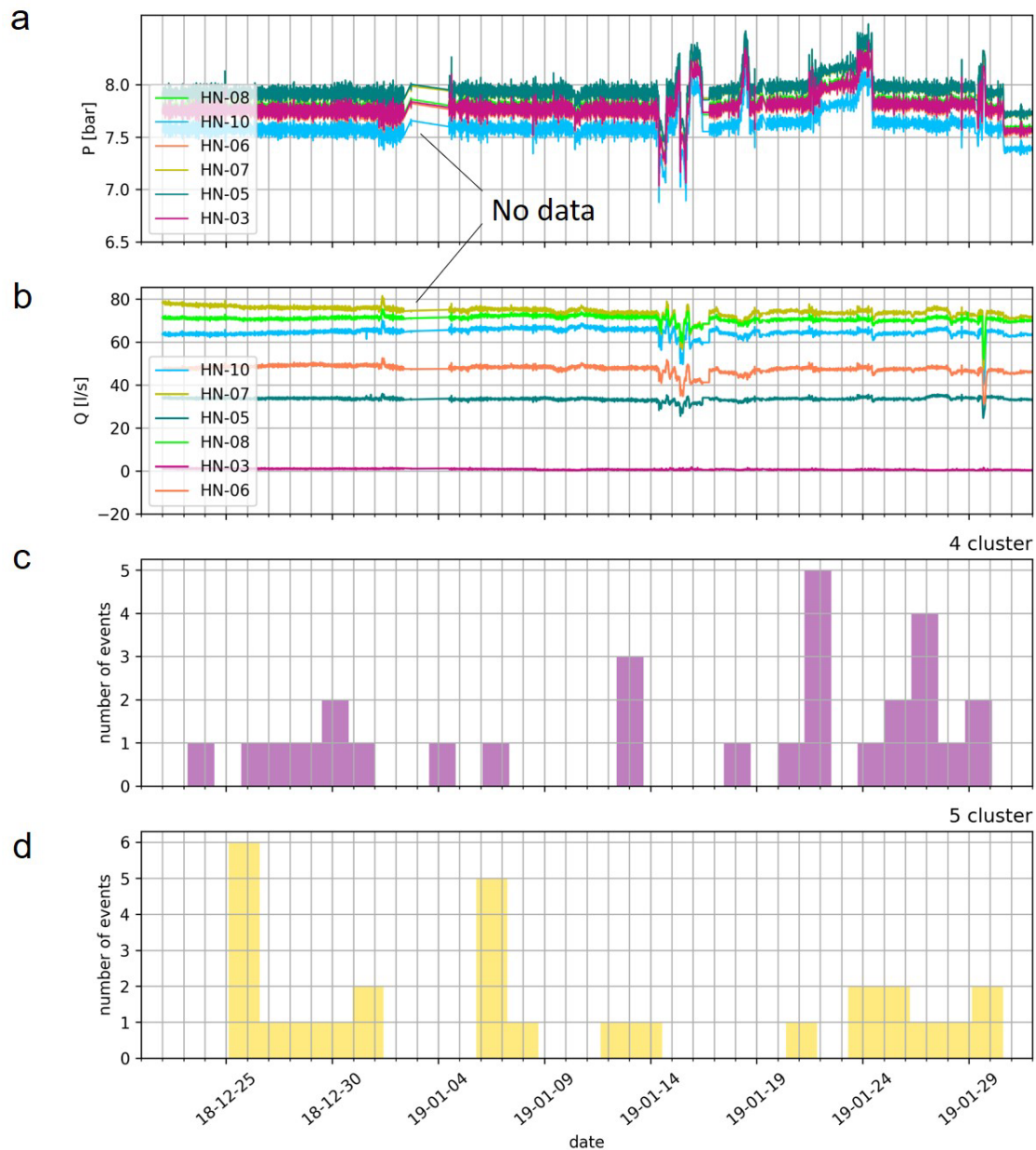


Figure 9.3 - Pressure (bar) (a) and flow rate Q (l/s) (b) applied at Gráuhnúkar wells head from 22 December 2018 to 31 January 2019. Number of events of clusters 4 (c) and 5 (d).

For Húsmúli site, injection data are provided for January 2019. Although Húsmúli site is not known as a seismically active area, during the stimulation some seismic events belonging to cluster 3 occurred (Fig. 9.4). In particular, the number of events tend to increase after 24 January until 29, when the applied pressure is higher (Fig. 9.4 a, c). A small seismic sequence occurred between 11 and 12 January, before the pressure drop (see table 9.1 and Fig. 9.4 c), and it seems not associated to the production wells.

The higher picks of flow rate occur immediately after the minimum values, between 14 and 15 January (table 9.2), but few events occurred during these days (Fig. 9.4 b, c). Temporal and spatial correlation between injection and seismicity was already found by Yusef (2020) for the period January 2018 and 2019 at Húsmúli and Gráuhnúkar sites, where seismicity took place after changes in the pressure or the injection rate.

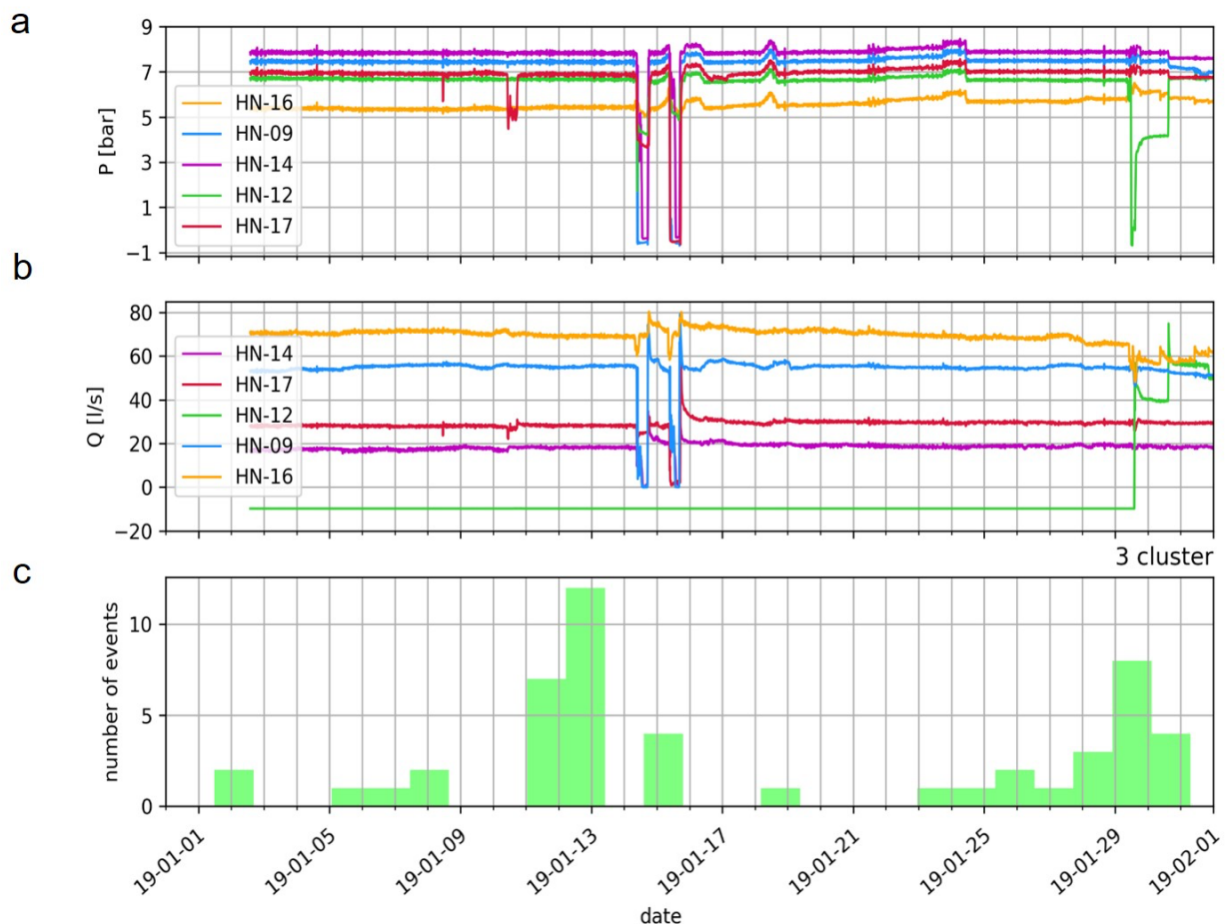


Figure 9.4 - Pressure (bar) (a) and flow rate Q (l/s) (b) applied at Húsmúli wells head from 1 January 2019 to 31 January 2019. Number of events of clusters 3 (c).

Question 4 – Injection practices

For both Húsmúli and Gráuhnúkar injection sites, the higher-pressure values at wells head are larger than 8 bar.

There are already a few reported cases of induced seismicity before 2018, such as the two M 4.0 induced events in 2011 (Bessason et al., 2012; Ratouis et al., 2019); the 2011

earthquakes occurred during rapid changes in the injection rates, but their triggering mechanism is still disputed. The induced earthquake found during 2011 - 2012 and the two mainshock occurred on normal and strike-slip faults with NNE-SSW orientation, in agreement with DC focal mechanism results.

At Húsmúli site between 2011 and 2012 a small induced seismicity was observed during drilling and testing of the wells, with the head pressure of 8 bar and 28 bar in the well, considering that the natural water level in the area is 200 m, which results in additional hydrostatic pressure of 20 bar in the well, when it is full of water (Gunnarson et al., 2013 a; Sveinbjornsson and Thorhallsson 2013). Even our pressure values are in the same range of the previous ones for the same site and the seismic events have magnitude less than 1.5. However, the applied pressure in the wells was also not high enough to cause hydrofracturing. An explanation for this seismic activity is that the reinjection triggered earthquakes, which released stresses that had already built up in the area (Gunnarson et al., 2013 a).

Although the pressure levels are similar, the flow rate for the period 2011-2012 was higher (> 100 l/s) (Bessason et al., 2012, Juncu et al., 2020) with respect to 2018-2019 level, whose mean value is about 30 l/s.

Some earthquakes occurred in 2003-2004 were also correlated to injection activity, where the fluid pressure changes inside the local reservoir fractures network have been observed (Bjornsson 2004).

The Davis and Frohlich (1993) test results show that, cluster 3, 4 and 5 are marked with “YES” or “YES?”, with the exception of the first answer, suggesting a clear relationship between seismic events and injection activities at Hellisheiði injection site. Other clusters are marked with “NO” for the same site suggesting a natural origin. Clusters 2, 6 and 8 have a mean epicentral distance from Nesjavellir wells bottom less than 5 km, however no deep injections were performed at the site.

9.1 SUMMARY

In order to discriminate between natural and induced seismicity at Hengill geothermal area, I computed earthquake location, clustering analysis and source mechanisms determination. Furthermore, I performed the test “YES” or “NO” proposed by Davis and

Frohlich (1993), considering the location of boreholes and injection data provided for Húsmúli and Gráuhnúkar site, parts of Hellisheiði field.

The results show that:

- 1) Some shallow seismic events of clusters 3, 4 and 5, located close to Hellisheiði wells, show a relationship with injection activities. Furthermore, most of full moment tensor solutions of shallower master events have a quite large percentage of non-DC component, and particularly of the ISO component. These results suggest that the origin of such events might be induced or natural but not caused by pure shear faulting.
- 2) Deeper events, especially those belonging to cluster 1 and 7 with depth > 4 km, are distant from geothermal site and might have more a natural origin. In particular the seismic source of cluster 1 seems to be consistent with combination of shear and tensile faulting, typical of geothermal and volcanic earthquakes.
- 3) Clusters 2, 6 and 8 occurred quite close to Nesjavellir geothermal site, with different depths, however there is no deep injection at the site. The origin of such seismic events might be natural or linked to injection site by some tectonic structure as a possible fluid flow channel. In particular, the master event of cluster 8 shows a high percentage of non-DC component of moment tensor.

10. CONCLUSIONS

The Hengill area is a complex tectonic and geothermal active, located at the triple junction between the Reykjanes Peninsula (RP), the Western Volcanic Zone (WVZ), and the South Iceland Seismic Zone (SISZ). This region is seismically active and hosts the two largest operating geothermal power plants, located at the Nesjavellir and the Hellisheidi, for electrical power and heat production. Therefore, the origin of earthquakes may be either natural or anthropogenic. Given the coexistence of natural and anthropogenic drivers of seismicity in the area, the problem of discriminating among natural and induced events is here very challenging.

In this thesis, I investigated the seismicity at Hengill geothermal area recorded between 22 December 2018 and 31 January 2019, including a seismic sequence at the end of December 2018 with Mw 4.7 mainshock occurred on 30 December 2018. The dataset is composed by a large number of low magnitude events, characterized by high frequency content and noise contaminated signal.

To understand the source mechanisms and the origin of these seismic events, I used a very dense seismic monitoring network and apply full-waveform based methods for earthquake location, clustering analysis and source mechanism determination.

I first tested three different velocity models choosing the best one (Tryggvason et al., 2002) on the basis of maximum estimated coherence values, and then I computed earthquake locations. The depth distribution of seismicity highlights: 1) shallower events, with depth less than 4 km, occurred in the proximity of the geothermal fields, which seem to be clustered in three small clusters; 2) most of deeper events appear as a bigger separate cluster located outside the geothermal area.

The spatial clustering analysis identified eight clusters: shallower clusters are located in the proximity of Hellisheidi geothermal fields, whereas the hypocenters are deeper at the edge of geothermal site. The M_L 4.7 mainshock belongs to the biggest and deepest cluster, located in south of study area, on the neighbouring SISZ, where larger earthquakes occurred. Most of waveform clustering results show one waveform, suggesting similar earthquake source mechanisms.

Focal mechanism solutions of selected master events for three source models (DC, deviatoric, full) are consistent to each cluster. P and T axis orientation and the DC focal mechanisms are in agreement with the stress field of the area.

The decomposition of full solutions shows a quite large non-DC component, particularly the ISO component, for shallower master events, whereas the deeper ones are close to deviatoric solution. In particular, focal mechanisms of cluster 1 differ from the others due to the high percentage of positive CLVD in full solutions; this source model is agreement with a combination of shear and tensile faulting.

I even performed the test “YES” or “NO” proposed by Davis and Frohlich (1993), combining all results to discriminate between natural and induced seismicity.

The analysis indicated that the shallower seismicity near to Hellisheiði boreholes (cluster 3, 4, 5) show a relationship with injection activities as well as a large non-DC component. This suggests that their origin might be induced or due to natural drivers different from the pure shear faulting.

Deeper events belonging to cluster 1 and 7 with depth > 4 km, are distant from the geothermal sites and might have more likely natural origin. Some events of cluster 2, 6 and 8 occurred quite close to Nesjavellir geothermal site, with different depths, and might have a natural origin or be linked to injection site by some tectonic structure as a possible fluid flow channel.

This thesis provides a basic framework to characterize the seismic source and to understand the origin of seismic events at Hengill area, SW Iceland, through earthquake location, clustering analysis, seismic source mechanisms and spatio-temporal correlation between seismicity and anthropogenic activity.

To better constrain the origin of such seismic events, future work may include more information and data, for instance a greater dataset, hydrogeologic modelling and geomechanical properties. Thus, this analysis and the obtained results can be considered as the incipit for future investigation of seismicity in the area.

REFERENCES

- Adamova, P., Sokos, E., & Zahradnik, J. (2009). Problematic non-double-couple mechanism of the 2002 Amfilochia M w 5 earthquake, western Greece. *Journal of seismology*, 13(1), 1.
- Ágústsson, K., Kristjánssdóttir, S., Flóvenz, Ó. G., & Gudmundsson, O. (2015). Induced Seismic Activity during Drilling of Injection Wells at the Hellisheiði Power Plant, SW Iceland. In *Proceedings World Geothermal Congress*.
- Arnadóttir, T., Hreinsdóttir, S., Gudmundsson, G., Einarsson, P., Heinert, M., & Völkens, C. (2001). Crustal deformation measured by GPS in the South Iceland Seismic Zone due to two large earthquakes in June 2000. *Geophysical research letters*, 28(21), 4031-4033.
- Árnason, K., Eysteinnsson, H., & Hersir, G. P. (2010). Joint 1D inversion of TEM and MT data and 3D inversion of MT data in the Hengill area, SW Iceland. *Geothermics*, 39(1), 13-34.
- Arnórsson, S., Axelsson, G., Saemundsson, K. Geothermal systems in Iceland. *Jökull* 58, 269–302, 2008.
- Arnott, S. K., & Foulger, G. R. (1994 a). The Krafla spreading segment, Iceland: 1. Three-dimensional crustal structure and the spatial and temporal distribution of local earthquakes. *Journal of Geophysical Research: Solid Earth*, 99(B12), 23801-23825.
- Arnott, S. K., & Foulger, G. R. (1994 b). The Krafla spreading segment, Iceland: 2. The accretionary stress cycle and nonshear earthquake focal mechanisms. *Journal of Geophysical Research: Solid Earth*, 99(B12), 23827-23842.
- Baker, T., Granat, R., & Clayton, R. W. (2005). Real-time earthquake location using Kirchhoff reconstruction. *Bulletin of the Seismological Society of America*, 95(2), 699-707.
- Bardainne, T., Dubos-Sallée, N., Sénéchal, G., Gaillot, P., & Perroud, H. (2008). Analysis of the induced seismicity of the Lacq gas field (Southwestern France) and model of deformation. *Geophysical Journal International*, 172(3), 1151-1162.
- Bergerat, F., & Angelier, J. (2000). The South Iceland Seismic Zone: tectonic and sismotectonic analyses revealing the evolution from rifting to transform motion. *Journal of Geodynamics*, 29(3-5), 211-231.
- Bessason, J., Olafsson, E. H., Gunnarsson, G., Flóvenz, O. G., Jakobsdóttir, S. S., Björnsson, S., & Arnadóttir, T. (2012). Verklag vegna örvadrar skjálftavirkni í jardhitakerfum. Tech. Rep., Reykjavík, Orkuveitu Reykjavíkur.
- Bischoff, M., Cete, A., Fritschen, R., & Meier, T. (2010). Coal mining induced seismicity in the Ruhr area, Germany. *Pure and applied geophysics*, 167(1-2), 63-75.
- Björnsson, G., & ISOR, I. G. (2004, January). Reservoir conditions at 3-6 km depth in the Hellisheiði geothermal field, SW-Iceland, estimated by deep drilling, cold water injection and seismic monitoring. In *Proceedings* (pp. 26-28).

- Bodvarsson. R., Rognvaldsson. S. T., Jakobsdottir. S. S., Slunga. R., & Stefansson. R. (1996). The SIL data acquisition and monitoring system. *Seismological Research Letters*. 67(5). 35-46.
- Bommer, J. J., Crowley, H., & Pinho, R. (2015). A risk-mitigation approach to the management of induced seismicity. *Journal of Seismology*, 19(2), 623-646.
- Bourne. S. J., Oates. S. J., van Elk. J., & Doornhof. D. (2014). A seismological model for earthquakes induced by fluid extraction from a subsurface reservoir. *Journal of Geophysical Research: Solid Earth*. 119(12). 8991-9015.
- Broccardo, M., Mignan, A., Grigoli, F., Karvounis, D., Rinaldi, A. P., Danciu, L., ... & Hjörleifsdóttir, V. (2020). Induced seismicity risk analysis of the hydraulic stimulation of a geothermal well on Geldinganes, Iceland. *Natural Hazards and Earth System Sciences*, 20(6), 1573-1593.
- Brodsky. E. E., & Lajoie. L. J. (2013). Anthropogenic seismicity rates and operational parameters at the Salton Sea Geothermal Field. *Science*. 341(6145). 543-546.
- Burnham. K. P., & Anderson. D. R. (2002). A practical information-theoretic approach. *Model selection and multimodel inference*. 2nd ed. Springer. New York. 2.
- Cattaneo. M., Augliera. P., Spallarossa. D., & Lanza. V. (1999). A waveform similarity approach to investigate seismicity patterns. *Natural hazards*. 19(2-3). 123-138.
- Cesca. S. (2020). Seiscloud. a tool for density-based seismicity clustering and visualization. *Journal of Seismology*.
- Cesca. S., Buforn. E., & Dahm. T. (2006). Amplitude spectra moment tensor inversion of shallow earthquakes in Spain. *Geophysical Journal International*. 166(2). 839-854.
- Cesca. S., Grigoli. F., Heimann. S., Dahm. T., Kriegerowski. M., Sobiesiak. M., ... & Olcay. M. (2016). The M w 8.1 2014 Iquique, Chile, seismic sequence: a tale of foreshocks and aftershocks. *Geophysical Journal International*. 204(3). 1766-1780.
- Cesca. S., Grigoli. F., Heimann. S., González. A., Buforn. E., Maghsoudi. S., ... & Dahm. T. (2014). The 2013 September–October seismic sequence offshore Spain: a case of seismicity triggered by gas injection?. *Geophysical Journal International*. 198(2). 941-953.
- Cesca. S., Heimann. S., Stammer. K., & Dahm. T. (2010). Automated procedure for point and kinematic source inversion at regional distances. *Journal of Geophysical Research: Solid Earth*. 115(B6).
- Cesca. S., Letort. J., Razafindrakoto. H. N., Heimann. S., Rivalta. E., Isken. M. P., ... & Dahm. T. (2020). Drainage of a deep magma reservoir near Mayotte inferred from seismicity and deformation. *Nature Geoscience*. 13(1). 87-93.
- Cesca. S., Rohr. A., & Dahm. T. (2013). Discrimination of induced seismicity by full moment tensor inversion and decomposition. *Journal of seismology*. 17(1). 147-163.
- Cesca. S., Şen. A. T., & Dahm. T. (2014). Seismicity monitoring by cluster analysis of moment tensors. *Geophysical Journal International*. 196(3). 1813-1826.

- Cheng, Y., & Chen, X. (2018). Characteristics of seismicity inside and outside the Salton Sea Geothermal Field. *Bulletin of the Seismological Society of America*. 108(4). 1877-1888.
- Clarke, H., Eisner, L., Styles, P., & Turner, P. (2014). Felt seismicity associated with shale gas hydraulic fracturing: The first documented example in Europe. *Geophysical Research Letters*. 41(23). 8308-8314.
- Cornet, F. H., Helm, J., Poitrenaud, H., & Etchecopar, A. (1997). Seismic and aseismic slips induced by large-scale fluid injections. In *Seismicity associated with mines, reservoirs and fluid injections* (pp. 563-583). Birkhäuser, Basel.
- Cox, S. F. (2016). Injection-driven swarm seismicity and permeability enhancement: Implications for the dynamics of hydrothermal ore systems in high fluid-flux, overpressured faulting regimes—An invited paper. *Economic Geology*. 111(3). 559-587.
- Cuenot, N., & Genter, A. (2015, April). Microseismic activity induced during recent circulation tests at the Soultz-sous-Forêts EGS power plant. In *World geothermal congress* (pp. 20-24).
- Cuenot, N., Dorbath, C., & Dorbath, L. (2008). Analysis of the microseismicity induced by fluid injections at the EGS site of Soultz-sous-Forêts (Alsace, France): implications for the characterization of the geothermal reservoir properties. *Pure and Applied Geophysics*. 165(5). 797-828.
- Dahm, T., Becker, D., Bischoff, M., Cesca, S., Dost, B., Fritschen, R., ... & Meier, T. (2013). Recommendation for the discrimination of human-related and natural seismicity. *Journal of seismology*. 17(1). 197-202.
- Dahm, T., Cesca, S., Hainzl, S., Braun, T., & Krüger, F. (2015). Discrimination between induced, triggered, and natural earthquakes close to hydrocarbon reservoirs: A probabilistic approach based on the modeling of depletion-induced stress changes and seismological source parameters. *Journal of Geophysical Research: Solid Earth*. 120(4). 2491-2509.
- Davis, S. D., & Frohlich, C. (1993). Did (or will) fluid injection cause earthquakes?-criteria for a rational assessment. *Seismological Research Letters*. 64(3-4). 207-224.
- Davis, S. D., Nyffenegger, P. A., & Frohlich, C. (1995). The 9 April 1993 earthquake in south-central Texas: Was it induced by fluid withdrawal?. *Bulletin of the Seismological Society of America*. 85(6). 1888-1895.
- Davis, Scott D., and Cliff Frohlich. "Did (or will) fluid injection cause earthquakes?-criteria for a rational assessment." *Seismological Research Letters* 64.3-4 (1993): 207-224.
- Decriem, J., Árnadóttir, T., Hooper, A., Geirsson, H., Sigmundsson, F., Keiding, M., ... & Bennett, R. A. (2010). The 2008 May 29 earthquake doublet in SW Iceland. *Geophysical Journal International*. 181(2). 1128-1146.
- Deichmann, N., & Garcia-Fernandez, M. (1992). Rupture geometry from high-precision relative hypocentre locations of microearthquake clusters. *Geophysical Journal International*. 110(3). 501-51

- Deichmann. N.. & Giardini. D. (2009). Earthquakes induced by the stimulation of an enhanced geothermal system below Basel (Switzerland). *Seismological Research Letters*. 80(5). 784-798.
- Dieterich. J. H.. Richards-Dinger. K. B.. & Kroll. K. A. (2015). Modeling injection-induced seismicity with the physics-based earthquake simulator RSQSim. *Seismological Research Letters*. 86(4). 1102-1109.
- Dorbath. L.. Cuenot. N.. Genter. A.. & Frogneux. M. (2009). Seismic response of the fractured and faulted granite of Soultz-sous-Forêts (France) to 5 km deep massive water injections. *Geophysical Journal International*. 177(2). 653-675.
- Douglas. A. (1967). Joint epicentre determination. *Nature*. 215(5096). 47-48.
- Dreger. D. S.. Ford. S. R.. & Walter. W. R. (2008). Source analysis of the Crandall Canyon, Utah, mine collapse. *Science*. 321(5886). 217-217.
- Dreger. D.. & Woods. B. (2002). Regional distance seismic moment tensors of nuclear explosions. *Tectonophysics*. 356(1-3). 139-156.
- Drew. J. E.. Leslie. H. D.. Armstrong. P. N.. & Michard. G. (2005. January). Automated microseismic event detection and location by continuous spatial mapping. In *SPE Annual Technical Conference and Exhibition*. Society of Petroleum Engineers.
- Eberhart-Phillips. D.. & Oppenheimer. D. H. (1984). Induced seismicity in The Geysers geothermal area, California. *Journal of Geophysical Research: Solid Earth*. 89(B2). 1191-1207
- Edwards. B.. Kraft. T.. Cauzzi. C.. Kästli. P.. & Wiemer. S. (2015). Seismic monitoring and analysis of deep geothermal projects in St Gallen and Basel, Switzerland. *Geophysical Journal International*. 201(2). 1022-1039.
- Einarsson. P. (1991). Earthquakes and present-day tectonism in Iceland. *Tectonophysics*. 189(1-4). 261-279.
- Einarsson. P. (2008). Plate boundaries, rifts and transforms in Iceland. *Jökull*. 58(12). 35-58.
- Ekström. G. (2006). Global detection and location of seismic sources by using surface waves. *Bulletin of the Seismological Society of America*. 96(4A). 1201-1212.
- Ellsworth. W. L.. Giardini. D.. Townend. J.. Ge. S.. & Shimamoto. T. (2019). Triggering of the Pohang, Korea, earthquake (M w 5.5) by enhanced geothermal system stimulation. *Seismological Research Letters*. 90(5). 1844-1858.
- Ester. M.. Krieger. H. P.. Sander. J.. & Xu. X. (1996. August). A density-based algorithm for discovering clusters in large spatial databases with noise. In *Kdd* (Vol. 96. No. 34. pp. 226-231).
- Fischer. T.. Horálek. J.. Hrubcová. P.. Vavryčuk. V.. Bräuer. K.. & Kämpf. H. (2014). Intra-continental earthquake swarms in West-Bohemia and Vogtland: a review. *Tectonophysics*. 611. 1-27.
- Ford. S. R.. Dreger. D. S.. & Walter. W. R. (2009). Identifying isotropic events using a regional moment tensor inversion. *Journal of Geophysical Research: Solid Earth*. 114(B1).

- Foulger. G. R. (1988 a). Hengill triple junction. SW Iceland 1. Tectonic structure and the spatial and temporal distribution of local earthquakes. *Journal of Geophysical Research: Solid Earth*. 93(B11). 13493-13506.
- Foulger. G. R. (1988 b). Hengill triple junction. SW Iceland 2. Anomalous earthquake focal mechanisms and implications for process within the geothermal reservoir and at accretionary plate boundaries. *Journal of Geophysical Research: Solid Earth*. 93(B11). 13507-13523
- Foulger. G. R., Julian. B. R., Hill. D. P., Pitt. A. M., Malin. P. E., & Shalev. E. (2004). Non-double-couple microearthquakes at Long Valley caldera, California, provide evidence for hydraulic fracturing. *Journal of Volcanology and Geothermal Research*. 132(1). 45-71.
- Foulger. G. R., Miller. A. D., Julian. B. R., & Evans. J. R. (1995). Three-dimensional v_p and v_p/v_s structure of the Hengill Triple Junction and Geothermal Area, Iceland, and the repeatability of tomographic inversion. *Geophysical research letters*. 22(10). 1309-1312.
- Foulger. G., & Long. R. E. (1984). Anomalous focal mechanisms: Tensile crack formation on an accreting plate boundary. *Nature*. 310(5972). 43-45
- Franzson. H., Gunnlaugsson. E., Árnason. K., Sæmundsson. K., Steingrímsson. B., & Hardarson. B. S. (2010, April). The Hengill geothermal system, conceptual model and thermal evolution. In *Proceedings World Geothermal Congress (Vol. 25, p. 1)*.
- Gaité. B., Ugalde. A., Villaseñor. A., & Blanch. E. (2016). Improving the location of induced earthquakes associated with an underground gas storage in the Gulf of Valencia (Spain). *Physics of the Earth and Planetary Interiors*. 254. 46-59.
- Gajewski. D., & Tessmer. E. (2005). Reverse modelling for seismic event characterization. *Geophysical Journal International*. 163(1). 276-284.
- Geiger. L. (1912). Probability method for the determination of earthquake epicenters from the arrival time only. *Bull. St. Louis Univ.* 8(1). 56-71.
- Gharti. H. N., Oye. V., Roth. M., & Kühn. D. (2010). Automated microearthquake location using envelope stacking and robust global optimization. *Automated microearthquake location. Geophysics*. 75(4). MA27-MA46.
- Gilbert. F. (1971). Excitation of the normal modes of the Earth by earthquake sources. *Geophysical Journal International*. 22(2). 223-226.
- Goebel. T. H. W., Hauksson. E., Aminzadeh. F., & Ampuero. J. P. (2015). An objective method for the assessment of fluid injection-induced seismicity and application to tectonically active regions in central California. *Journal of Geophysical Research: Solid Earth*. 120(10). 7013-7032.
- Grasso. J. R., & Wittlinger. G. (1990). Ten years of seismic monitoring over a gas field. *Bulletin of the Seismological Society of America*. 80(2). 450-473.
- Grigoli. F., Cesca. S., Amoroso. O., Emolo. A., Zollo. A., & Dahm. T. (2014). Automated seismic event location by waveform coherence analysis. *Geophysical Journal International*. 196(3). 1742-1753.

- Grigoli. F., Cesca. S., Priolo. E., Rinaldi. A. P., Clinton. J. F., Stabile. T. A., ... & Dahm. T. (2017). Current challenges in monitoring, discrimination, and management of induced seismicity related to underground industrial activities: A European perspective. *Reviews of Geophysics*. 55(2). 310-340.
- Grigoli. F., Cesca. S., Rinaldi. A. P., Manconi. A., Lopez-Comino. J. A., Clinton. J. F., ... & Wiemer. S. (2018). The November 2017 Mw 5.5 Pohang earthquake: A possible case of induced seismicity in South Korea. *Science*. 360(6392). 1003-1006.
- Grigoli. F., Cesca. S., Vassallo. M., & Dahm. T. (2013). Automated seismic event location by travel-time stacking: An application to mining induced seismicity. *Seismological Research Letters*. 84(4). 666-677.
- Guilhem. A., Hutchings. L., Dreger. D. S., & Johnson. L. R. (2014). Moment tensor inversions of M_w ~ 3 earthquakes in the Geysers geothermal fields, California. *Journal of Geophysical Research: Solid Earth*. 119(3). 2121-2137.
- Gunnarsson. A., Steingrímsson. B. S., Gunnlaugsson. E., Magnusson. J., & Maack. R. (1992). Nesjavellir geothermal co-generation power plant. *Geothermics*. 21(4). 559-583.
- Gunnarsson. G. (2013 a). Temperature Dependent Injectivity and Induced Seismicity—Managing Reinjection in the Hellisheiði Field, SW-Iceland. *GRC Transactions*. 37. 1019-1025.
- Gunnarsson. I., Aradóttir. E. S., Sigfússon. B., Gunnlaugsson. E., Júlíusson. B. M., & Energy. R. (2013 b). Geothermal gas emission from Hellisheiði and Nesjavellir power plants, Iceland. *GRC Transactions*. 37. 7859.
- Hainzl. S., & Ogata. Y. (2005). Detecting fluid signals in seismicity data through statistical earthquake modeling. *Journal of Geophysical Research: Solid Earth*. 110(B5)
- Hainzl. S., Zöller. G., & Kurths. J. (2000). Self-organization of spatio-temporal earthquake clusters.
- Hardarson. B. S., Einarsson. G. M., Krittjánsson. B. R., Gunnarsson. G., Helgadóttir. H. M., Franzson. H., ... & Gunnlaugsson. E. (2010, April). Geothermal reinjection at the hengill triple junction, SW Iceland. In *Proceedings World Geothermal Congress*. Bali, Indonesia (pp. 25-29).
- Hardebeck. J. L., & Shearer. P. M. (2003). Using S/P amplitude ratios to constrain the focal mechanisms of small earthquakes. *Bulletin of the Seismological Society of America*. 93(6). 2434-2444.
- Häring. M. O., Schanz. U., Ladner. F., & Dyer. B. C. (2008). Characterisation of the Basel 1 enhanced geothermal system. *Geothermics*. 37(5). 469-495.
- Hauksson. E., & Unruh. J. (2007). Regional tectonics of the Coso geothermal area along the intracontinental plate boundary in central eastern California: Three-dimensional V_p and V_p/V_s models, spatial-temporal seismicity patterns, and seismogenic deformation. *Journal of Geophysical Research: Solid Earth*. 112(B6).
- Heimann. Sebastian; Isken. Marius; Kühn. Daniela; Sudhaus. Henriette; Steinberg. Andreas; Vasyura-Bathke. Hannes; Daout. Simon; Cesca. Simone; Dahm. Torsten (2018): *Grond - A*

probabilistic earthquake source inversion framework. V. 1.0. GFZ Data Services. <https://doi.org/10.5880/GFZ.2.1.2018.003>

- Hreinsdóttir. S., Árnadóttir. T., Decriem. J., Geirsson. H., Tryggvason. A., Bennett. R. A., & LaFemina. P. (2009). A complex earthquake sequence captured by the continuous GPS network in SW Iceland. *Geophysical Research Letters*. 36(12).
- Hreinsdóttir. S., Árnadóttir. T., Decriem. J., Geirsson. H., Tryggvason. A., Bennett. R. A., & LaFemina. P. (2009). A complex earthquake sequence captured by the continuous GPS network in SW Iceland. *Geophysical Research Letters*. 36(12).
- Improta. L., Valoroso. L., Piccinini. D., & Chiarabba. C. (2015). A detailed analysis of wastewater-induced seismicity in the Val d'Agri oil field (Italy). *Geophysical Research Letters*. 42(8). 2682-2690.
- Jakobsdóttir. S. S. (2008). Seismicity in Iceland: 1994–2007. *Jökull*. 58. 75-100.
- Jechumtálová. Z., & Šílený. J. (2005). Amplitude ratios for complete moment tensor retrieval. *Geophysical Research Letters*. 32(22).
- Jost. M. U., & Herrmann. R. B. (1989). A student's guide to and review of moment tensors. *Seismological Research Letters*. 60(2). 37-57.
- Jousset. P., Haberland. C., Bauer. K., & Arnason. K. (2011). Hengill geothermal volcanic complex (Iceland) characterized by integrated geophysical observations. *Geothermics*. 40(1). 1-24.
- Julian. B. R., Miller. A. D., & Foulger. G. R. (1997). Non-double-couple earthquake mechanisms at the Hengill-Grensdalur volcanic complex, southwest Iceland. *Geophysical Research Letters*. 24(7). 743-746.
- Juncu. D., Árnadóttir. T., Geirsson. H., Guðmundsson. G. B., Lund. B., Gunnarsson. G., ... & Michalczevska. K. (2020). Injection-induced surface deformation and seismicity at the Hellisheidi geothermal field, Iceland. *Journal of Volcanology and Geothermal Research*. 391. 106337.
- Kagan. Y. Y., & Jackson. D. D. (1991). Long-term earthquake clustering. *Geophysical Journal International*. 104(1). 117-133.
- Kagan. Y., & Knopoff. L. (1976). Statistical search for non-random features of the seismicity of strong earthquakes. *Physics of the earth and planetary interiors*. 12(4). 291-318.
- Kao. H., & Shan. S. J. (2004). The source-scanning algorithm: Mapping the distribution of seismic sources in time and space. *Geophysical Journal International*. 157(2). 589-594.
- Kao. H., & Shan. S. J. (2007). Rapid identification of earthquake rupture plane using source-scanning algorithm. *Geophysical Journal International*. 168(3). 1011-1020.
- Kass. R. E., & Raftery. A. E. (1995). Bayes factors. *Journal of the american statistical association*. 90(430). 773-795.
- Kaven. J. O., Hickman. S. H., & Davatzes. N. C. (2014, February). Micro-seismicity and seismic moment release within the Coso Geothermal Field, California. In *Proceedings of the 39th Workshop on Geothermal Reservoir Engineering* (p. 10)

- Khodayar. M.. & Björnsson. S. (2014). Fault ruptures and geothermal effects of the second earthquake. 29 May 2008. South Iceland Seismic Zone. *Geothermics*. 50. 44-65.
- Klein. F. W.. Einarsson. P.. & Wyss. M. (1977). The Reykjanes Peninsula. Iceland. earthquake swarm of September 1972 and its tectonic significance. *Journal of Geophysical Research*. 82(5). 865-888.
- Konstantaras. A. J.. Katsifarakis. E.. Maravelakis. E.. Skounakis. E.. Kokkinos. E.. & Karapidakis. E. (2012). Intelligent spatial-clustering of seismicity in the vicinity of the Hellenic Seismic Arc. *Earth Science Research*. 1(2). 1.
- Koper. K. D.. Pechmann. J. C.. Burlacu. R.. Pankow. K. L.. Stein. J.. Hale. J. M.. ... & McCarter. M. K. (2016). Magnitude-based discrimination of man-made seismic events from naturally occurring earthquakes in Utah. USA. *Geophysical Research Letters*. 43(20). 10-638.
- Kwiatek. G.. Martínez-Garzón. P.. & Bohnhoff. M. (2016). HybridMT: A MATLAB/shell environment package for seismic moment tensor inversion and refinement. *Seismological Research Letters*. 87(4). 964-976.
- Langenbruch. C.. & Zoback. M. D. (2016). How will induced seismicity in Oklahoma respond to decreased saltwater injection rates?. *Science advances*. 2(11). e1601542.
- Lasocki. S. (2014). Transformation to equivalent dimensions—a new methodology to study earthquake clustering. *Geophysical Journal International*. 197(2). 1224-1235.
- Lee. W. H. K.. & Lahr. J. C. (1972). HYPO71: A computer program for determining hypocenter. magnitude. and first motion pattern of local earthquakes (p. 100). US Department of the Interior. Geological Survey. National Center for Earthquake Research.
- Liao. Y. C.. Kao. H.. Rosenberger. A.. Hsu. S. K.. & Huang. B. S. (2012). Delineating complex spatiotemporal distribution of earthquake aftershocks: An improved source-scanning algorithm. *Geophysical Journal International*. 189(3). 1753-1770.
- Lippiello. E.. Marzocchi. W.. de Arcangelis. L.. & Godano. C. (2012). Spatial organization of foreshocks as a tool to forecast large earthquakes. *Scientific reports*. 2. 846.
- Lizurek. G.. & Lasocki. S. (2014). Clustering of mining-induced seismic events in equivalent dimension spaces. *Journal of seismology*. 18(3). 543-563.
- Lomax. A.. & Curtis. A. (2001). Fast. probabilistic earthquake location in 3D models using oct-tree importance sampling. In *Geophys. Res. Abstr* (Vol. 3. p. 955).
- Lomax. A.. Virieux. J.. Volant. P.. & Berge-Thierry. C. (2000). Probabilistic earthquake location in 3D and layered models. In *Advances in seismic event location* (pp. 101-134). Springer. Dordrecht.
- Manley. C. R.. & Bacon. C. R. (2000). Rhyolite thermobarometry and the shallowing of the magma reservoir. Coso volcanic field. California. *Journal of Petrology*. 41(1). 149-174.
- Martens. H. R.. & White. R. S. (2013). Triggering of microearthquakes in Iceland by volatiles released from a dyke intrusion. *Geophysical Journal International*. 194(3). 1738-1754.

- Martínez-Garzón. P., Kwiatek. G., Bohnhoff. M., & Dresen. G. (2017). Volumetric components in the earthquake source related to fluid injection and stress state. *Geophysical Research Letters*. 44(2). 800-809.
- Maurer. H., & Deichmann. N. (1995). Microearthquake cluster detection based on waveform similarities. with an application to the western Swiss Alps. *Geophysical Journal International*. 123(2). 588-600.
- Maury. V., Grasso. J. R., & Wittlinger. G. (1990, January). Lacq gas field (France): Monitoring of induced subsidence and seismicity consequences on gas production and field operation. In *European Petroleum Conference*. Society of Petroleum Engineers.
- McGarr. A., and D. Simpson (1997). Keynote lecture: A broad look at induced and triggered seismicity. in *Rockbursts and Seismicity in Mines*. edited by S. J. Gibowitz and S. Lasocki. pp. 948-970. Balkema. Rotterdam.
- McMechan. G. A. (1982). Determination of source parameters by wavefield extrapolation. *Geophysical Journal International*. 71(3). 613-628.
- Miller. A. D., Julian. B. R., & Foulger. G. R. (1998). Three-dimensional seismic structure and moment tensors of non-double-couple earthquakes at the Hengill–Grensdalur volcanic complex. Iceland. *Geophysical Journal International*. 133(2). 309-325.
- Milne. J. (1886). *Earthquakes and other earth movements* (Vol. 56). K. Paul. Trench.
- Moriya. H., Niitsuma. H., & Baria. R. (2003). Multiplet-clustering analysis for estimation of fine detail structures in seismic clouds at Soultz field. France. *Bull. seism. Soc. Am.* 93. 1606-1620.
- Myers. S. C., Johannesson. G., & Hanley. W. (2007). A Bayesian hierarchical method for multiple-event seismic location. *Geophysical Journal International*. 171(3). 1049-1063.
- Nakamura. M. (2002). Determination of focal mechanism solution using initial motion polarity of P and S waves. *Physics of the Earth and Planetary Interiors*. 130(1-2). 17-29.
- Ouillon. G., & Sornette. D. (2011). Segmentation of fault networks determined from spatial clustering of earthquakes. *Journal of Geophysical Research: Solid Earth*. 116(B2).
- Passarelli. L., Maccaferri. F., Rivalta. E., Dahm. T., & Boku. E. A. (2013). A probabilistic approach for the classification of earthquakes as ‘triggered’ or ‘not triggered’. *Journal of seismology*. 17(1). 165-187.
- Podvin. P., & Lecomte. I. (1991). Finite difference computation of traveltimes in very contrasted velocity models: a massively parallel approach and its associated tools. *Geophysical Journal International*. 105(1). 271-284.
- Ratouis. T. M., Snæbjörnsdóttir. S. O., Gunnarsson. G., Gunnarsson. I., Kristjánsson. B. R., & Aradóttir. E. S. (2019). Modelling the Complex Structural Features Controlling Fluid Flow at the CarbFix2 Reinjection Site. Hellisheiði Geothermal Power Plant. SW-Iceland. In *44th Workshop on Geothermal Reservoir Engineering*.

- Reasenberg. P. A. (1985). FPFIT. FPLOT. and FPPAGE: Fortran computer programs for calculating and displaying earthquake fault-plane solutions. US Geol. Surv. Open-File Rep.. 85-739.
- Reid. H.F. (1910). The Mechanics of the Earthquake. Vol. II of The California Earthquake of April 18. 1906. in Report of the State Earthquake Investigation Commisision. ed Lawson. A. C. Carnegie Institution of Washington.
- Rögnvaldsson. S. T. (1998). Overview of the 1993-1996 seismicity near Hengill. Veðurstofa Íslands.
- Ross. A. C. (1996). The Geysers geothermal area. California: Tomographic images of the depleted steam reservoir and non-double-couple earthquakes (Doctoral dissertation. Durham University)
- Ross. A., Foulger. G. R., & Julian. B. R. (1999). Source processes of industrially-induced earthquakes at The Geysers geothermal area. California. Geophysics. 64(6). 1877-1889.
- Saemundsson. K. (1979). Outline of the geology of Iceland. Jokull. 29. 7-28.
- Sæmundsson. K. (1995). Hengill. geological map (bedrock) 1: 50000. National Energy Authority. Reykjavík Municipal Heating and Iceland Geodetic Survey.
- Sambridge. M. S., & Kennett. B. L. N. (1986). A novel method of hypocentre location. Geophysical Journal International. 87(2). 679-697.
- Sambridge. M., & Mosegaard. K. (2002). Monte Carlo methods in geophysical inverse problems. Reviews of Geophysics. 40(3). 3-1.
- Schaefer. A. M., Daniell. J. E., & Wenzel. F. (2017). The smart cluster method. Journal of Seismology. 21(4). 965-985.
- Schoenball. M., Davatzes. N. C., & Glen. J. M. (2015). Differentiating induced and natural seismicity using space-time-magnitude statistics applied to the Coso Geothermal field. Geophysical Research Letters. 42(15). 6221-6228.
- Segall. P., Grasso. J. R., & Mossop. A. (1994). Poroelastic stressing and induced seismicity near the Lacq gas field. southwestern France. Journal of Geophysical Research: Solid Earth. 99(B8). 15423-15438.
- Sgattoni. G., Gudmundsson. Ó., Einarsson. P., & Lucchi. F. (2016). Joint relative location of earthquakes without a pre-defined velocity model: an example from a peculiar seismic cluster on Katla volcano's south-flank (Iceland). Geophysical Supplements to the Monthly Notices of the Royal Astronomical Society. 207(2). 1244-1257.
- Shapiro. S., O. S. Krger. and C. Dinske (2013). Probability of inducing given magnitude earthquakes by perturbing finite volumes of rocks. J. Geophys. Res. Solid Earth. 118. 3557-3575. doi:10.1002/jgrb.50264.
- Sigmundsson. F., Einarsson. P., Rögnvaldsson. S. T., Foulger. G. R., Hodgkinson. K. M., & Thorbergsson. G. (1997). The 1994–1995 seismicity and deformation at the Hengill triple junction.

- Iceland: Triggering of earthquakes by minor magma injection in a zone of horizontal shear stress. *Journal of Geophysical Research: Solid Earth*. 102(B7). 15151-15161
- Šílený. J., Hill. D. P., Eisner. L., & Cornet. F. H. (2009). Non-double-couple mechanisms of microearthquakes induced by hydraulic fracturing. *Journal of Geophysical Research: Solid Earth*. 114(B8).
 - Šílený. J., Hill. D. P., Eisner. L., & Cornet. F. H. (2009). Non-double-couple mechanisms of microearthquakes induced by hydraulic fracturing. *Journal of Geophysical Research: Solid Earth*. 114(B8).
 - Sokos. E. N., & Zahradnik. J. (2008). ISOLA a Fortran code and a Matlab GUI to perform multiple-point source inversion of seismic data. *Computers & Geosciences*. 34(8). 967-977.
 - Sornette. D., & Werner. M. J. (2005). Apparent clustering and apparent background earthquakes biased by undetected seismicity. *Journal of Geophysical Research: Solid Earth*. 110(B9).
 - Stefánsson. R., & Halldórsson. P. (1988). Strain release and strain build-up in the South Iceland seismic zone. *Tectonophysics*. 152(3-4). 267-276.
 - Stefánsson. R., Böðvarsson. R., Slunga. R., Einarsson. P., Jakobsdóttir. S., Bungum. H., ... & Korhonen. H. (1993). Earthquake prediction research in the South Iceland Seismic Zone and the SIL project. *Bulletin of the Seismological Society of America*. 83(3). 696-716.
 - Steigerwald. L., Einarsson. P., & Hjartardóttir. Á. R. (2020). Fault kinematics at the Hengill Triple Junction, SW-Iceland, derived from surface fracture pattern. *Journal of Volcanology and Geothermal Research*. 391. 106439.
 - Sveinbjörnsson. B. M., & Þórhallsson. S. (2013). Drilling performance and productivity of geothermal wells—Case history from Hengill Geothermal Area in Iceland. In *Proceedings of the ARMA 47th US Rock Mechanics–Geomechanics Symposium held in San Francisco, CA, USA, 23–26 June 2013*.
 - Tarantola. A., & Valette. B. (1982). Inverse problems= quest for information. *Journal of Geophysics*| IF 32.18. 50(1). 159-170.
 - Toomey. D. R., & Foulger. G. R. (1989). Tomographic inversion of local earthquake data from the Hengill-Grensdalur central volcano complex, Iceland. *Journal of Geophysical Research: Solid Earth*. 94(B12). 17497-17510.
 - Tryggvason. A., Rögnvaldsson S þur T., Flóvenz ÓG (2002) Threedimensional imaging of the P-and S-wave velocity structure and earthquake locations beneath southwest Iceland. *Geophys J Int*. 151. 848-866.
 - Vavryčuk. V. (2002). Non-double-couple earthquakes of 1997 January in West Bohemia, Czech Republic: evidence of tensile faulting. *Geophysical Journal International*. 149(2). 364-373.
 - Vavryčuk. V. (2015). Moment tensor decompositions revisited. *Journal of Seismology*. 19(1). 231-252.

- Vavryčuk. V. & Kühn. D. (2012). Moment tensor inversion of waveforms: a two-step time-frequency approach. *Geophysical Journal International*. 190(3). 1761-1776.
- Vavryčuk. V., Bohnhoff. M., Jechumtálová. Z., Kolář. P., & Šílený. J. (2008). Non-double-couple mechanisms of microearthquakes induced during the 2000 injection experiment at the KTB site. Germany: A result of tensile faulting or anisotropy of a rock?. *Tectonophysics*. 456(1-2). 74-93.
- Verdon. J. P., Baptie. B. J., & Bommer. J. J. (2019). An Improved Framework for Discriminating Seismicity Induced by Industrial Activities from Natural Earthquakes. *Seismological Research Letters*. 90(4). 1592-1611.
- Vogfjörð. K. S., & Hjaltadóttir. S. (2007). Kortlagning skjálftavirkni við Hverahlíð á Hellisheiði í febrúar 2006. Unnið fyrir Orkuveitu Reykjavíkur. Icelandic Meteorological Office.
- Waldhauser. F., & Ellsworth. W. L. (2000). A double-difference earthquake location algorithm: Method and application to the northern Hayward fault. California. *Bulletin of the Seismological Society of America*. 90(6). 1353-1368.
- Wang. R. (1999). A simple orthonormalization method for stable and efficient computation of Green's functions. *Bulletin of the Seismological Society of America*. 89(3). 733-741.
- Wehling-Benatelli. S., Becker. D., Bischoff. M., Friederich. W., & Meier. T. (2013). Indications for different types of brittle failure due to active coal mining using waveform similarities of induced seismic events. *Solid Earth*. 4(2).
- Willemann. R. J. (1993). Cluster analysis of seismic moment tensor orientations. *Geophysical Journal International*. 115(3). 617-634.
- Wilson. M. P., Davies. R. J., Foulger. G. R., Julian. B. R., Styles. P., Gluyas. J. G., & Almond. S. (2015). Anthropogenic earthquakes in the UK: A national baseline prior to shale exploitation. *Marine and Petroleum Geology*. 68. 1-17.
- Wolfe. C. J., Bjarnason. I. T., VanDecar. J. C., & Solomon. S. C. (1997). Seismic structure of the Iceland mantle plume. *Nature*. 385(6613). 245-247.
- Zahradnik. J., Jansky. J., & Plicka. V. (2008). Detailed waveform inversion for moment tensors of $M \sim 4$ events: Examples from the Corinth Gulf. Greece. *Bulletin of the Seismological Society of America*. 98(6). 2756-2771.
- Zaliapin. I., & Ben-Zion. Y. (2016). Discriminating characteristics of tectonic and human-induced seismicity. *Bulletin of the Seismological Society of America*. 106(3). 846-859.
- Zaliapin. I., Gabrielov. A., Keilis-Borok. V., & Wong. H. (2008). Clustering analysis of seismicity
- Zeng. X., Zhang. H., Zhang. X., Wang. H., Zhang. Y., & Liu. Q. (2014). Surface microseismic monitoring of hydraulic fracturing of a shale-gas reservoir using short-period and broadband seismic sensors. *Seismological Research Letters*. 85(3). 668-677.

- Zhao, P., Kühn, D., Oye, V., & Cesca, S. (2014). Evidence for tensile faulting deduced from full waveform moment tensor inversion during the stimulation of the Basel enhanced geothermal system. *Geothermics*, 52, 74-83.

Appendix A. Catalogue

Table A.1 - Catalogue

Date	Latitude	Longitude	Depth(km)
22/12/18 8.18	64.04929	-21.39755	1.8551
22/12/18 8.19	64.07494	-21.40026	3.6174
22/12/18 11.00	64.11058	-21.28347	5.4332
22/12/18 11.41	63.94308	-21.43315	5.5874
22/12/18 13.18	64.10698	-21.29165	5.5787
22/12/18 15.04	63.95171	-21.36793	6.1886
22/12/18 17.51	64.06689	-21.26795	3.5358
22/12/18 17.52	64.06753	-21.27329	3.6000
22/12/18 18.16	64.11419	-21.27530	4.4000
22/12/18 21.19	64.05674	-21.28293	3.1304
22/12/18 21.36	64.10698	-21.29165	5.4986
22/12/18 21.40	64.05673	-21.28472	3.1126
22/12/18 22.02	64.08679	-21.31605	1.1327
22/12/18 22.43	64.09604	-21.36619	3.7876
22/12/18 23.36	64.08512	-21.42267	4.8000
22/12/18 23.39	64.03693	-21.39510	3.7018
23/12/18 0.00	63.97700	-21.33914	6.6268
23/12/18 0.08	64.07916	-21.64563	4.5608
23/12/18 2.17	64.06180	-21.17942	4.1991
23/12/18 2.41	64.05472	-21.42024	0.0766
23/12/18 3.05	64.11119	-21.35738	3.6000
23/12/18 3.06	64.11200	-21.35739	3.6000
23/12/18 4.30	64.01642	-21.37387	2.3952
23/12/18 5.03	64.11692	-21.35428	4.3677
23/12/18 5.27	63.94713	-21.48178	4.0077
23/12/18 7.04	63.95935	-21.44360	6.2415
23/12/18 8.01	64.05319	-21.25972	2.8000
23/12/18 8.28	64.05705	-21.40585	2.0721
23/12/18 8.32	64.05645	-21.40584	2.0000
23/12/18 8.37	64.05645	-21.40584	2.0000
23/12/18 11.07	64.11418	-21.28055	2.4000
23/12/18 11.08	64.11339	-21.27529	2.9565
23/12/18 11.17	64.11139	-21.27710	2.3141
23/12/18 13.08	63.93796	-21.41512	6.9468
23/12/18 14.55	64.11779	-21.26712	3.5116
23/12/18 17.28	64.04567	-21.40758	2.2218
23/12/18 17.37	64.04206	-21.41666	2.0693
23/12/18 18.47	64.04329	-21.40709	2.0000
23/12/18 18.51	64.04207	-21.41382	2.3141
23/12/18 18.52	64.04486	-21.40567	2.2249
23/12/18 19.42	63.95548	-21.44244	6.4000

23/12/18 20.22	63.84967	-21.12679	6.2433
24/12/18 9.46	64.10698	-21.29165	2.1721
24/12/18 10.51	64.10339	-21.28986	5.6000
24/12/18 12.51	64.10340	-21.28192	4.9478
24/12/18 13.37	64.10062	-21.28337	5.2000
24/12/18 14.01	64.10430	-21.27962	5.6136
24/12/18 15.45	64.10340	-21.28340	5.4427
24/12/18 15.50	63.91904	-21.26044	4.0000
24/12/18 17.08	64.05288	-21.39892	1.3567
24/12/18 17.18	63.94884	-21.37452	6.8673
24/12/18 17.21	63.94884	-21.37456	6.8000
24/12/18 17.52	64.10340	-21.28187	5.7427
24/12/18 18.30	64.02526	-21.39879	0.2087
24/12/18 20.03	64.03815	-21.42264	2.0000
24/12/18 20.54	63.93449	-21.52031	8.4183
24/12/18 21.29	63.95294	-21.66983	2.0579
24/12/18 21.36	64.09322	-21.16301	11.0308
25/12/18 2.51	64.01692	-21.42163	2.8000
25/12/18 3.59	64.04865	-21.30724	3.1500
25/12/18 4.36	64.05318	-21.26650	3.6000
25/12/18 15.44	63.95161	-21.39380	6.1525
25/12/18 22.41	64.10470	-21.35897	3.4908
25/12/18 23.19	64.11333	-21.35585	3.6703
26/12/18 6.05	64.01966	-21.42168	1.1596
26/12/18 6.17	64.01858	-21.42926	1.7383
26/12/18 7.22	64.02287	-21.40490	1.5110
26/12/18 7.22	64.02085	-21.41573	1.8159
26/12/18 8.01	64.02110	-21.42988	1.5311
26/12/18 12.35	64.00338	-21.37093	2.2577
26/12/18 14.06	64.05829	-21.28294	3.2756
26/12/18 22.59	63.99084	-21.47588	8.3007
27/12/18 5.07	64.05286	-21.40579	1.7450
27/12/18 12.26	63.95746	-21.74103	9.1762
27/12/18 17.56	63.93964	-21.33174	6.1304
27/12/18 22.05	64.04240	-21.27459	4.4000
27/12/18 22.36	63.96915	-21.12855	9.4303
27/12/18 22.59	64.01311	-21.43497	2.4897
28/12/18 2.04	64.01281	-21.42975	3.3100
28/12/18 2.13	64.11197	-21.35739	3.6000
28/12/18 2.45	64.10699	-21.28563	5.2058
28/12/18 4.01	64.01766	-21.38073	2.1439
28/12/18 7.07	64.01484	-21.37886	2.6449
28/12/18 10.39	64.05674	-21.28293	2.8000
28/12/18 11.23	64.05289	-21.39256	2.0844
28/12/18 14.49	64.05827	-21.27822	2.7115
28/12/18 15.28	64.06154	-21.29000	2.1944
28/12/18 20.04	64.01294	-21.61723	3.1977
29/12/18 3.19	64.05066	-21.25588	3.5712

29/12/18 8.53	63.96530	-21.15295	9.1561
29/12/18 10.54	64.05111	-21.26025	3.6000
29/12/18 15.07	64.01689	-21.42982	1.6000
29/12/18 16.56	63.95850	-21.17536	8.5340
29/12/18 17.18	64.05985	-21.29219	2.8000
29/12/18 17.28	64.04608	-21.33094	2.4627
29/12/18 18.36	63.96405	-21.10420	9.5823
29/12/18 19.08	64.00717	-21.37241	2.2430
29/12/18 19.23	64.17083	-21.85718	11.8812
29/12/18 21.33	63.95254	-21.32932	5.2756
29/12/18 22.55	63.97812	-21.47806	5.9723
30/12/18 2.56	63.97262	-21.32625	7.0468
30/12/18 2.57	63.96252	-21.33707	6.7431
30/12/18 2.58	64.03849	-21.40854	2.0000
30/12/18 3.00	64.03850	-21.40558	2.3248
30/12/18 3.00	64.03850	-21.40558	2.2441
30/12/18 3.01	63.97248	-21.32445	6.5856
30/12/18 3.01	63.97385	-21.33111	6.7102
30/12/18 3.02	64.04209	-21.40563	2.2587
30/12/18 3.04	64.04082	-21.41034	1.7401
30/12/18 3.06	63.97645	-21.32658	6.5077
30/12/18 3.06	63.96250	-21.34691	6.6099
30/12/18 3.08	63.95971	-21.33418	6.4000
30/12/18 3.11	63.96446	-21.16454	8.6253
30/12/18 3.15	64.00571	-21.35754	2.5898
30/12/18 3.16	63.97027	-21.32243	7.0933
30/12/18 3.17	63.95007	-21.30030	10.0758
30/12/18 3.20	64.04209	-21.40563	1.6000
30/12/18 3.20	63.99241	-21.37811	4.8744
30/12/18 3.23	63.95472	-21.31835	6.9466
30/12/18 3.27	63.97047	-21.33924	6.0000
30/12/18 3.30	63.97377	-21.35163	6.5990
30/12/18 3.31	63.97485	-21.32969	6.7791
30/12/18 3.33	63.96328	-21.34381	5.7447
30/12/18 3.36	63.97617	-21.31129	7.4879
30/12/18 3.39	63.96717	-21.34407	4.2768
30/12/18 3.40	63.96763	-21.35057	6.1730
30/12/18 3.41	63.96868	-21.32744	5.6555
30/12/18 3.41	63.96921	-21.30990	4.5082
30/12/18 3.46	63.97235	-21.33406	4.2185
30/12/18 3.50	63.97414	-21.30017	6.8000
30/12/18 3.51	63.95959	-21.29174	3.7359
30/12/18 3.54	63.96051	-21.33615	5.9950
30/12/18 3.55	63.97333	-21.34092	5.6804
30/12/18 4.04	63.97324	-21.33501	6.6531
30/12/18 4.14	63.97333	-21.33563	6.1548
30/12/18 4.20	63.96954	-21.35548	6.6815
30/12/18 4.23	63.96894	-21.31864	6.3884

30/12/18 4.29	63.95818	-21.34085	5.2061
30/12/18 4.34	63.95971	-21.33390	6.2215
30/12/18 4.35	63.98180	-21.33266	8.5362
30/12/18 4.41	63.96684	-21.32629	7.3657
30/12/18 4.56	63.96433	-21.33345	6.5924
30/12/18 5.00	63.97420	-21.33917	8.0220
30/12/18 5.02	63.95970	-21.33911	5.1107
30/12/18 5.04	63.95970	-21.33911	5.5041
30/12/18 5.05	63.96451	-21.33407	6.5839
30/12/18 5.14	63.95970	-21.33911	5.1184
30/12/18 5.17	63.96329	-21.33915	6.0000
30/12/18 5.21	63.97800	-21.31875	8.8842
30/12/18 5.22	63.96749	-21.33920	6.2042
30/12/18 5.22	63.95189	-21.32626	5.8323
30/12/18 5.28	63.97049	-21.33107	6.4000
30/12/18 5.30	63.97706	-21.32479	7.3644
30/12/18 5.37	63.96758	-21.35032	5.6000
30/12/18 6.16	63.96995	-21.30665	8.7331
30/12/18 6.26	63.95970	-21.33911	5.2863
30/12/18 6.36	63.91391	-21.37161	8.5190
30/12/18 6.37	63.96678	-21.32397	6.3117
30/12/18 6.46	63.97000	-21.33145	8.1077
30/12/18 6.47	63.96683	-21.35895	5.6000
30/12/18 6.56	63.97200	-21.32292	7.5547
30/12/18 6.56	63.97278	-21.32293	7.8962
30/12/18 7.11	63.91653	-21.36515	8.0789
30/12/18 7.14	63.96613	-21.32356	5.7093
30/12/18 7.19	63.96686	-21.34737	6.3339
30/12/18 7.49	63.95970	-21.33638	5.2079
30/12/18 9.00	63.95835	-21.32817	7.0156
30/12/18 9.25	63.96456	-21.33917	6.6966
30/12/18 9.31	63.96107	-21.37996	7.7770
30/12/18 9.32	63.96043	-21.33912	6.3963
30/12/18 9.34	63.96541	-21.39935	6.1466
30/12/18 9.55	64.07044	-21.30122	3.7392
30/12/18 10.20	63.97122	-21.34636	6.0605
30/12/18 10.30	63.96330	-21.33271	7.1154
30/12/18 10.40	63.96255	-21.38211	7.2356
30/12/18 11.36	63.95810	-21.33092	5.3804
30/12/18 11.45	63.96319	-21.37999	7.2135
30/12/18 11.52	63.96671	-21.30951	4.2166
30/12/18 11.55	63.96463	-21.40490	6.7873
30/12/18 11.56	63.98715	-21.32093	9.0520
30/12/18 11.56	63.95961	-21.37351	8.0000
30/12/18 12.09	63.96314	-21.39769	6.5658
30/12/18 12.18	63.97053	-21.33292	6.5571
30/12/18 12.23	64.02393	-21.50833	3.4317
30/12/18 12.40	63.95973	-21.32278	6.3889

30/12/18 12.41	63.96014	-21.32583	6.5117
30/12/18 12.42	63.95852	-21.34043	5.6652
30/12/18 12.43	63.95892	-21.33636	5.2872
30/12/18 12.51	64.03033	-21.33708	13.3336
30/12/18 13.06	63.95757	-21.33633	6.1266
30/12/18 13.16	63.96938	-21.32465	7.4586
30/12/18 13.24	63.96689	-21.33274	7.5257
30/12/18 14.12	63.96328	-21.34100	6.1733
30/12/18 15.58	63.96093	-21.33913	5.6136
30/12/18 16.00	63.97472	-21.32610	7.5015
30/12/18 17.00	63.97446	-21.39245	5.7770
30/12/18 17.05	63.97963	-21.32438	7.3903
30/12/18 17.15	64.03051	-21.54189	5.5351
30/12/18 18.00	63.96560	-21.32503	7.6171
30/12/18 18.23	63.96768	-21.33283	8.0112
30/12/18 19.47	63.97404	-21.31979	6.5387
30/12/18 20.26	64.10405	-21.28341	5.5859
30/12/18 20.31	63.97249	-21.34743	7.5094
30/12/18 20.45	63.97182	-21.33315	7.4991
30/12/18 20.47	64.00604	-21.36879	2.6809
30/12/18 21.11	63.96775	-21.35106	7.2000
30/12/18 21.24	63.96449	-21.33128	7.0891
30/12/18 23.37	63.96687	-21.34112	6.0941
31/12/18 5.23	63.96591	-21.32324	5.4169
31/12/18 9.16	63.96601	-21.39113	6.7843
31/12/18 10.34	63.96255	-21.34081	6.0889
31/12/18 14.01	63.96003	-21.16442	8.5812
31/12/18 14.32	63.97331	-21.33927	6.1085
31/12/18 15.17	63.96409	-21.34733	6.8536
31/12/18 15.19	64.03443	-21.37569	0.4492
31/12/18 15.51	63.96620	-21.33435	6.2032
31/12/18 17.10	63.96264	-21.31828	4.8354
31/12/18 19.31	64.01016	-21.44366	1.7087
31/12/18 19.37	64.16781	-21.33746	4.0729
31/12/18 20.15	63.96594	-21.34409	6.6759
31/12/18 22.15	63.93448	-21.37432	6.7086
1/1/19 0.06	64.04042	-21.17798	2.3171
1/1/19 0.16	63.95818	-21.33736	6.1736
1/1/19 0.26	63.96255	-21.34082	6.7394
1/1/19 5.56	63.95970	-21.33911	5.4685
1/1/19 5.58	63.95970	-21.33911	5.5143
1/1/19 6.11	64.01829	-21.42481	2.4917
1/1/19 6.22	63.96620	-21.33919	6.2406
1/1/19 7.14	63.98490	-21.30672	8.4802
1/1/19 7.44	63.96678	-21.30901	8.3728
1/1/19 10.27	63.96928	-21.32816	6.8682
1/1/19 11.19	63.95771	-21.34216	5.2000
1/1/19 11.22	63.95330	-21.33897	5.0118

1/1/19 11.36	63.95970	-21.33911	5.0623
1/1/19 11.50	64.06082	-21.40591	2.0869
1/1/19 13.08	63.97270	-21.33476	6.0603
1/1/19 15.17	63.93238	-21.92078	11.2291
1/1/19 21.41	64.05569	-21.39764	2.0871
2/1/19 2.31	63.97416	-21.33751	5.4596
2/1/19 2.49	63.96997	-21.33923	5.9911
2/1/19 3.16	64.03415	-21.62209	3.0611
2/1/19 7.51	63.96328	-21.34145	6.4066
2/1/19 10.03	63.96478	-21.97766	-1.8338
2/1/19 11.19	63.97408	-21.32819	6.1972
4/1/19 0.49	63.96733	-21.33849	6.7552
4/1/19 3.50	63.93455	-21.27083	7.0333
4/1/19 10.29	64.00565	-21.37524	2.2589
4/1/19 15.36	64.11183	-21.35738	3.6000
4/1/19 18.53	64.02170	-21.62740	6.1770
4/1/19 23.06	63.96123	-21.34234	6.1574
5/1/19 22.25	64.05647	-21.39765	1.6809
6/1/19 7.27	64.01043	-21.43790	2.3176
6/1/19 7.39	64.01410	-21.43459	2.6087
6/1/19 7.41	64.01557	-21.43798	2.5514
6/1/19 7.59	63.96172	-21.33913	6.0939
6/1/19 8.01	63.98721	-21.42114	4.4741
6/1/19 8.08	64.01032	-21.43250	2.6636
6/1/19 8.24	63.95970	-21.33911	6.1767
6/1/19 11.55	63.95609	-21.34723	6.1069
6/1/19 13.54	63.99661	-21.16784	7.1802
6/1/19 15.09	64.04207	-21.41382	2.0906
6/1/19 16.28	63.93606	-21.27189	4.6490
6/1/19 16.44	63.93271	-21.27715	4.2540
6/1/19 16.59	64.10832	-21.28345	5.2000
6/1/19 20.06	64.11058	-21.28347	5.2000
6/1/19 21.07	63.93045	-21.28348	5.8632
6/1/19 21.53	63.93108	-21.29254	6.3291
6/1/19 21.54	63.93002	-21.28254	6.6759
6/1/19 22.04	63.92675	-21.29475	6.6443
6/1/19 22.18	63.93109	-21.28769	6.3158
6/1/19 23.12	63.93108	-21.29257	5.9380
6/1/19 23.17	64.05903	-21.28121	3.1152
6/1/19 23.30	63.93220	-21.28594	6.6032
6/1/19 23.40	63.93195	-21.27715	4.1049
6/1/19 23.49	63.93260	-21.28904	5.4323
6/1/19 23.50	63.93389	-21.28169	4.0000
7/1/19 0.48	64.02048	-21.42987	-1.6000
7/1/19 0.49	63.89637	-21.95577	9.9619
7/1/19 2.11	63.92907	-21.28689	5.1036
7/1/19 2.20	63.94618	-21.29948	2.6775
7/1/19 2.52	64.03115	-21.46278	4.2541

7/1/19 3.23	64.00367	-21.48870	3.4385
7/1/19 3.40	64.01758	-21.42176	1.8351
7/1/19 4.56	64.00349	-21.37236	2.0714
7/1/19 5.29	64.06332	-21.21579	4.3206
7/1/19 15.44	63.93745	-21.34520	7.1119
7/1/19 17.20	63.94808	-21.38795	5.7501
7/1/19 18.29	63.99668	-21.32625	5.7454
7/1/19 18.31	63.95733	-21.32545	6.7947
7/1/19 19.35	63.96982	-21.55017	7.1744
7/1/19 20.31	64.05677	-21.26654	2.8000
7/1/19 21.23	63.96328	-21.34270	6.4000
7/1/19 21.58	63.97333	-21.33786	5.5865
7/1/19 22.42	63.99487	-21.37659	1.3994
7/1/19 23.33	64.10698	-21.28876	5.6000
8/1/19 0.38	64.11043	-21.35207	3.5111
8/1/19 0.40	64.10967	-21.35563	3.3381
8/1/19 2.11	63.97030	-21.40294	5.3430
8/1/19 4.19	63.92799	-21.29278	7.9193
8/1/19 4.22	64.11704	-21.26711	4.9478
8/1/19 4.29	63.99822	-20.88304	-0.0855
8/1/19 4.56	64.01175	-21.44438	1.6269
8/1/19 5.20	63.94567	-21.44495	6.4000
8/1/19 5.30	64.13315	-21.33985	2.1325
8/1/19 7.08	64.06001	-21.41409	2.0000
8/1/19 9.28	64.05969	-21.28296	3.2000
8/1/19 10.33	64.05283	-21.41398	1.6816
8/1/19 20.01	63.96980	-21.33247	5.5842
8/1/19 22.55	63.93173	-21.69416	8.6416
9/1/19 2.13	63.96639	-21.16300	7.5121
9/1/19 2.35	64.03636	-21.44649	3.4400
9/1/19 3.04	64.00677	-21.60486	3.6908
9/1/19 3.06	64.00756	-21.59790	3.5479
10/1/19 0.02	64.07199	-21.42112	3.8873
10/1/19 7.46	63.96975	-21.36523	5.5819
10/1/19 7.58	63.93808	-21.34885	6.4378
10/1/19 12.13	64.04161	-21.35152	2.7120
10/1/19 12.15	64.04160	-21.35348	2.9126
10/1/19 15.36	64.11261	-21.25852	9.1313
10/1/19 16.23	63.95915	-21.33397	7.7488
10/1/19 16.42	64.05313	-21.29290	4.5033
10/1/19 18.23	63.96986	-21.32933	6.8848
11/1/19 15.27	64.05017	-21.40131	2.3650
11/1/19 15.33	64.05202	-21.39053	1.5365
11/1/19 18.01	64.05954	-21.40948	2.7282
11/1/19 20.16	63.95019	-21.45162	1.3697
11/1/19 23.00	64.05226	-21.40269	1.7027
11/1/19 23.05	64.05146	-21.40080	1.7576
11/1/19 23.13	64.05286	-21.40392	1.7676

12/1/19 1.37	64.04207	-21.41382	2.7846
12/1/19 9.11	64.05442	-21.42324	8.2837
12/1/19 11.47	64.02058	-21.57814	5.9491
12/1/19 13.22	64.05058	-21.40576	1.0533
12/1/19 13.24	64.05288	-21.39760	1.6000
12/1/19 13.28	64.11353	-21.28204	4.8714
12/1/19 13.29	64.05289	-21.39260	0.7836
12/1/19 13.34	64.05288	-21.39904	1.6000
12/1/19 13.43	64.05221	-21.39759	1.6747
12/1/19 13.47	64.05217	-21.39494	1.6803
12/1/19 13.47	64.05289	-21.39486	1.6000
12/1/19 13.49	64.05087	-21.39757	1.8243
12/1/19 13.56	64.05058	-21.40053	1.7451
12/1/19 13.57	64.03398	-21.34493	3.1357
12/1/19 13.57	64.04928	-21.40071	1.7711
12/1/19 14.02	64.05069	-21.39439	1.5125
12/1/19 15.21	63.99910	-21.37230	1.6000
12/1/19 15.41	64.05288	-21.39760	0.8000
12/1/19 18.56	64.09606	-21.35839	4.0589
12/1/19 19.11	64.01341	-21.41795	3.6489
12/1/19 23.12	64.00486	-21.37553	1.8426
13/1/19 0.35	64.04078	-21.52927	12.7027
13/1/19 3.33	63.93689	-21.37470	3.5138
13/1/19 6.05	64.03483	-21.43483	3.0314
13/1/19 6.07	64.01397	-21.34795	2.0000
13/1/19 8.26	63.93451	-21.17046	3.7284
13/1/19 10.09	63.94809	-21.21191	7.4147
13/1/19 20.32	64.06045	-21.21215	4.4116
13/1/19 21.38	64.12496	-21.27018	3.7672
14/1/19 0.35	64.02409	-21.42174	2.0890
14/1/19 2.51	64.04699	-21.39680	4.7454
14/1/19 4.25	64.02970	-21.42659	1.1721
14/1/19 15.27	64.05286	-21.40579	2.4000
14/1/19 15.39	64.05285	-21.40890	2.7161
14/1/19 16.17	64.09308	-21.35855	4.0000
14/1/19 17.47	63.96193	-21.34084	6.4676
14/1/19 18.35	63.94508	-21.43499	6.7175
14/1/19 22.37	63.94523	-21.38294	5.4258
15/1/19 2.44	64.11997	-21.25893	3.9297
15/1/19 3.40	64.04142	-21.30074	5.5068
15/1/19 6.34	63.96563	-21.20979	6.6547
15/1/19 7.50	63.93661	-21.35872	5.8383
15/1/19 9.13	64.02759	-21.50632	1.5072
15/1/19 9.36	63.96033	-21.33912	6.2594
15/1/19 10.15	63.96234	-21.07780	7.6713
15/1/19 10.59	64.10341	-21.28154	5.4570
15/1/19 12.11	63.95543	-21.33906	5.2155
15/1/19 12.31	64.04224	-21.34830	1.4318

15/1/19 13.10	64.09377	-21.36540	4.0019
15/1/19 14.25	63.96260	-21.33915	6.0764
15/1/19 16.00	64.11873	-21.32702	6.4027
15/1/19 16.43	64.05295	-21.37302	1.6880
15/1/19 16.53	64.05295	-21.37302	2.0000
15/1/19 21.10	63.97654	-21.60605	6.0120
15/1/19 22.39	64.05538	-21.29426	4.3231
15/1/19 23.58	63.94527	-21.38132	6.7043
16/1/19 0.56	64.11866	-21.22645	3.4620
16/1/19 4.44	64.02192	-21.59388	4.2379
16/1/19 6.40	64.03631	-21.58352	5.1342
16/1/19 9.28	64.03620	-21.58105	5.7728
16/1/19 10.33	63.96029	-21.34728	5.2000
16/1/19 11.43	63.95893	-21.35362	5.3656
16/1/19 14.20	64.03236	-21.58055	5.8184
16/1/19 14.24	64.03302	-21.57744	5.7461
16/1/19 15.42	64.05093	-21.25829	2.8809
16/1/19 17.01	64.03149	-21.58090	5.8260
16/1/19 17.03	64.03073	-21.57894	5.9113
16/1/19 17.34	64.12268	-21.25112	3.5018
16/1/19 19.25	63.95966	-21.35544	5.4542
16/1/19 19.51	64.05318	-21.26650	2.8000
16/1/19 21.22	64.06752	-21.27507	3.6057
16/1/19 22.30	64.04108	-21.17939	2.8652
16/1/19 22.40	64.03581	-21.57894	6.0000
16/1/19 23.13	63.94688	-21.39286	5.5532
16/1/19 23.35	64.03229	-21.58063	5.7555
16/1/19 23.37	64.03137	-21.58420	5.8425
16/1/19 23.51	64.03071	-21.58423	5.6733
17/1/19 0.25	64.03312	-21.58328	5.8199
17/1/19 0.28	64.03132	-21.58284	5.6739
17/1/19 2.55	64.03211	-21.58666	5.9782
17/1/19 2.56	63.95899	-21.28659	5.5287
17/1/19 4.22	64.05674	-21.28293	2.8000
17/1/19 5.40	64.09604	-21.36539	4.0000
17/1/19 12.43	64.04391	-20.98891	8.4569
17/1/19 13.32	64.03322	-21.58271	5.4337
17/1/19 14.48	64.00424	-21.38055	2.0000
17/1/19 16.23	64.00718	-21.53954	3.4416
17/1/19 18.30	64.02677	-21.23021	3.4964
17/1/19 19.58	63.97753	-21.09233	8.4906
17/1/19 22.30	64.06253	-21.19465	5.2076
17/1/19 22.49	63.96776	-21.54527	7.1099
18/1/19 5.19	63.95510	-21.33905	4.7531
18/1/19 7.37	64.12723	-21.50469	5.9772
18/1/19 7.41	64.01151	-21.38972	0.8417
18/1/19 8.37	64.05391	-21.21094	4.2411
18/1/19 9.46	64.03348	-21.57786	5.2490

18/1/19 9.57	64.04968	-21.21405	3.8374
18/1/19 14.28	64.04717	-21.37889	0.9016
18/1/19 22.24	64.05836	-21.21787	4.0884
18/1/19 23.02	64.03508	-21.40369	0.4186
18/1/19 23.03	64.05431	-21.36648	6.2440
19/1/19 7.46	64.06033	-21.28296	3.2000
19/1/19 14.31	64.00994	-21.66266	8.4120
19/1/19 15.43	64.03160	-21.56446	5.4330
19/1/19 20.55	64.05965	-21.28825	3.2000
19/1/19 21.17	64.07765	-21.33524	4.4056
20/1/19 0.45	64.10409	-21.28163	5.2000
20/1/19 0.58	64.02070	-21.36844	0.2083
20/1/19 2.00	64.01346	-21.37386	2.6241
20/1/19 4.46	64.03896	-21.17628	2.4000
20/1/19 5.36	63.94876	-21.06935	9.6798
20/1/19 7.44	63.95397	-21.33038	6.9864
20/1/19 12.09	63.97022	-21.43353	3.8251
20/1/19 23.47	64.10685	-21.34911	4.2538
21/1/19 4.36	63.94238	-21.40238	7.0283
21/1/19 6.07	64.06402	-21.22417	4.7969
21/1/19 6.45	64.05541	-21.26340	2.9524
21/1/19 11.16	64.01344	-21.37887	2.7117
21/1/19 11.16	64.01344	-21.37887	2.7121
21/1/19 12.31	64.00836	-21.37612	3.0558
21/1/19 12.53	64.00989	-21.36426	2.5461
21/1/19 14.28	63.95546	-21.32772	6.9734
21/1/19 15.23	64.05321	-21.25197	3.5336
21/1/19 16.59	64.06044	-21.21740	4.5523
21/1/19 17.00	64.06044	-21.21740	4.6101
21/1/19 18.43	63.97245	-21.62293	6.8000
21/1/19 18.48	63.97034	-21.62332	7.0436
21/1/19 20.14	64.01687	-21.43800	2.0000
21/1/19 20.14	64.01687	-21.43800	2.0000
21/1/19 20.57	64.00563	-21.38199	1.7398
21/1/19 22.42	64.06033	-21.28296	3.2000
21/1/19 23.35	64.06263	-21.20102	4.6217
22/1/19 0.17	64.06737	-21.34514	1.9131
22/1/19 1.51	63.96610	-21.35722	5.9168
22/1/19 2.19	64.03076	-21.58693	5.8360
22/1/19 3.14	64.11838	-21.23798	-0.0458
22/1/19 3.31	64.06352	-21.21542	4.5777
22/1/19 3.32	64.01187	-21.47482	13.2864
22/1/19 6.16	63.95223	-21.08875	9.3139
22/1/19 10.29	64.03302	-21.58394	5.9103
22/1/19 10.33	64.11112	-21.35222	4.1782
22/1/19 10.35	64.11042	-21.35737	3.5294
22/1/19 10.36	64.11042	-21.35737	3.5307
22/1/19 10.41	64.03632	-21.57933	5.5430

22/1/19 17.36	63.95006	-21.43526	4.6936
23/1/19 0.41	64.05320	-21.25477	3.0550
23/1/19 7.15	64.07095	-21.34866	1.7732
23/1/19 9.06	63.96591	-21.14619	8.9441
23/1/19 12.14	64.05319	-21.26293	2.8000
23/1/19 12.32	64.11562	-21.24963	4.7846
23/1/19 12.58	63.91544	-21.20701	4.8676
23/1/19 15.11	63.97273	-21.33927	6.3153
23/1/19 18.58	64.05318	-21.26650	3.2000
23/1/19 19.05	64.05317	-21.26985	2.8780
23/1/19 19.10	64.04967	-21.21731	3.7701
23/1/19 19.13	63.94975	-21.34799	5.6409
23/1/19 19.22	64.04568	-21.40569	2.8000
23/1/19 19.25	64.07168	-21.34523	4.0000
23/1/19 19.36	63.94890	-21.35146	5.9100
23/1/19 22.09	64.05970	-21.27860	2.6126
23/1/19 23.28	64.05954	-21.27773	2.7437
23/1/19 23.30	64.06033	-21.28296	2.4000
23/1/19 23.31	64.08342	-21.32716	3.4584
24/1/19 1.56	64.10917	-21.28487	5.2000
24/1/19 12.36	63.96568	-21.15224	9.4620
24/1/19 13.42	63.96762	-21.39383	6.5850
24/1/19 14.33	63.94302	-21.44478	6.8000
24/1/19 16.41	64.00987	-21.37387	2.6377
24/1/19 16.42	64.00913	-21.42754	2.5469
24/1/19 16.46	64.00973	-21.42457	2.8461
24/1/19 20.51	63.94461	-21.43984	7.0044
24/1/19 23.05	64.06033	-21.28296	3.1300
25/1/19 0.44	64.02048	-21.42987	2.4886
25/1/19 1.59	63.95324	-21.43419	4.1470
25/1/19 3.09	64.04860	-21.24026	10.1979
25/1/19 3.11	63.95639	-21.43818	6.1670
25/1/19 3.25	64.12500	-21.25076	3.9284
25/1/19 5.56	64.00688	-21.37240	2.4341
25/1/19 6.05	64.05652	-21.38059	2.2163
25/1/19 6.55	63.94367	-21.43510	6.5476
25/1/19 7.37	64.00267	-21.38052	2.2211
25/1/19 16.38	63.93003	-21.46302	4.3453
25/1/19 18.43	63.95295	-21.17223	8.0656
25/1/19 20.05	64.02188	-21.42815	3.0365
25/1/19 23.51	64.05356	-21.41399	2.0000
26/1/19 2.56	63.97398	-21.33876	11.7511
26/1/19 3.33	63.89690	-21.92829	7.2494
26/1/19 3.53	63.91800	-21.38738	6.2392
26/1/19 4.01	63.91862	-21.38568	6.1647
26/1/19 4.06	64.05962	-21.27935	3.1296
26/1/19 4.07	64.05819	-21.27650	3.2000
26/1/19 7.27	64.05645	-21.40584	3.2000

26/1/19 8.26	63.86167	-21.44381	9.5714
26/1/19 9.18	64.06033	-21.28296	3.6000
26/1/19 10.55	63.99642	-21.69301	6.2210
26/1/19 13.41	64.07708	-21.48477	9.1219
26/1/19 14.17	64.00697	-21.35901	3.0386
26/1/19 14.18	64.01248	-21.35844	2.0731
26/1/19 14.20	64.01062	-21.36262	2.3153
26/1/19 15.45	63.94891	-21.34533	5.2456
26/1/19 16.38	64.04673	-21.28282	4.0000
26/1/19 19.32	63.93372	-21.44982	10.3867
26/1/19 21.43	64.11058	-21.28524	5.2716
26/1/19 22.02	63.84637	-21.30051	6.2012
26/1/19 23.18	64.11059	-21.28034	5.3525
27/1/19 3.40	64.01053	-21.37097	1.6000
27/1/19 4.10	64.05316	-21.27470	3.6000
27/1/19 4.40	64.06363	-21.40595	2.0000
27/1/19 4.42	64.06371	-21.44667	3.7344
27/1/19 7.21	64.01430	-21.43503	2.0301
27/1/19 7.47	64.10994	-21.28194	5.5127
27/1/19 9.58	64.05752	-21.29113	2.4884
27/1/19 10.01	64.02037	-20.90721	8.3344
27/1/19 10.05	64.03301	-21.10000	3.1848
27/1/19 11.57	63.95184	-21.33721	5.6762
27/1/19 12.37	63.98187	-21.83418	6.8845
27/1/19 14.26	64.04459	-20.93704	10.5255
27/1/19 14.41	64.00861	-21.36273	1.8462
27/1/19 15.37	64.05314	-21.28764	3.7576
27/1/19 15.37	64.05315	-21.28448	3.4282
27/1/19 17.59	64.05247	-21.25830	3.0586
27/1/19 18.01	64.05321	-21.25195	3.2000
27/1/19 18.53	63.93770	-21.16749	8.1810
27/1/19 19.32	63.95029	-21.30862	7.0717
27/1/19 22.35	64.10926	-21.28346	5.4290
28/1/19 0.04	64.06100	-21.58636	2.8964
28/1/19 1.35	64.02052	-21.41702	2.1483
28/1/19 2.10	64.03978	-21.41280	3.3961
28/1/19 2.24	63.98874	-21.95548	9.3876
28/1/19 2.30	64.06004	-21.40412	2.0000
28/1/19 8.15	63.94443	-21.27072	8.2209
28/1/19 8.52	64.01746	-21.40703	8.1683
28/1/19 9.51	63.93762	-21.19399	7.1634
28/1/19 12.01	64.06003	-21.40729	2.0000
28/1/19 12.13	64.07207	-21.33067	5.6201
28/1/19 13.44	64.04236	-21.27037	3.6488
28/1/19 16.27	64.11058	-21.28347	5.2684
28/1/19 20.02	63.96555	-21.23769	5.6624
28/1/19 21.17	64.04253	-21.18784	2.6193
28/1/19 21.25	64.04317	-21.18307	2.0757

28/1/19 22.11	64.05970	-21.29115	2.4680
28/1/19 22.30	64.06032	-21.28453	2.7235
28/1/19 23.34	64.10073	-21.31864	-1.0636
28/1/19 23.37	63.95536	-21.29989	6.8100
29/1/19 0.19	64.06032	-21.28615	2.6447
29/1/19 0.19	64.05827	-21.28812	2.9472
29/1/19 0.20	64.06031	-21.29116	2.6439
29/1/19 0.21	64.05958	-21.29115	2.4817
29/1/19 0.22	64.06851	-21.29652	3.0414
29/1/19 0.37	64.06031	-21.29116	2.8000
29/1/19 2.00	64.06032	-21.28588	2.8000
29/1/19 2.15	64.05955	-21.28473	2.5443
29/1/19 2.16	64.06033	-21.28296	2.2366
29/1/19 2.24	64.06031	-21.28972	2.4000
29/1/19 2.29	64.06088	-21.28627	2.7382
29/1/19 2.33	64.05753	-21.28293	3.3553
29/1/19 2.34	64.06032	-21.28463	2.4701
29/1/19 2.35	64.06031	-21.29116	2.4000
29/1/19 2.38	64.06033	-21.28296	2.8000
29/1/19 2.50	64.05675	-21.27822	3.2765
29/1/19 2.51	64.06031	-21.29116	2.8000
29/1/19 2.54	64.06033	-21.28296	2.4802
29/1/19 2.55	64.06032	-21.28622	2.4000
29/1/19 2.56	64.05898	-21.28808	2.6992
29/1/19 2.57	64.06033	-21.28296	2.4000
29/1/19 3.01	64.06033	-21.28296	2.8000
29/1/19 3.01	64.06033	-21.28296	2.8000
29/1/19 3.04	64.05901	-21.28461	2.7748
29/1/19 3.38	63.94308	-21.41685	4.4692
29/1/19 4.31	64.06033	-21.28296	2.8000
29/1/19 4.37	64.05483	-21.41401	2.0000
29/1/19 5.45	64.06353	-21.28709	4.2495
29/1/19 6.14	64.05902	-21.28295	2.5456
29/1/19 6.45	64.05750	-21.28937	2.7140
29/1/19 10.48	64.02048	-21.42987	2.7323
29/1/19 12.49	64.05647	-21.39765	1.6000
29/1/19 12.50	64.05647	-21.39765	1.6000
29/1/19 12.50	64.05647	-21.39765	1.5210
29/1/19 12.53	64.00493	-21.37709	2.4614
29/1/19 14.52	64.05348	-21.40082	2.0904
29/1/19 14.54	64.05567	-21.40739	1.7482
29/1/19 15.52	64.05362	-21.40232	1.6834
29/1/19 16.26	64.09663	-21.36539	3.2658
29/1/19 17.46	64.11961	-21.02212	10.9285
29/1/19 19.16	64.05645	-21.40584	1.9071
29/1/19 19.33	63.94590	-21.38466	5.0581
29/1/19 21.49	64.06752	-21.27484	3.6000
29/1/19 21.54	64.06752	-21.27653	3.6106

29/1/19 22.27	64.06752	-21.27484	3.5156
29/1/19 22.51	64.06752	-21.27484	3.1175
30/1/19 2.06	64.01343	-21.38369	2.8000
30/1/19 3.21	64.06562	-21.18445	4.0000
30/1/19 6.40	64.11977	-21.36427	4.8696
30/1/19 9.23	64.04047	-21.14344	1.5128
30/1/19 10.32	63.95641	-21.16760	8.4000
30/1/19 14.33	64.02288	-21.41354	2.2761
30/1/19 15.15	64.05709	-21.53057	7.2048
30/1/19 15.18	64.05723	-21.40550	1.9825
30/1/19 15.37	64.04965	-21.23370	2.3101
30/1/19 23.21	64.04936	-21.37297	2.0000
31/1/19 1.42	63.84464	-21.13180	13.4198
31/1/19 1.45	63.79265	-21.04738	16.4079
31/1/19 2.21	64.05319	-21.25831	2.8000
31/1/19 2.30	63.96773	-21.57085	6.0814
31/1/19 6.21	64.06004	-21.40589	2.0000
31/1/19 6.46	64.04927	-21.40574	1.9118
31/1/19 7.16	64.06363	-21.40595	2.0000

Appendix B. Relative magnitude

Table B.1 – Relative magnitude of Cluster 1

Date	Longitude	Latitude	Depth (km)	Relative Magnitude
23/12/18 0.00	-21.33914	63.97700	6.627	-0.22
29/12/18 21.33	-21.32932	63.95254	5.276	0.19
30/12/18 2.56	-21.32625	63.97262	7.047	4.58
30/12/18 2.57	-21.33707	63.96252	6.743	2.02
30/12/18 3.01	-21.32445	63.97248	6.586	1.00
30/12/18 3.01	-21.33111	63.97385	6.710	1.04
30/12/18 3.06	-21.32658	63.97645	6.508	0.91
30/12/18 3.06	-21.34691	63.96250	6.610	0.73
30/12/18 3.08	-21.33418	63.95971	6.400	0.17
30/12/18 3.16	-21.32243	63.97027	7.093	0.56
30/12/18 3.23	-21.31835	63.95472	6.947	0.49
30/12/18 3.27	-21.33924	63.97047	6.000	1.33
30/12/18 3.30	-21.35163	63.97377	6.599	0.63
30/12/18 3.31	-21.32969	63.97485	6.779	0.48
30/12/18 3.33	-21.34381	63.96328	5.745	0.16
30/12/18 3.36	-21.31129	63.97617	7.488	0.24
30/12/18 3.40	-21.35057	63.96763	6.173	0.79
30/12/18 3.41	-21.32744	63.96868	5.655	0.53
30/12/18 3.50	-21.30017	63.97414	6.800	0.20
30/12/18 3.54	-21.33615	63.96051	5.995	0.28
30/12/18 3.55	-21.34092	63.97333	5.680	0.43
30/12/18 4.04	-21.33501	63.97324	6.653	1.18
30/12/18 4.14	-21.33563	63.97333	6.155	0.47
30/12/18 4.20	-21.35548	63.96954	6.682	0.31
30/12/18 4.23	-21.31864	63.96894	6.388	0.45
30/12/18 4.29	-21.34085	63.95818	5.206	0.23
30/12/18 4.34	-21.33390	63.95971	6.222	0.40
30/12/18 4.41	-21.32629	63.96684	7.366	0.21
30/12/18 4.56	-21.33345	63.96433	6.592	0.51
30/12/18 5.00	-21.33917	63.97420	8.022	0.52
30/12/18 5.02	-21.33911	63.95970	5.111	1.60
30/12/18 5.04	-21.33911	63.95970	5.504	1.15
30/12/18 5.05	-21.33407	63.96451	6.584	0.88
30/12/18 5.14	-21.33911	63.95970	5.118	0.65
30/12/18 5.17	-21.33915	63.96329	6.000	0.26
30/12/18 5.22	-21.33920	63.96749	6.204	0.72
30/12/18 5.22	-21.32626	63.95189	5.832	0.87
30/12/18 5.28	-21.33107	63.97049	6.400	1.21
30/12/18 5.30	-21.32479	63.97706	7.364	0.90
30/12/18 5.37	-21.35032	63.96758	5.600	0.59
30/12/18 6.26	-21.33911	63.95970	5.286	1.26

30/12/18 6.37	-21.32397	63.96678	6.312	0.40
30/12/18 6.46	-21.33145	63.97000	8.108	0.55
30/12/18 6.47	-21.35895	63.96683	5.600	0.33
30/12/18 6.56	-21.32292	63.97200	7.555	0.42
30/12/18 6.56	-21.32293	63.97278	7.896	0.41
30/12/18 7.14	-21.32356	63.96613	5.709	0.23
30/12/18 7.19	-21.34737	63.96686	6.334	1.01
30/12/18 7.49	-21.33638	63.95970	5.208	1.35
30/12/18 9.00	-21.32817	63.95835	7.016	1.99
30/12/18 9.25	-21.33917	63.96456	6.697	1.15
30/12/18 9.32	-21.33912	63.96043	6.396	0.58
30/12/18 10.20	-21.34636	63.97122	6.060	1.06
30/12/18 10.30	-21.33271	63.96330	7.115	1.22
30/12/18 11.36	-21.33092	63.95810	5.380	1.40
30/12/18 12.18	-21.33292	63.97053	6.557	0.10
30/12/18 12.40	-21.32278	63.95973	6.389	2.62
30/12/18 12.41	-21.32583	63.96014	6.512	0.86
30/12/18 12.42	-21.34043	63.95852	5.665	0.87
30/12/18 12.43	-21.33636	63.95892	5.287	1.59
30/12/18 13.06	-21.33633	63.95757	6.127	1.01
30/12/18 13.16	-21.32465	63.96938	7.459	0.25
30/12/18 13.24	-21.33274	63.96689	7.526	0.49
30/12/18 14.12	-21.34100	63.96328	6.173	0.83
30/12/18 15.58	-21.33913	63.96093	5.614	0.48
30/12/18 16.00	-21.32610	63.97472	7.502	0.54
30/12/18 17.05	-21.32438	63.97963	7.390	0.37
30/12/18 18.00	-21.32503	63.96560	7.617	0.29
30/12/18 18.23	-21.33283	63.96768	8.011	0.38
30/12/18 19.47	-21.31979	63.97404	6.539	0.13
30/12/18 20.31	-21.34743	63.97249	7.509	0.47
30/12/18 20.45	-21.33315	63.97182	7.499	0.53
30/12/18 21.11	-21.35106	63.96775	7.200	1.14
30/12/18 21.24	-21.33128	63.96449	7.089	0.54
30/12/18 23.37	-21.34112	63.96687	6.094	1.21
31/12/18 5.23	-21.32324	63.96591	5.417	0.88
31/12/18 10.34	-21.34081	63.96255	6.089	0.81
31/12/18 14.32	-21.33927	63.97331	6.108	0.20
31/12/18 15.17	-21.34733	63.96409	6.854	0.46
31/12/18 15.51	-21.33435	63.96620	6.203	0.28
31/12/18 17.10	-21.31828	63.96264	4.835	0.10
31/12/18 20.15	-21.34409	63.96594	6.676	1.03
1/1/19 0.16	-21.33736	63.95818	6.174	0.40
1/1/19 0.26	-21.34082	63.96255	6.739	0.23
1/1/19 5.56	-21.33911	63.95970	5.468	1.90
1/1/19 5.58	-21.33911	63.95970	5.514	0.73
1/1/19 6.22	-21.33919	63.96620	6.241	0.47
1/1/19 10.27	-21.32816	63.96928	6.868	0.67
1/1/19 11.19	-21.34216	63.95771	5.200	0.30
1/1/19 11.22	-21.33897	63.95330	5.012	0.37

1/1/19 11.36	-21.33911	63.95970	5.062	0.87
1/1/19 13.08	-21.33476	63.97270	6.060	1.09
2/1/19 2.31	-21.33751	63.97416	5.460	0.10
2/1/19 2.49	-21.33923	63.96997	5.991	0.69
2/1/19 7.51	-21.34145	63.96328	6.407	1.21
2/1/19 11.19	-21.32819	63.97408	6.197	0.66
4/1/19 0.49	-21.33849	63.96733	6.755	1.81
4/1/19 23.06	-21.34234	63.96123	6.157	1.08
6/1/19 7.59	-21.33913	63.96172	6.094	1.09
6/1/19 8.24	-21.33911	63.95970	6.177	0.64
6/1/19 11.55	-21.34723	63.95609	6.107	0.43
7/1/19 18.31	-21.32545	63.95733	6.795	0.31
7/1/19 21.23	-21.34270	63.96328	6.400	0.46
7/1/19 21.58	-21.33786	63.97333	5.587	-0.02
8/1/19 20.01	-21.33247	63.96980	5.584	0.40
10/1/19 7.46	-21.36523	63.96975	5.582	0.70
10/1/19 16.23	-21.33397	63.95915	7.749	0.38
10/1/19 18.23	-21.32933	63.96986	6.885	0.11
14/1/19 17.47	-21.34084	63.96193	6.468	0.16
15/1/19 9.36	-21.33912	63.96033	6.259	0.66
15/1/19 12.11	-21.33906	63.95543	5.215	0.50
15/1/19 14.25	-21.33915	63.96260	6.076	0.53
16/1/19 10.33	-21.34728	63.96029	5.200	1.15
16/1/19 11.43	-21.35362	63.95893	5.366	0.45
16/1/19 19.25	-21.35544	63.95966	5.454	0.36
18/1/19 5.19	-21.33905	63.95510	4.753	0.12
20/1/19 7.44	-21.33038	63.95397	6.986	0.24
21/1/19 14.28	-21.32772	63.95546	6.973	0.93
22/1/19 1.51	-21.35722	63.96610	5.917	0.19
23/1/19 15.11	-21.33927	63.97273	6.315	0.67
23/1/19 19.13	-21.34799	63.94975	5.641	1.39
23/1/19 19.36	-21.35146	63.94890	5.910	1.41
26/1/19 15.45	-21.34533	63.94891	5.246	0.09
27/1/19 11.57	-21.33721	63.95184	5.676	0.62

Table B.2 – Relative magnitude of Cluster 2

Date	Longitude	Latitude	Depth (km)	Relative Magnitude
22/12/18 17.51	-21.26795	64.06689	3.536	0.97
22/12/18 17.52	-21.27329	64.06753	3.600	-0.35
22/12/18 21.19	-21.28293	64.05674	3.130	-0.26
22/12/18 21.40	-21.28472	64.05673	3.113	-0.70
23/12/18 8.01	-21.25972	64.05319	2.800	-0.25
25/12/18 4.36	-21.26650	64.05318	3.600	-0.44
26/12/18 14.06	-21.28294	64.05829	3.276	-0.35
28/12/18 10.39	-21.28293	64.05674	2.800	-0.26
28/12/18 14.49	-21.27822	64.05827	2.711	-0.40

28/12/18 15.28	-21.29000	64.06154	2.194	-0.50
29/12/18 3.19	-21.25588	64.05066	3.571	0.89
29/12/18 10.54	-21.26025	64.05111	3.600	-0.29
29/12/18 17.18	-21.29219	64.05985	2.800	-0.25
6/1/19 23.17	-21.28121	64.05903	3.115	-0.51
7/1/19 20.31	-21.26654	64.05677	2.800	-0.43
8/1/19 9.28	-21.28296	64.05969	3.200	-0.31
10/1/19 16.42	-21.29290	64.05313	4.503	-0.33
15/1/19 22.39	-21.29426	64.05538	4.323	-0.52
16/1/19 15.42	-21.25829	64.05093	2.881	-0.17
16/1/19 19.51	-21.26650	64.05318	2.800	-0.61
16/1/19 21.22	-21.27507	64.06752	3.606	-0.51
17/1/19 4.22	-21.28293	64.05674	2.800	-0.57
19/1/19 7.46	-21.28296	64.06033	3.200	0.57
19/1/19 20.55	-21.28825	64.05965	3.200	-0.09
21/1/19 6.45	-21.26340	64.05541	2.952	-0.34
21/1/19 15.23	-21.25197	64.05321	3.534	0.80
21/1/19 22.42	-21.28296	64.06033	3.200	-0.35
23/1/19 0.41	-21.25477	64.05320	3.055	-0.35
23/1/19 12.14	-21.26293	64.05319	2.800	-0.50
23/1/19 18.58	-21.26650	64.05318	3.200	0.42
23/1/19 19.05	-21.26985	64.05317	2.878	-0.66
23/1/19 22.09	-21.27860	64.05970	2.613	-0.51
23/1/19 23.28	-21.27773	64.05954	2.744	-0.67
23/1/19 23.30	-21.28296	64.06033	2.400	-0.23
24/1/19 23.05	-21.28296	64.06033	3.130	0.11
26/1/19 4.06	-21.27935	64.05962	3.130	0.02
26/1/19 4.07	-21.27650	64.05819	3.200	0.30
26/1/19 9.18	-21.28296	64.06033	3.600	-0.59
26/1/19 16.38	-21.28282	64.04673	4.000	-0.71
27/1/19 4.10	-21.27470	64.05316	3.600	0.01
27/1/19 9.58	-21.29113	64.05752	2.488	-0.88
27/1/19 15.37	-21.28764	64.05314	3.758	-0.51
27/1/19 15.37	-21.28448	64.05315	3.428	-0.50
27/1/19 17.59	-21.25830	64.05247	3.059	0.22
27/1/19 18.01	-21.25195	64.05321	3.200	-0.13
28/1/19 22.11	-21.29115	64.05970	2.468	-0.37
28/1/19 22.30	-21.28453	64.06032	2.724	-0.41
29/1/19 0.19	-21.28615	64.06032	2.645	0.23
29/1/19 0.19	-21.28812	64.05827	2.947	-0.32
29/1/19 0.20	-21.29116	64.06031	2.644	-0.06
29/1/19 0.21	-21.29115	64.05958	2.482	-0.16
29/1/19 0.22	-21.29652	64.06851	3.041	-0.45
29/1/19 0.37	-21.29116	64.06031	2.800	1.14
29/1/19 2.00	-21.28588	64.06032	2.800	0.12
29/1/19 2.15	-21.28473	64.05955	2.544	-0.45
29/1/19 2.16	-21.28296	64.06033	2.237	-0.47
29/1/19 2.24	-21.28972	64.06031	2.400	-0.37
29/1/19 2.29	-21.28627	64.06088	2.738	2.20

29/1/19 2.33	-21.28293	64.05753	3.355	-0.38
29/1/19 2.34	-21.28463	64.06032	2.470	0.03
29/1/19 2.35	-21.29116	64.06031	2.400	-0.36
29/1/19 2.38	-21.28296	64.06033	2.800	-0.25
29/1/19 2.50	-21.27822	64.05675	3.277	-0.47
29/1/19 2.51	-21.29116	64.06031	2.800	0.12
29/1/19 2.54	-21.28296	64.06033	2.480	-0.28
29/1/19 2.55	-21.28622	64.06032	2.400	0.09
29/1/19 2.56	-21.28808	64.05898	2.699	-0.34
29/1/19 2.57	-21.28296	64.06033	2.400	-0.49
29/1/19 3.01	-21.28296	64.06033	2.800	-0.43
29/1/19 3.01	-21.28296	64.06033	2.800	-0.26
29/1/19 3.04	-21.28461	64.05901	2.775	-0.46
29/1/19 4.31	-21.28296	64.06033	2.800	-0.44
29/1/19 5.45	-21.28709	64.06353	4.249	-0.51
29/1/19 6.14	-21.28295	64.05902	2.546	-0.55
29/1/19 6.45	-21.28937	64.05750	2.714	-0.55
29/1/19 21.49	-21.27484	64.06752	3.600	-0.16
29/1/19 21.54	-21.27653	64.06752	3.611	-0.54
29/1/19 22.27	-21.27484	64.06752	3.516	-0.57
29/1/19 22.51	-21.27484	64.06752	3.117	-0.58
31/1/19 2.21	-21.25831	64.05319	2.800	-0.01

Table B.3 – Relative magnitude of Cluster 3

Date	Longitude	Latitude	Depth (km)	Relative Magnitude
22/12/18 8.18	-21.39755	64.04929	1.855	-0.38
23/12/18 8.28	-21.40585	64.05705	2.072	-0.23
23/12/18 8.32	-21.40584	64.05645	2.000	-0.34
23/12/18 8.37	-21.40584	64.05645	2.000	-0.08
23/12/18 17.28	-21.40758	64.04567	2.222	0.62
23/12/18 17.37	-21.41666	64.04206	2.069	-0.26
23/12/18 18.47	-21.40709	64.04329	2.000	0.70
23/12/18 18.51	-21.41382	64.04207	2.314	-0.07
23/12/18 18.52	-21.40567	64.04486	2.225	1.05
24/12/18 17.08	-21.39892	64.05288	1.357	-0.21
24/12/18 20.03	-21.42264	64.03815	2.000	-0.22
27/12/18 5.07	-21.40579	64.05286	1.745	-0.28
28/12/18 11.23	-21.39256	64.05289	2.084	0.01
30/12/18 2.58	-21.40854	64.03849	2.000	0.84
30/12/18 3.00	-21.40558	64.03850	2.325	1.55
30/12/18 3.00	-21.40558	64.03850	2.244	1.88
30/12/18 3.02	-21.40563	64.04209	2.259	0.56
30/12/18 3.04	-21.41034	64.04082	1.740	0.43
30/12/18 3.20	-21.40563	64.04209	1.600	0.31
1/1/19 11.50	-21.40591	64.06082	2.087	-0.24
1/1/19 21.41	-21.39764	64.05569	2.087	0.88

5/1/19 22.25	-21.39765	64.05647	1.681	0.27
6/1/19 15.09	-21.41382	64.04207	2.091	-0.11
8/1/19 7.08	-21.41409	64.06001	2.000	-0.14
8/1/19 10.33	-21.41398	64.05283	1.682	0.06
11/1/19 15.27	-21.40131	64.05017	2.365	0.09
11/1/19 15.33	-21.39053	64.05202	1.537	0.42
11/1/19 18.01	-21.40948	64.05954	2.728	0.14
11/1/19 23.00	-21.40269	64.05226	1.703	0.19
11/1/19 23.05	-21.40080	64.05146	1.758	0.50
11/1/19 23.13	-21.40392	64.05286	1.768	0.44
12/1/19 1.37	-21.41382	64.04207	2.785	0.26
12/1/19 13.22	-21.40576	64.05058	1.053	-0.03
12/1/19 13.24	-21.39760	64.05288	1.600	0.57
12/1/19 13.29	-21.39260	64.05289	0.784	0.15
12/1/19 13.34	-21.39904	64.05288	1.600	0.38
12/1/19 13.43	-21.39759	64.05221	1.675	0.25
12/1/19 13.47	-21.39494	64.05217	1.680	1.42
12/1/19 13.47	-21.39486	64.05289	1.600	1.55
12/1/19 13.49	-21.39757	64.05087	1.824	0.53
12/1/19 13.56	-21.40053	64.05058	1.745	0.00
12/1/19 13.57	-21.40071	64.04928	1.771	0.03
12/1/19 14.02	-21.39439	64.05069	1.512	0.19
12/1/19 15.41	-21.39760	64.05288	0.800	-0.26
14/1/19 15.27	-21.40579	64.05286	2.400	1.19
14/1/19 15.39	-21.40890	64.05285	2.716	0.01
15/1/19 16.43	-21.37302	64.05295	1.688	0.01
15/1/19 16.53	-21.37302	64.05295	2.000	0.12
18/1/19 14.28	-21.37889	64.04717	0.902	0.00
23/1/19 19.22	-21.40569	64.04568	2.800	-0.22
25/1/19 6.05	-21.38059	64.05652	2.216	-0.33
25/1/19 23.51	-21.41399	64.05356	2.000	-0.26
26/1/19 7.27	-21.40584	64.05645	3.200	-0.32
27/1/19 4.40	-21.40595	64.06363	2.000	-0.25
28/1/19 2.10	-21.41280	64.03978	3.396	-0.30
28/1/19 2.30	-21.40412	64.06004	2.000	-0.33
28/1/19 12.01	-21.40729	64.06003	2.000	-0.08
29/1/19 4.37	-21.41401	64.05483	2.000	-0.02
29/1/19 12.49	-21.39765	64.05647	1.600	0.05
29/1/19 12.50	-21.39765	64.05647	1.600	-0.05
29/1/19 12.50	-21.39765	64.05647	1.521	-0.03
29/1/19 14.52	-21.40082	64.05348	2.090	-0.13
29/1/19 14.54	-21.40739	64.05567	1.748	-0.10
29/1/19 15.52	-21.40232	64.05362	1.683	-0.06
29/1/19 19.16	-21.40584	64.05645	1.907	1.70
30/1/19 15.18	-21.40550	64.05723	1.983	-0.29
31/1/19 6.21	-21.40589	64.06004	2.000	-0.08
31/1/19 6.46	-21.40574	64.04927	1.912	-0.13
31/1/19 7.16	-21.40595	64.06363	2.000	-0.24

Table B.4 – Relative magnitude of Cluster 4

Date	Longitude	Latitude	Depth (km)	Relative Magnitude
23/12/18 4.30	-21.37387	64.01642	2.395	-0.46
26/12/18 12.35	-21.37093	64.00338	2.258	0.56
28/12/18 4.01	-21.38073	64.01766	2.144	-0.11
28/12/18 7.07	-21.37886	64.01484	2.645	-0.09
29/12/18 19.08	-21.37241	64.00717	2.243	0.07
30/12/18 3.15	-21.35754	64.00571	2.590	0.53
30/12/18 20.47	-21.36879	64.00604	2.681	-0.01
4/1/19 10.29	-21.37524	64.00565	2.259	0.13
7/1/19 4.56	-21.37236	64.00349	2.071	0.22
12/1/19 15.21	-21.37230	63.99910	1.600	0.07
12/1/19 23.12	-21.37553	64.00486	1.843	-0.26
13/1/19 6.07	-21.34795	64.01397	2.000	0.29
17/1/19 14.48	-21.38055	64.00424	2.000	0.03
20/1/19 2.00	-21.37386	64.01346	2.624	-0.01
21/1/19 11.16	-21.37887	64.01344	2.712	0.10
21/1/19 11.16	-21.37887	64.01344	2.712	0.11
21/1/19 12.31	-21.37612	64.00836	3.056	0.02
21/1/19 12.53	-21.36426	64.00989	2.546	0.27
24/1/19 16.41	-21.37387	64.00987	2.638	-0.09
25/1/19 5.56	-21.37240	64.00688	2.434	1.30
25/1/19 7.37	-21.38052	64.00267	2.221	0.90
26/1/19 14.17	-21.35901	64.00697	3.039	-0.08
26/1/19 14.18	-21.35844	64.01248	2.073	0.00
26/1/19 14.20	-21.36262	64.01062	2.315	-0.04
27/1/19 3.40	-21.37097	64.01053	1.600	0.00
27/1/19 14.41	-21.36273	64.00861	1.846	-0.10
29/1/19 12.53	-21.37709	64.00493	2.461	0.04
30/1/19 2.06	-21.38369	64.01343	2.800	-0.43

Table B.5 – Relative magnitude of Cluster 5

Date	Longitude	Latitude	Depth (km)	Relative Magnitude
25/12/18 2.51	-21.42163	64.01692	2.800	0.30
26/12/18 6.05	-21.42168	64.01966	1.160	0.39
26/12/18 6.17	-21.42926	64.01858	1.738	0.54
26/12/18 7.22	-21.40490	64.02287	1.511	0.49
26/12/18 7.22	-21.41573	64.02085	1.816	0.50
26/12/18 8.01	-21.42988	64.02110	1.531	0.34
27/12/18 22.59	-21.43497	64.01311	2.490	0.15
28/12/18 2.04	-21.42975	64.01281	3.310	0.22
29/12/18 15.07	-21.42982	64.01689	1.600	0.61
31/12/18 19.31	-21.44366	64.01016	1.709	-0.03

1/1/19 6.11	-21.42481	64.01829	2.492	1.13
6/1/19 7.27	-21.43790	64.01043	2.318	0.28
6/1/19 7.39	-21.43459	64.01410	2.609	0.65
6/1/19 7.41	-21.43798	64.01557	2.551	0.69
6/1/19 8.08	-21.43250	64.01032	2.664	0.26
7/1/19 3.40	-21.42176	64.01758	1.835	0.57
8/1/19 4.56	-21.44438	64.01175	1.627	0.02
12/1/19 19.11	-21.41795	64.01341	3.649	0.01
14/1/19 0.35	-21.42174	64.02409	2.089	0.09
24/1/19 16.42	-21.42754	64.00913	2.547	0.62
24/1/19 16.46	-21.42457	64.00973	2.846	0.09
25/1/19 0.44	-21.42987	64.02048	2.489	0.25
25/1/19 20.05	-21.42815	64.02188	3.036	0.55
27/1/19 7.21	-21.43503	64.01430	2.030	0.14
28/1/19 1.35	-21.41702	64.02052	2.148	0.00
29/1/19 10.48	-21.42987	64.02048	2.732	1.01
30/1/19 14.33	-21.41354	64.02288	2.276	1.40

Table B.6 – Relative magnitude of Cluster 6

Date	Longitude	Latitude	Depth (km)	Relative Magnitude
22/12/18 11.00	-21.28347	64.11058	5.433	0.56
22/12/18 13.18	-21.29165	64.10698	5.579	0.80
22/12/18 18.16	-21.27530	64.11419	4.400	0.39
22/12/18 21.36	-21.29165	64.10698	5.499	0.30
24/12/18 10.51	-21.28986	64.10339	5.600	0.55
24/12/18 12.51	-21.28192	64.10340	4.948	0.81
24/12/18 13.37	-21.28337	64.10062	5.200	0.62
24/12/18 14.01	-21.27962	64.10430	5.614	0.48
24/12/18 15.45	-21.28340	64.10340	5.443	0.51
24/12/18 17.52	-21.28187	64.10340	5.743	0.38
28/12/18 2.45	-21.28563	64.10699	5.206	0.51
30/12/18 20.26	-21.28341	64.10405	5.586	0.77
6/1/19 16.59	-21.28345	64.10832	5.200	0.40
6/1/19 20.06	-21.28347	64.11058	5.200	0.64
7/1/19 23.33	-21.28876	64.10698	5.600	0.57
8/1/19 4.22	-21.26711	64.11704	4.948	0.39
12/1/19 13.28	-21.28204	64.11353	4.871	0.45
15/1/19 10.59	-21.28154	64.10341	5.457	1.00
20/1/19 0.45	-21.28163	64.10409	5.200	0.43
24/1/19 1.56	-21.28487	64.10917	5.200	0.21
26/1/19 21.43	-21.28524	64.11058	5.272	0.34
26/1/19 23.18	-21.28034	64.11059	5.353	0.49
27/1/19 7.47	-21.28194	64.10994	5.513	0.90
27/1/19 22.35	-21.28346	64.10926	5.429	0.34
28/1/19 16.27	-21.28347	64.11058	5.268	0.60

Table B.7 – Relative magnitude of Cluster 7

Date	Longitude	Latitude	Depth (km)	Relative Magnitude
16/1/19 6.40	-21.58352	64.03631	5.134	1.16
16/1/19 9.28	-21.58105	64.03620	5.773	0.81
16/1/19 14.20	-21.58055	64.03236	5.818	1.52
16/1/19 14.24	-21.57744	64.03302	5.746	0.87
16/1/19 17.01	-21.58090	64.03149	5.826	1.05
16/1/19 17.03	-21.57894	64.03073	5.911	0.89
16/1/19 22.40	-21.57894	64.03581	6.000	0.91
16/1/19 23.35	-21.58063	64.03229	5.756	0.72
16/1/19 23.37	-21.58420	64.03137	5.843	1.05
16/1/19 23.51	-21.58423	64.03071	5.673	0.91
17/1/19 0.25	-21.58328	64.03312	5.820	1.40
17/1/19 0.28	-21.58284	64.03132	5.674	0.98
17/1/19 2.55	-21.58666	64.03211	5.978	0.88
17/1/19 13.32	-21.58271	64.03322	5.434	0.92
18/1/19 9.46	-21.57786	64.03348	5.249	1.21
19/1/19 15.43	-21.56446	64.03160	5.433	1.62
22/1/19 2.19	-21.58693	64.03076	5.836	1.21
22/1/19 10.29	-21.58394	64.03302	5.910	1.28
22/1/19 10.41	-21.57933	64.03632	5.543	1.60

Table B.8 – Relative magnitude of Cluster 8

Date	Longitude	Latitude	Depth (km)	Relative Magnitude
23/12/18 3.05	-21.35738	64.11119	3.600	-0.11
23/12/18 3.06	-21.35739	64.11200	3.600	0.65
23/12/18 5.03	-21.35428	64.11692	4.368	0.03
25/12/18 22.41	-21.35897	64.10470	3.491	0.60
25/12/18 23.19	-21.35585	64.11333	3.670	0.28
28/12/18 2.13	-21.35739	64.11197	3.600	0.47
4/1/19 15.36	-21.35738	64.11183	3.600	0.67
8/1/19 0.38	-21.35207	64.11043	3.511	0.42
8/1/19 0.40	-21.35563	64.10967	3.338	-0.03
20/1/19 23.47	-21.34911	64.10685	4.254	0.13
22/1/19 10.33	-21.35222	64.11112	4.178	0.42
22/1/19 10.35	-21.35737	64.11042	3.529	0.19
22/1/19 10.36	-21.35737	64.11042	3.531	0.19
29/1/19 16.26	-21.36539	64.09663	3.266	1.30

Appendix C. Data fitting and optimization of moment tensor inversion

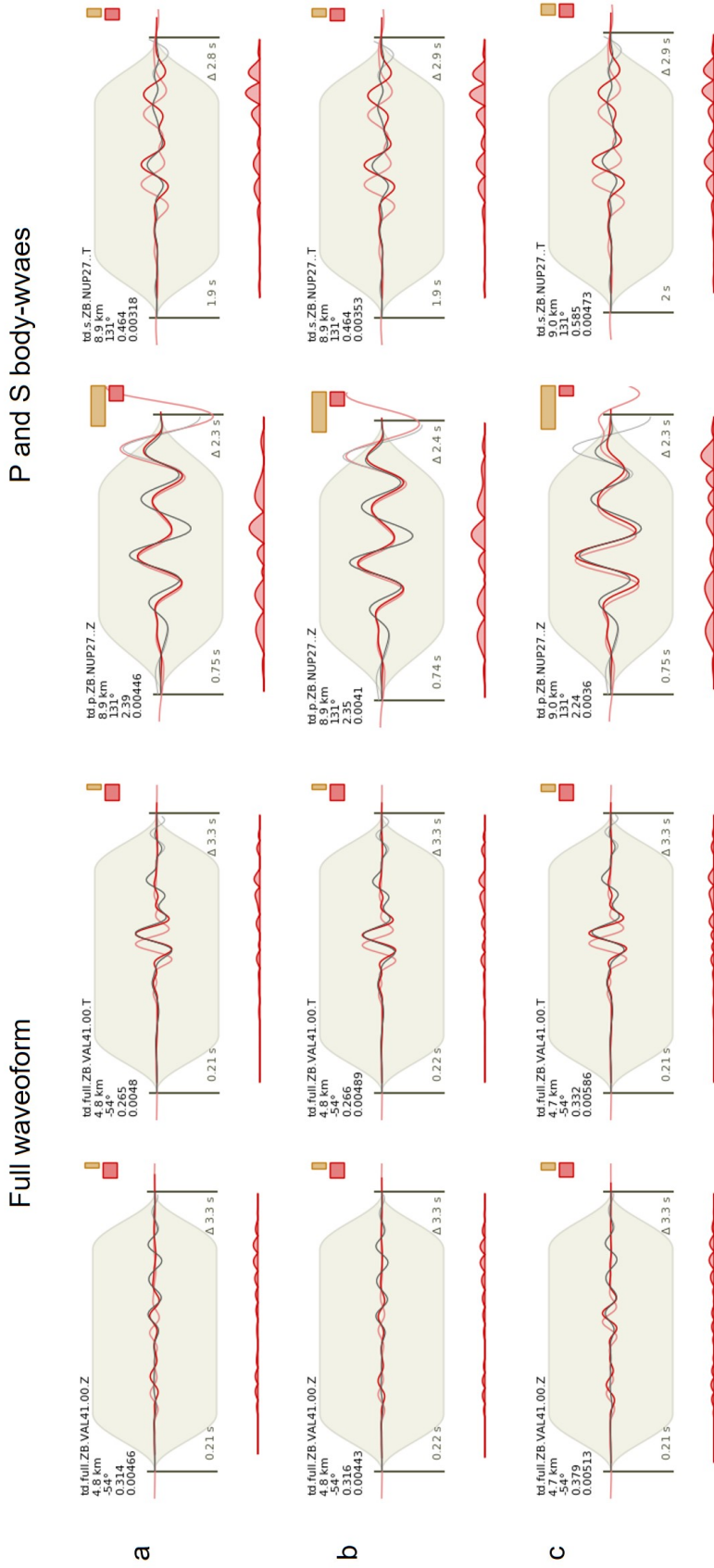


Figure C.1 - Observed and synthetic full-waveform (left side) and body waves (right side) best fitting model of the master events occurred on 29 January 2019 for DC (a), deviatoric (b) and full (c) source models. In each panel, target information are indicated on the left side (from top to bottom) giving station name with component, distance to source, azimuth of station with respect to source, target weight, target misfit and starting time of waveform relative to the origin time. The background area shows the applied taper function. The waveforms shown are: the filtered observed trace without tapering (light grey) and the same with tapering and processing (dark grey), the synthetic trace (light red) and the filtered and tapered processed synthetic trace (red). The traces are scaled according to target weight (small weight, small amplitude) and normed relative to the maximum amplitude of targets (i.e. full waveform and body waves). Sample-wise residuals for time domain comparisons are shown on the bottom of panels. Color boxes on the upper right show the relative weight of target within the entire dataset of optimization top box, orange) and the relative misfit contribution to the global misfit of the optimization (bottom box, red).

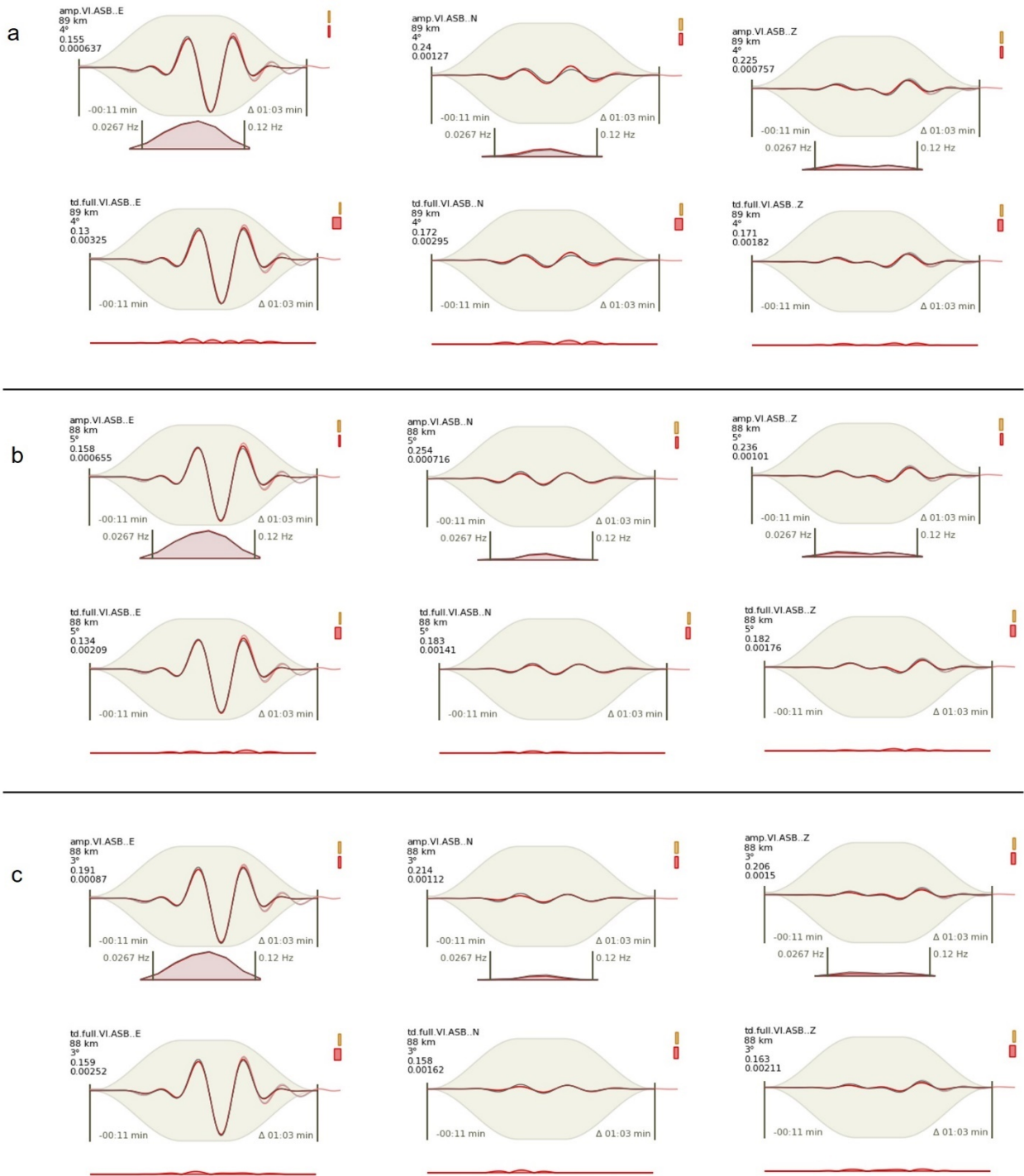


Figure C.2 – Observed and synthetic full waveform best fitting model of the mainshock for DC (a), deviatoric (b) and full source models (c) in both frequency top part in a, b, c panels) and time domain (bottom part in a, b, c panels). All information is explained in figure C1. Spectra of observed and synthetic traces for amplitude comparisons are added.

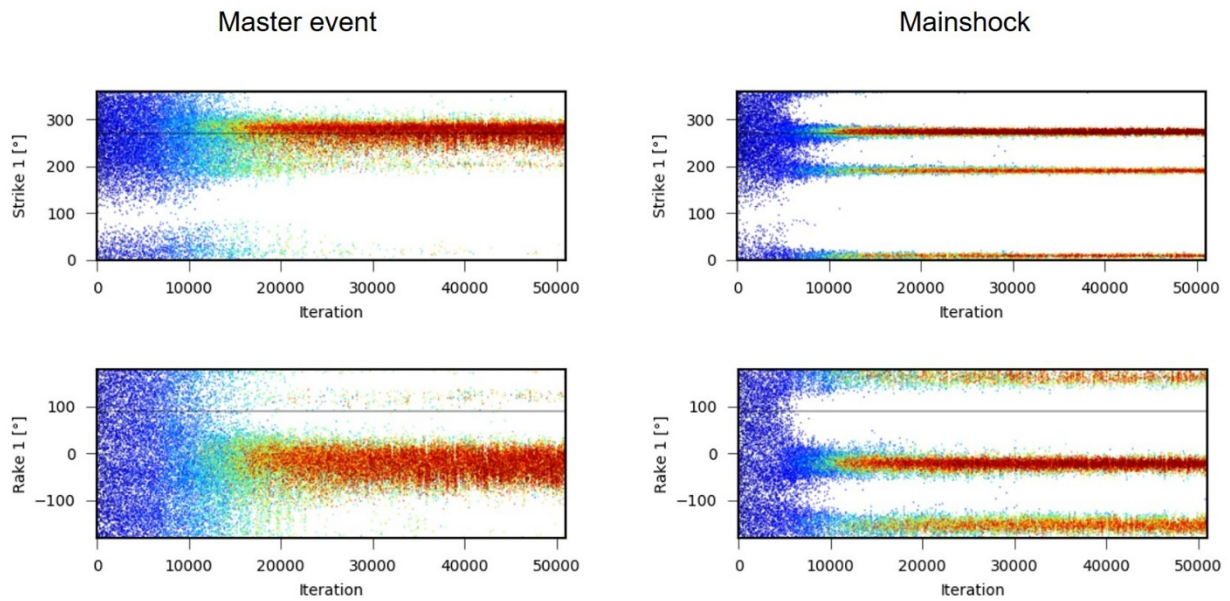


Figure C.3 – Sequence plots for strike and rake parameters of master event occurred on 30 December 2018 (left side) and mainshock (right side) optimization. The color shows the relative misfit: relatively high misfits are in cold blue colors and relatively low misfits in red. The sequence of parameter values is either a function of optimization or of the misfit from high to low. The values of parameter tend to converge at the same value with the lower misfits.

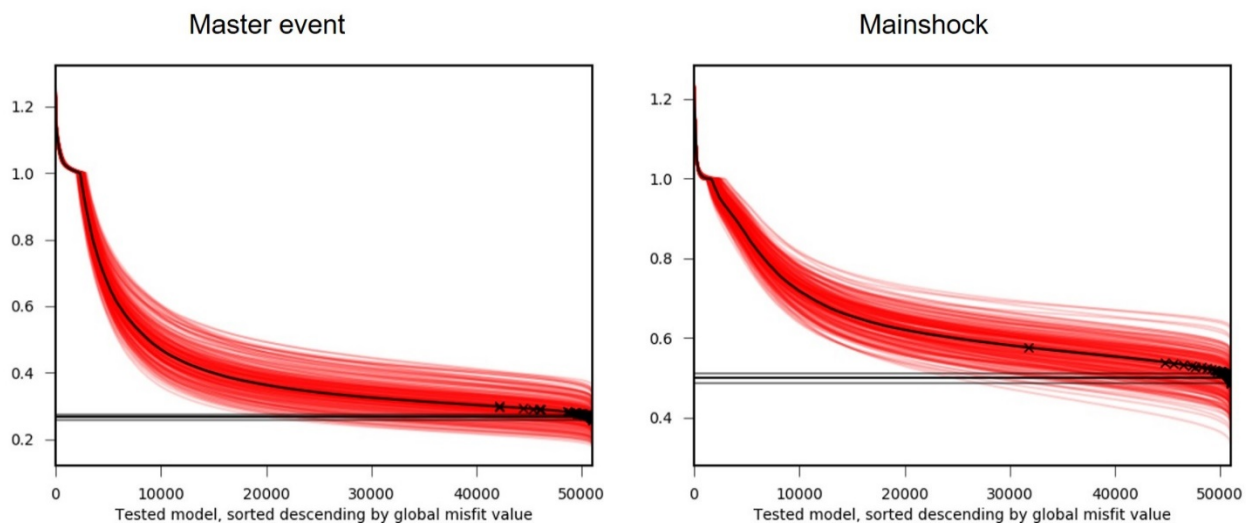


Figure C.4 – Sorted misfit (descending) of single bootstrap chains. For each bootstrap configuration, all models are sorted according to their misfit value (red lines) and their global misfit value (black line). The best model of every bootstrap configuration (right end model of red lines) is marked as a cross in the global misfit configuration. The horizontal black lines indicate mean and \pm standard deviation of the y-axis values (i.e. misfits) of these crosses. If the bootstrap configurations converge to the same region in model space, all crosses should be close to the right end of the plot.

Appendix D. Test Davis and Frohlich (1993)

Table D.1 – Results of Davis and Frohlich (1993) test for each spatial cluster

QUESTIONS	1 cluster	2 cluster	3 cluster	4 cluster	5 cluster	6 cluster	7 cluster	8 cluster
Background seismicity								
1) Are these events the first known earthquakes earthquakes?	NO	NO	NO	NO	NO	NO	NO	NO
Spatial correlation								
2) Are epicenters near wells (within 5 km)?	NO	YES Nesjavellir NO Hellisheidi	NO Nesjavellir YES Hellisheidi	NO Nesjavellir YES Hellisheidi	NO Nesjavellir YES Hellisheidi	YES Nesjavellir NO Hellisheidi	NO	YES Nesjavellir NO Hellisheidi
3) Do some earthquakes occur at or near injection depths?	NO	NO	YES	YES	YES	NO	NO	NO
4) If some earthquakes occur away from wells, are there known geologic structures that may channel fluid flow to the sites of the earthquakes?	NO?	YES?	YES?	YES?	YES?	YES?	NO?	YES?
Temporal correlation								
5) Is there a clear correlation between injection and seismicity?	NO	NO	YES	YES	YES	NO	NO	NO
Injection practices								
6) Are changes in fluid pressure at well bottoms sufficient to encourage seismicity?	NO	NO	YES	YES	YES	NO	NO	NO
7) Are changes in fluid pressure at hypocentral locations sufficient to encourage seismicity?	NO	NO	YES?	YES?	YES?	NO	NO	NO